THE UNIVERSITY OF MICHIGAN

INDUSTRY PROGRAM OF THE COLLEGE OF ENGINEERING

TWO-PHASE VORTEX FLOW

James F. Lafferty

A dissertation submitted in partial fulfillment
of the requirements for the degree of
Doctor of Philosophy in the
University of Michigan
Department of Nuclear Engineering

June, 1967

IP-782

ACKNOWLEDGEMENTS

Professor Frederick G. Hammitt, doctoral committee chairman, gave unsparingly of his time in providing guidance, assistance and encouragement throughout the course of this investigation.

The members of the doctoral committee and the Faculty of the Department of Nuclear Engineering in general supplied many helpful suggestions. Special acknowledgement is due to Dr. Robert Cheesewright, Queen Mary College, University of London, for many enlightening and stimulating discussions. Mr. R. A. Robinson, Research Assistant, performed much of the technical work required in the design, assembly and calibration of the test facility.

The encouragement, understanding and phenomenal tolerance displayed by my wife, Vivian, were indispensable to the sucessful completion of this project.

Financial support for this work was supplied by the Michigan Memorial Phoenix Project, The University of Michigan, under grant No. 293. The aid received through the National Science Foundation Science Faculty Fellowship program is also gratefully acknowledged.

TABLE OF CONTENTS

LIST OF TABLES

LIST OF ILLUSTRATIONS

NOMENCLATURE

A	Area
B	Magnetic flux density
b	Channel width
D	Diameter
E	Electric field intensity
E_o	Open circuit voltage
F	Force
f	Friction factor
h	Height of vortex
I	Electric current
K, k	Constants
L	Vortex length
M	Momentum
$\mathring{M}$	Momentum flux
m	Mass
$\mathring{m}$	Mass flow rate
P	Pressure
ΔP	Pressure drop from plenum chamber to exhaust ($P_a - P_E$)
R	Universal gas constant, Radius
Re	Reynolds number
r	radius
T	Temperature
U	Radial liquid velocity
u	Radial gas velocity
V	Tangential liquid velocity

v	Tangential gas velocity
v_o/v_n	Jet-recovery factor
x	Quality
y	Nondimensional radius
Z	Axial position
α	Void fraction
μ	Absolute viscosity
ν	Kinematic viscosity
ρ	Density
σ	Conductivity
ϕ	Asimuthal position

Subscripts

a	Plenum chamber conditions
c	Centrifugal
D	Drag
E	Exhaust conditions
F	Flowmeter measurements
g	Gas phase
L	Liquid phase
n	Nozzle exit conditions
o	Outer radius, zero void
P	Probe measurements
p	Pressure
r	Radial
s	Superficial

t	Total pressure
TP	Two-Phase
ø	Angular or tangential

CHAPTER I

INTRODUCTION

A. Motivation for the Investigation

Confined vortex flow has typically been utilized for such practical applications as viscosity measurements[1] and pressure diffusion separation[2,3] as well as being an area of traditional academic interest. Research on confined forced vortex flow was greatly intensified following the proposal of the cavity reactor concept[4,5] for nuclear rocket propulsion in 1957 and the vortex magnetohydrodynamic (MHD) power generator[6,7,8] in 1959. Interest has also been generated in the vortex valve,[9] vortex stabilization of arc discharges[10,11] and vortex flow heat exchangers[12] as well as in the study of vortices in natural phenomena.[13]

Although many types of vortex-like flow have been considered in conjunction with these diverse applications, there has been, to the author's knowledge, no analytical or experimental work reported on the characteristics of the gas-driven liquid vortex although at least two other investigators[14,15] have considered some aspects of the problem. This is surprising since this specific type of vortex flow has been considered in connection with both the liquid-core nuclear rocket[16] and the vortex MHD generator.[17,18] Analytical models have been presented for the wheel-flow,

liquid-gas, vortex,[19,20] driven by rotating the containment vessel, in which gas is introduced at the periphery and allowed to diffuse through the liquid under the influence of the strong pressure gradient; however, these models provide little insight into the characteristics of the gas-driven liquid vortex. Weber and Marston[17,18] considered the application of the vapor-driven liquid vortex to MHD power generation, but their analytical and experimental work did not consider the two-phase nature of the flow.

In view of the potential applications and importance of the gas-driven liquid vortex, this investigation was undertaken to determine the basic characteristics of this type of vortex flow.

B. Previous Investigation of Vortex Flow

This discussion will be concerned primarily with the aspects of jet-driven confined vortices which are applicable to the gas-driven two-phase vortex. The vortex flow of interest is characterized by a cylindrical containment chamber with injection ports in the cylindrical wall and a central exhaust port in one or both end plates. Although the characteristics of the gas-driven gas vortex and the liquid-driven liquid vortex are not necessarily typical of the gas-driven two-phase vortex, some of the results of the investigations of single-phase vortices serve to indicate the nature of the problems which are expected to be encountered in the two-phase vortex.

1. Secondary Flows: In vortex flow between flat plates, the reduced tangential velocity in the boundary layers is expected to result in increased radial flow in this region due to the decreased centrifugal force. In analytical investigations of a jet-driven vortex, Anderson[21,22] found that mass flow through the end-wall boundary layers can be appreciable for both compressible and incompressible flow. For sufficiently high ratios of v_o/u_o (ratio of tangential to radial velocity at the periphery), it was found that the flow through the boundary layers can exceed the total mass flow rate of the system, which implies that there can be considerable recirculation between the secondary and primary flows. In a comprehensive experimental investigation of the velocity distribution of a confined gas vortex, Savino and Keshock[23] confirmed that the secondary flow can be substantial and that considerable circulation between the secondary and primary flows exists. These tests were carried out at only one value of mass flow rate and v_o/u_o so that the dependence of the boundary layer flow on these parameters was not confirmed. An increase of the mass flow through the boundary layers with increasing total mass flow was shown analytically by Loper[24] and in an experimental investigation of a water vortex, Ginsberg[25] found that the boundary layer carried a large radial inflow of fluid.

In flow visualization studies of a jet-driven water vortex, Roschke[26] found that L/D (vortex length/diameter) ratios had a strong influence on the secondary flows for low

values of L/D. The overall effect appeared to be a decrease in the influence of the end-wall boundary layers with increasing L/D. Operation of the vortex with nonplanar end-walls (conical, hemispherical, and canted) indicated an increase in both axial and radial secondary flows as compared to the plane end-walls.

From these results it is apparent that in those applications of vortex flow in which a strong centrifugal force field is desired, the decrease in vortex strength due to secondary flows can be important.

2. Turbulence: As concluded by Donaldson,[8] jet driven vortices of an engineering scale are generally turbulent. Since turbulence results in a dissipation of energy, the level of turbulence and its dependence on flow parameters is of interest. From the results of an investigation of the effects of peripheral-wall injection techniques on the turbulence of a water vortex, Travers[27] reported that the turbulence level resulting from multi-jet injection was considerably (40 to 50%) greater than for a single-slot and four-slot injection. In these tests, the multi-jet configuration operated with 2144 injection ports in the cylindrical wall and the slots for the slot-injection configuration extended the length of the cylindrical wall. The higher level of turbulence with the multi-jet configuration was attributed to the much thinner turbulent mixing region near the peripheral wall.

McFarland[28] obtained similar results for an air vortex using the same configurations as that investigated by Travers.

In his flow visualization studies with a water vortex, Roschke[26] reported that the turbulence appeared to increase with both L/D and mass flow rate. It is noteworthy that Ragsdale[29] has been successful in obtaining a correlation for vortex turbulence. It was shown that a modified von Karman expression for eddy viscosity provides good correlation of the turbulent Reynolds numbers.

3. Jet Recovery Factor: As the result of an experimental study of gas vortices, Keyes[30] reported that the viscous retardation near the periphery of the vortex was "severe". This observation probably reflects the drag of the fluid on the cylindrical wall and the losses due to turbulent mixing of the driving jets. Defining v_o as the effective tangential velocity of the fluid at the cylindrical wall, or, more accurately, the velocity at the free-stream edge of the cylindrical wall boundary layer, a jet recovery factor which reflects these losses has been defined by Roschke[31] as v_o/v_n where v_n is the injection jet-velocity. Roschke determined values of the jet recovery factor ranging from about 0.2 to 0.95 for radial Reynolds numbers ($Re_r = \dot{m}/2\pi\mu L$) from 60 to 10^3. The minimum value of v_o/v_n occurred near $Re_r = 2 \times 10^2$. From the data reported by McFarland[28] for the air vortex, v_o/v_n varied from about 0.55 at $Re_r = 24$ to 0.625 at $Re_r = 157$.

Travers' data on the water vortex[27] indicates a jet recovery factor of about 0.87 at Re_r = 30 to 90 which agrees with Roschke's results.

These results indicate that the jet recovery factor for the gas-driven liquid vortex will be an important factor since the jet mixing losses of a gas jet directed into a liquid may well be substantial. It will be shown that the jet recovery factor for the two-phase vortex considered in this investigation is on the order of 0.3 for a gas radial Reynolds number on the order of 2×10^4.

4. Two-Component Vortex Flow: The basic aspect of the cavity nuclear reactor concept is the use of the strong radial pressure gradient generated by vortex flow to maintain a high density annulus of a heavy fuel gas in the presence of the flow-through of a lighter driving gas. Reshotko and Monnin[32] investigated the stability of a two-fluid wheel-flow ($V = a\,r$) vortex in which the inner fluid was heavier and found that the growth rate of the dynamic (Taylor) instability of this type of flow increases with increasing density of the heavy inner fluid. In an experimental and analytical investigation using argon and freon as heavy gases with hydrogen and nitrogen as the light gases, Pivirotto[33,34] demonstrated that in a jet-driven vortex an inner annulus of heavy gas could be maintained in steady state operation. These results were in qualitative agreement with his analytical model; however, the maximum density of the heavy gas was

found to be much lower than that required by the gaseous vortex reactor concept. Data obtained with an optical probe which did not disturb the flow indicated that the average retention time of the heavy gas particles was on the order of 1 to 4 seconds which was not significantly greater than that which would result if the mixture remained homogeneous throughout the flow. The only encouraging result from these investigations insofar as the gas-driven liquid vortex is concerned is that the heavier gas concentration increased with increasing molecular weight.

C. Problem Statement

Because of the complete lack of information on the characteristics of gas-driven two-phase vortex flow, it was decided that this investigation should utilize gas and liquid media which would afford the greatest experimental flexibility. Air and water were therefore selected as the fluids most suitable. Since the cavity reactor and the vortex MHD generator provide the most immediate application of this type of flow, the following objectives, which are of major importance in these applications, were established:

1) Develop a suitable laboratory test facility which would take advantage of existing laboratory facilities and provide for visual observation techniques as well as standard measuring instruments.

2) Develop the necessary instrumentation and measuring techniques.

3) Determine the radial and axial distributions

of pressure and density and determine the radial distributions of the velocity of both gas and liquid over a range of operating conditions.

4) Determine the effects of operating the two-phase vortex in the presence of a radial magnetic field.

5) Correlate the measured parameters to characteristic system parameters.

CHAPTER II

DESCRIPTION OF EXPERIMENTAL APPARATUS AND INSTRUMENTATION

A. The Vortex Assembly

The vortex was contained in a cylindrical chamber 1.0 inch long and 5.0 inches in diameter (inside dimensions). The outer wall of the chamber contained a water injection port as well as nozzles which directed air jets tangentially into the chamber. As shown in the schematic view in Fig. 2.1, a center tube, 1.62 inches in diameter, contained axial slots through which the air was exhausted. A second ring, 8.0 inches in diameter and concentric with the nozzle ring, formed a plenum chamber to facilitate the even distribution of air to the nozzles. The exhaust line from the vortex chamber was connected to a water trap to avoid having the water pass through the back-pressure control valve.

The end plates of the chamber were machined from 1.0 inch thick plexiglas which permitted visual observation of the vortex. One of the end plates contained six static pressure taps spaced at 0.1875 inch intervals radially and 30° azimuthally. The 0.062 inch diameter pressure tap holes were also used as access holes for the impact pressure probe. Subsequent to making the pressure measurements, these holes were enlarged to 0.125 inch diameter to accept the void

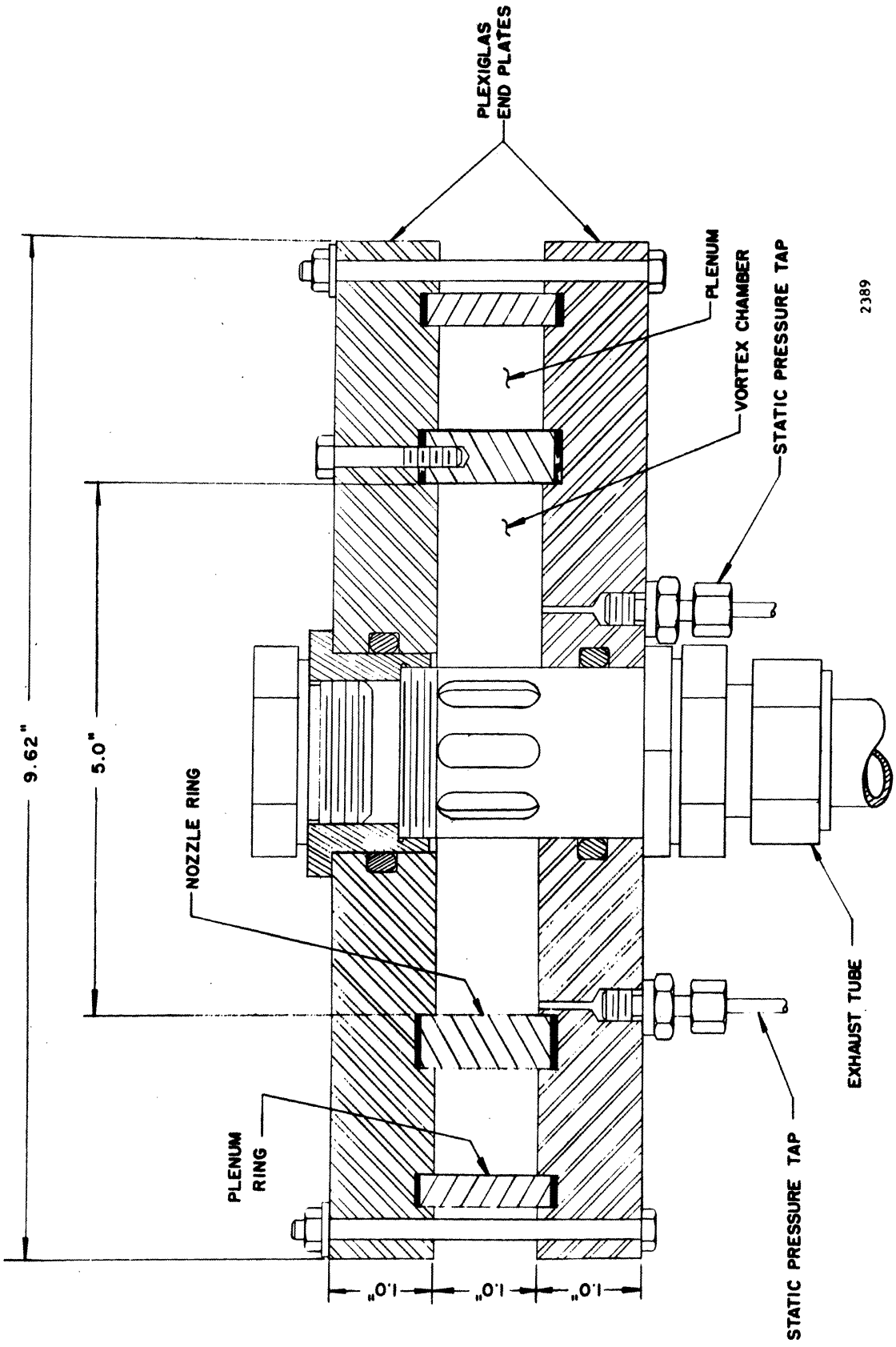

Fig. 2.1 - Schematic Representation of the Vortex Chamber.

fraction probe. The relative location of the pressure taps and the exhaust tube is shown in the photographs of the assembled vortex chamber in Fig. 2.2.

In the initial vortex assembly the nozzle ring formed two 2-dimensional nozzles 180° apart. This simple nozzle arrangement was obtained by machining the nozzle ring in two sections with the mating ends of the sections forming two converging nozzles with a throat section 0.125 inch wide. This arrangement was used in the early operation of the facility to verify that a vortex of reasonable density could be maintained and to check the general operation and response of the instrumentation.

A second nozzle ring, with which all subsequent tests were run, was made of plexiglas with twelve converging nozzles of circular cross section and a 0.125 inch diameter throat. The nozzles were located at 45° intervals with double nozzles at every other location, as shown in the photograph of Fig. 2.3.

The radial magnetic field required for the final phase of the investigation was supplied by coils placed above and below the vortex chamber, as illustrated in Fig. 2.4. The radial field was obtained by connecting the coils such that two opposed current loops were formed. With this arrangement, the axial components of the superposed fields tend to cancel while the radial components reinforce each other. The coils, made of No. 14 copper wire, were connected to a 120/240-volt d.c. rectifier and the current controlled by ten 500-watt incandescent

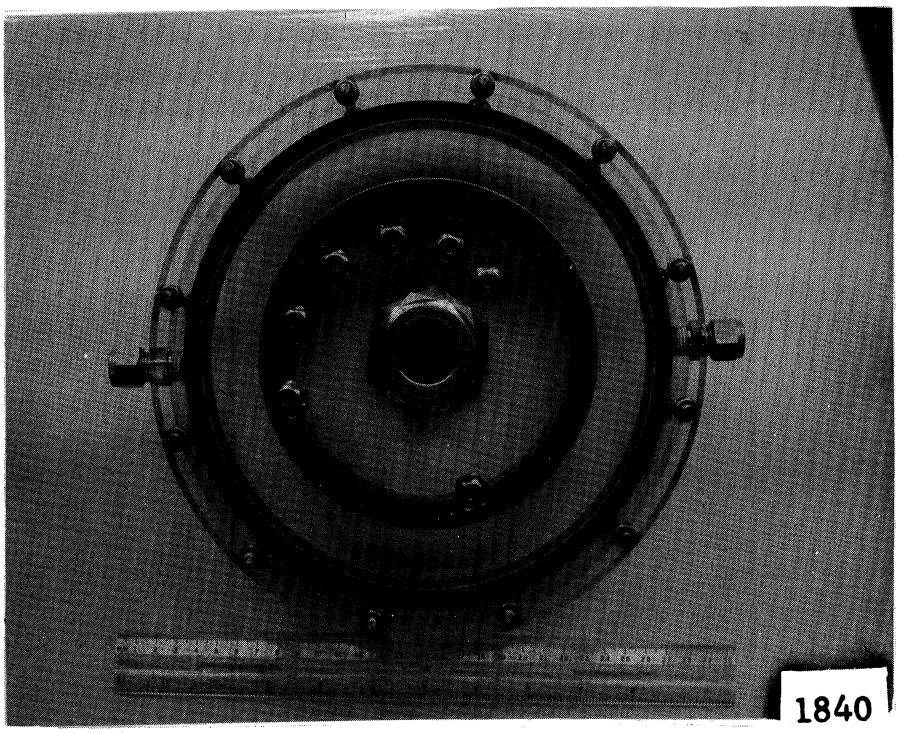

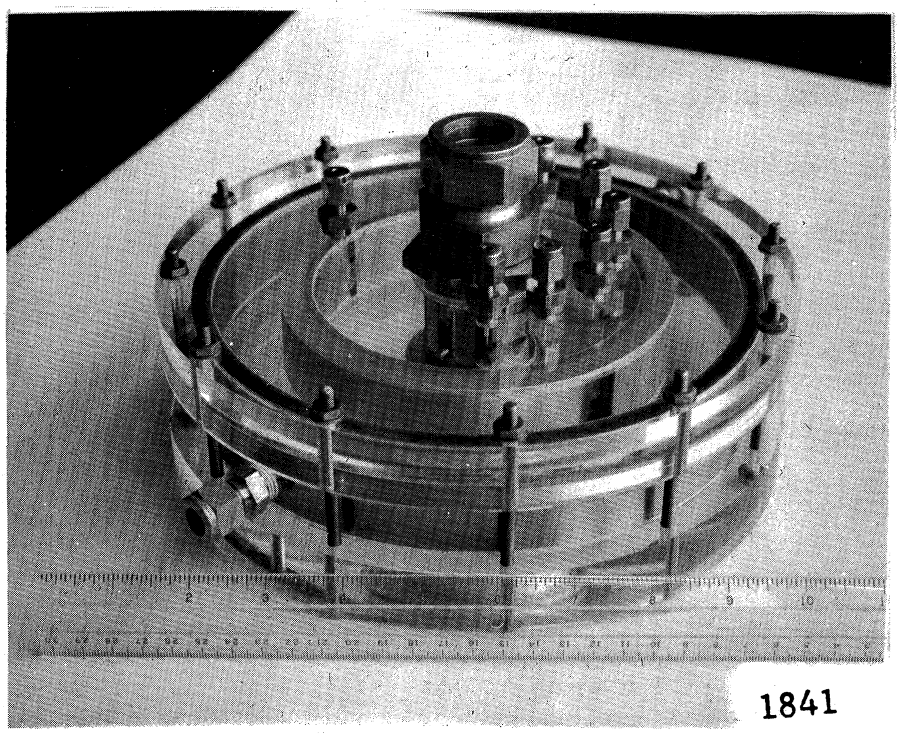

Fig. 2.2 - Photographs of the Vortex Chamber.

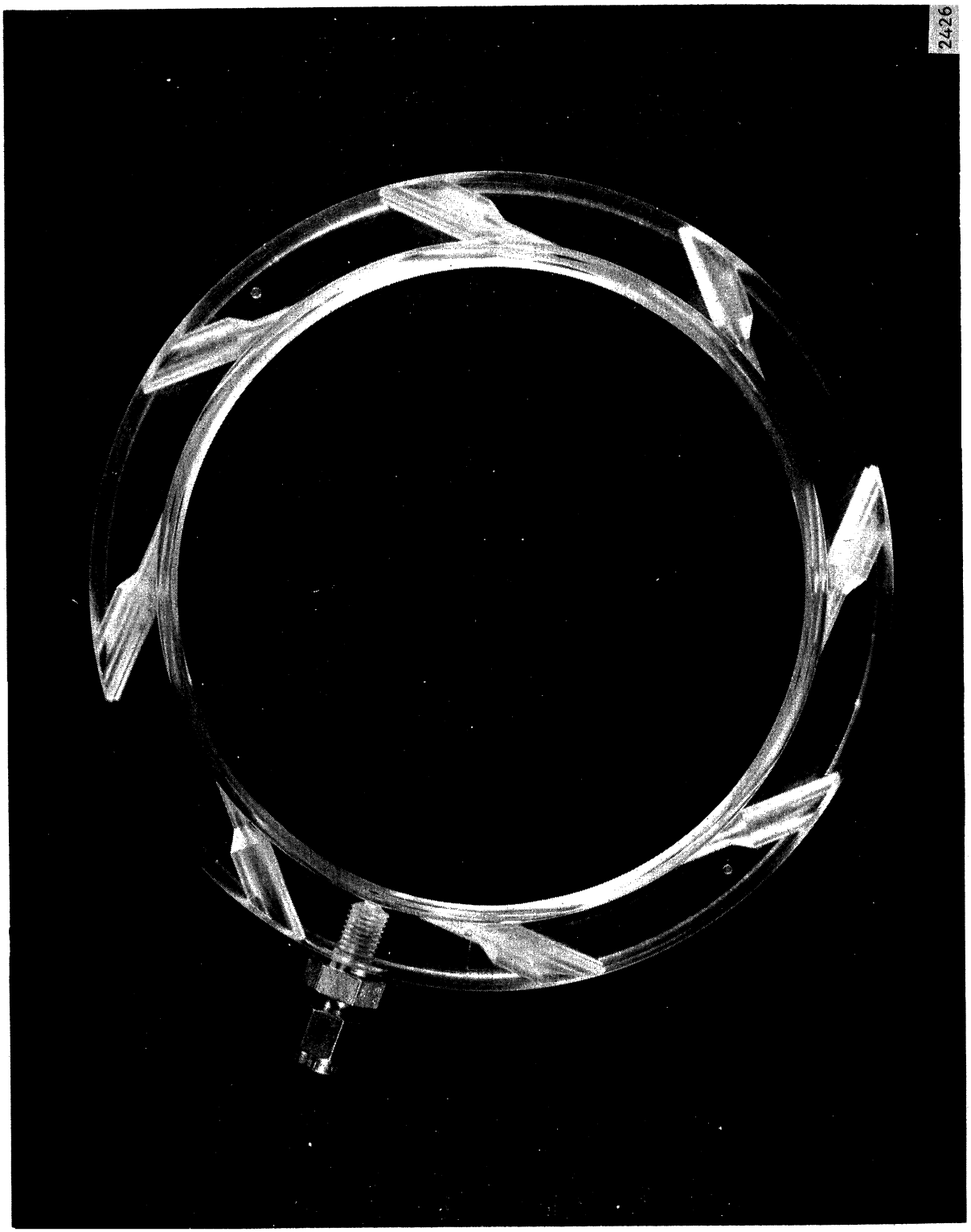

Fig. 2.3 - Plexiglas Nozzle Ring (Twelve Nozzle Configuration).

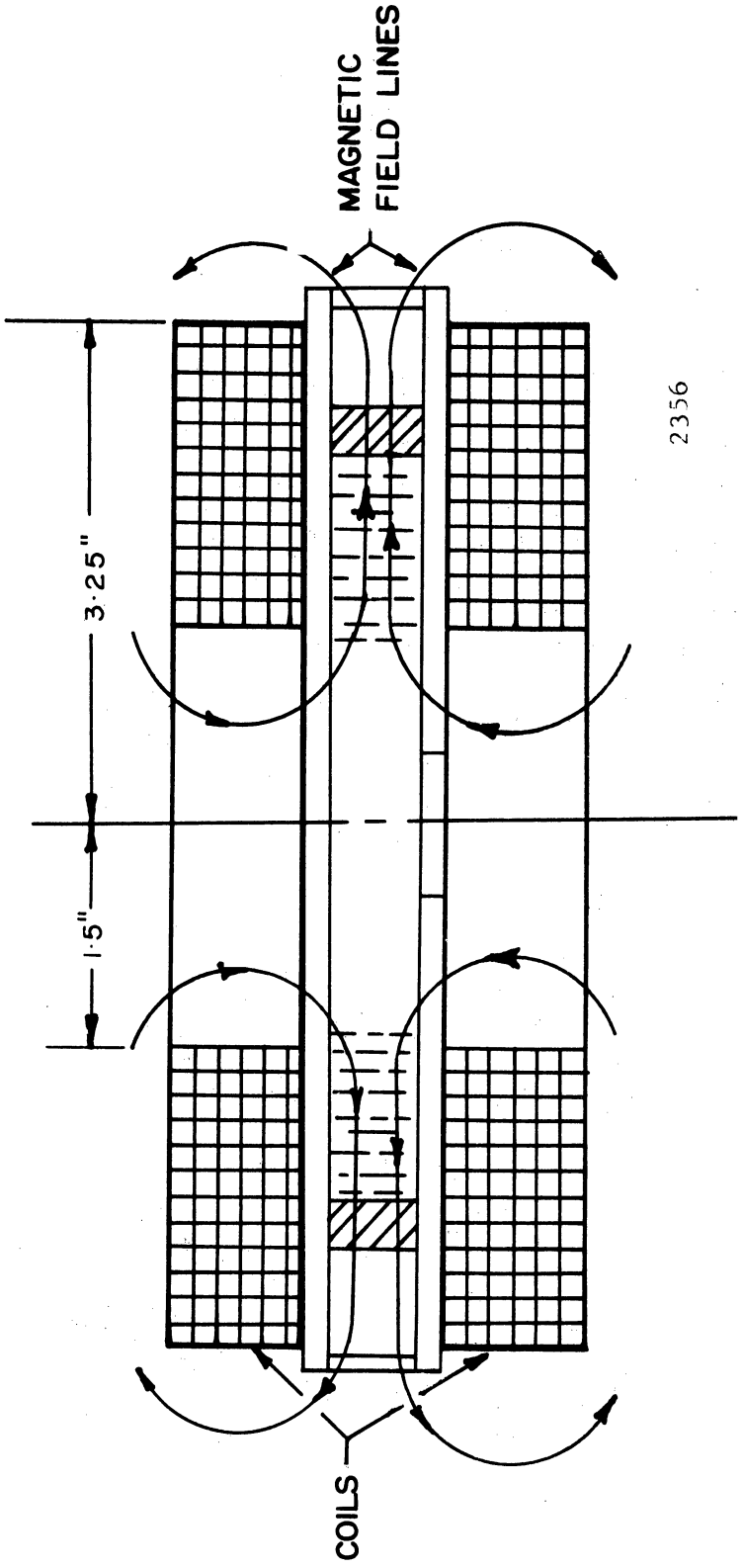

Fig. 2.4 - Sketch of the Vortex Chamber Showing Location of the Magnetic Field Coils.

lamps wired in parallel. The lamp circuit was operated in series with the coils.

For the tests in which the vortex was operated in the presence of the magnetic field, stainless steel electrodes in the form of annular discs were installed on the end plates of the vortex chamber. The electrodes were recessed so that they were flush with the end plates and the chamber dimensions were unchanged. The electrodes had an internal diameter of 3.00 inches and an outer diameter of 5.00 inches. In conjunction with this modification, the connectors to the static pressure taps were removed and the holes closed off so that the magnetic field coils could be mounted against the end plates. Access to the static pressure taps was then provided by drilling radially from the outer edge of the end plate to intersect the pressure tap holes. The photographs in Fig. 2.5 show the electrode plate installed and the modified pressure taps.

B. Instrumentation

1. Static Pressure: In making the pressure measurements, an all-air measuring system was used in preference to an alternative all-water system since it proved more convenient to keep the air system free of water than to maintain a water system free of entrained air bubbles. In either system there is a tendency for the air-water mixture to enter the pressure measuring system from the two-phase flow. Since the pressure

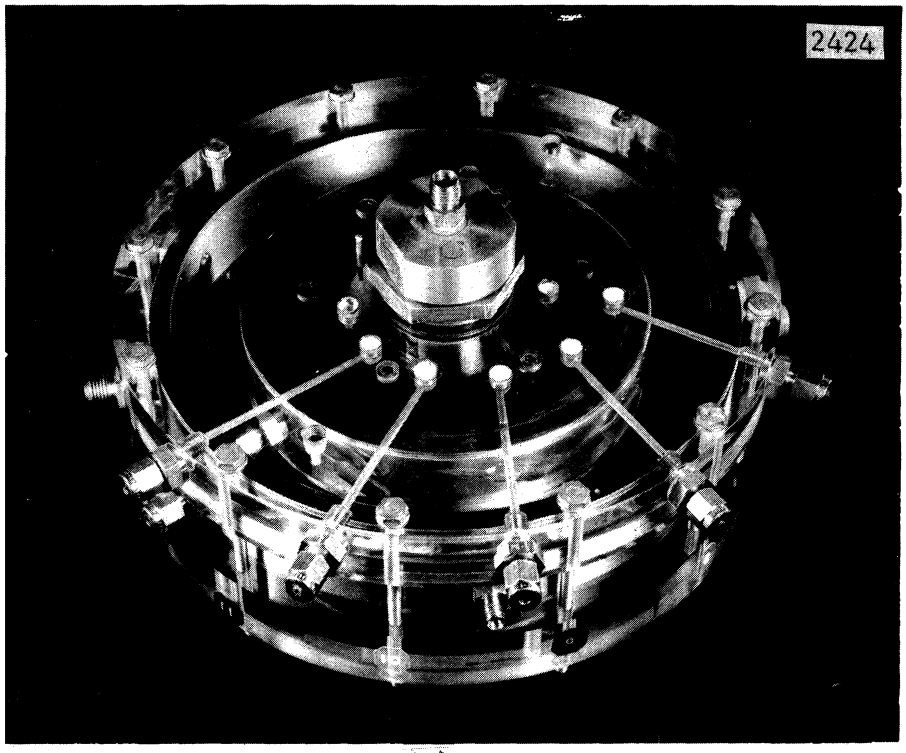

(a)

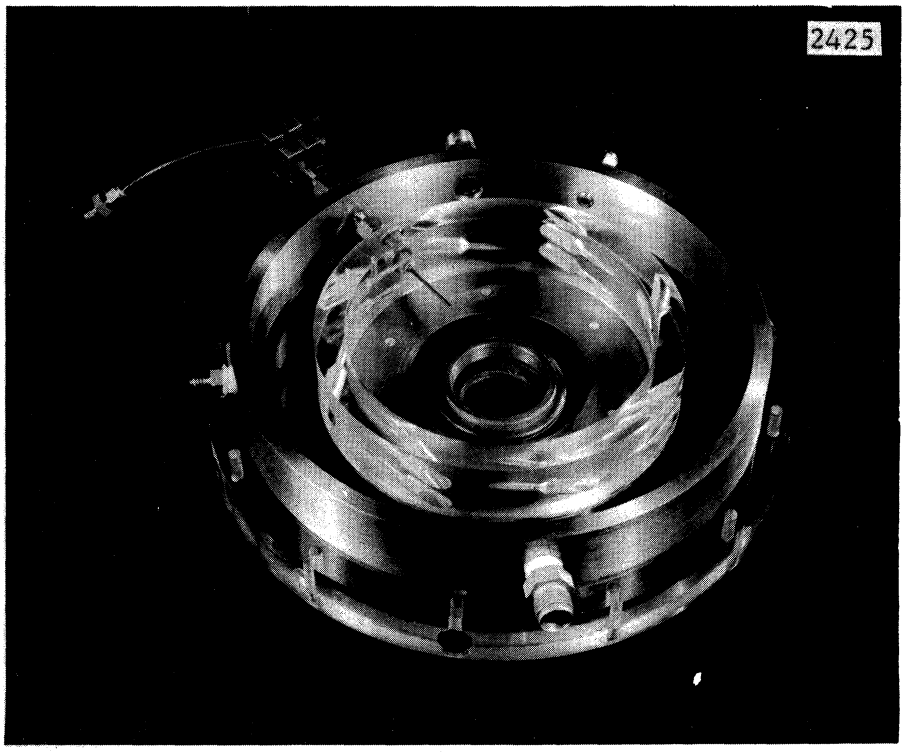

(b)

Fig. 2.5 - Modified Vortex Chamber Showing a) Assembled Unit with Relocated Static Pressure Tap Connectors, and b) Location of Bottom Electrode and Radially Inserted Pitot Tube.

gauge was about 1.5 feet above the vortex assembly, tap lines filled with water would result in the pressure gauge sensing pressures which were low by about 0.7 psi compared to that at the point of measurement. The gauge could be adjusted to compensate for this error; however, if an undetermined amount of air entered the measuring system, the gauge would be over-compensated and the resulting error in measurement could, in many cases, make relative measurements meaningless. Hence, in making measurements of this type, it is essential to maintain the pressure measuring system free of either gas or liquid. In the air system which was used, air was maintained at a slight positive pressure relative to the vortex, thus preventing the water from entering the pressure tap lines. When making a pressure measurement, the air bleed to the tap line was cut off and the pressure allowed to balance that in the vortex. Although the pressure fluctuations in the vortex resulted in the air-water mixture eventually entering the lines of the pressure measuring system, an equilibrium condition existed long enough to obtain valid and repeatable measurements. As illustrated in the schematic of the pressure measuring system in Fig. 2.6, the pressure taps were connected via valves to a manifold which was, in turn, connected to the pressure gauge. The pressure gauge, which could be read accurately to within ± 0.05 psi, could alternately be connected to the pressure manifold and the plenum chamber.

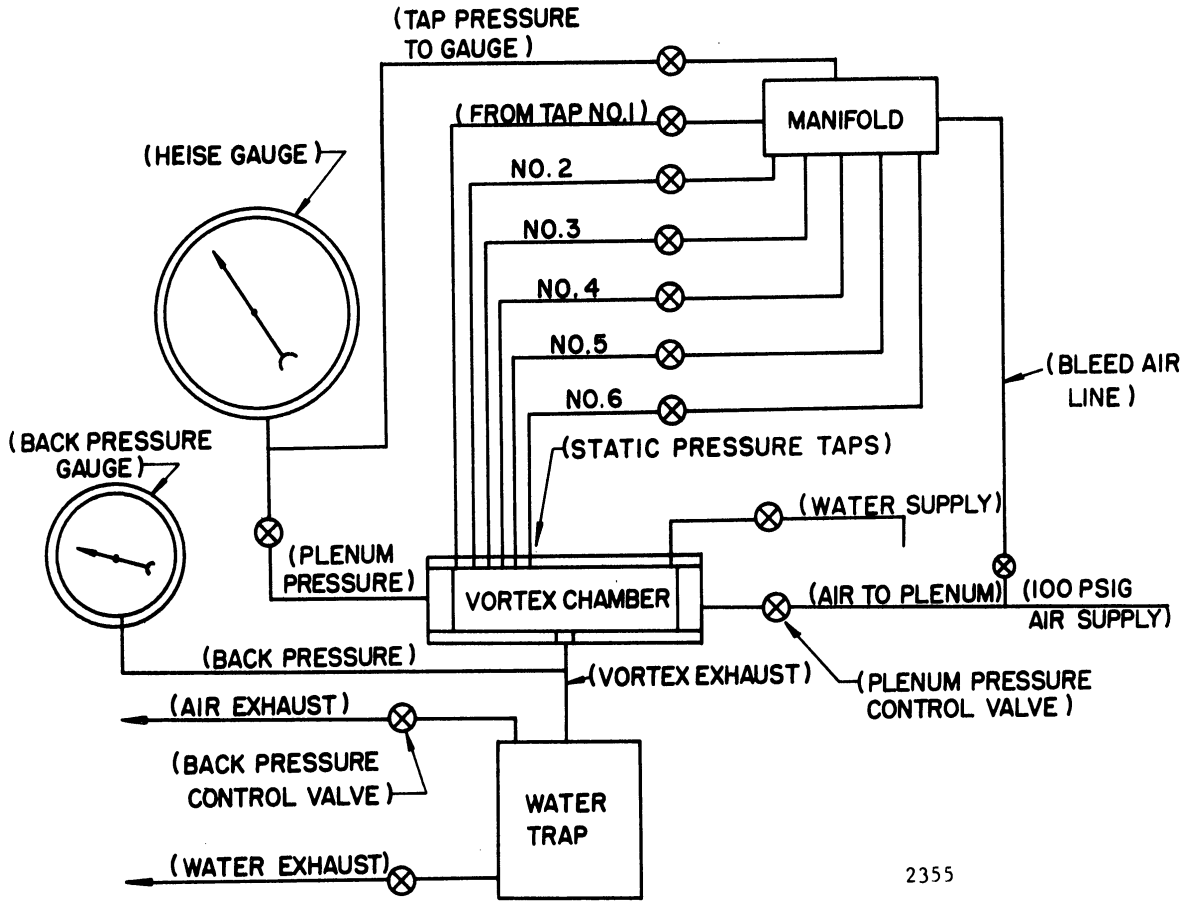

Fig. 2.6 - Schematic of the Pressure Measuring and Control System.

2. Total Pressure: The total pressure measurements were made by inserting the impact pressure probe, connected to the Heise gauge, through the static pressure-tap holes. The impact pressure probe, shown in Fig. 2.7a, was a 0.062 inch diameter tube with a 0.0156 inch diameter hole drilled normal to the tube axis through one wall only. This hole was located 0.125 inch from the sealed end of the tube. The impact probe response in an air stream was compared to that of a 0.125 inch diameter pitot tube of standard design and found to give accurate readings.

Initially, the use of water and mercury manometers was considered but it was found more convenient to make the pressure measurements with the Heise gauge which, under the influence of the vortex pressure fluctuations, could be read with an accuracy comparable to that obtained with the mercury manometer. The use of the Heise gauge later proved to be a virtual necessity since the upper range of pressures investigated could have required a mercury column ten feet in height to make the measurements.

3. Void Fraction: The void fraction measurements were obtained with a conductivity probe (Fig. 2.7b) which was developed specifically for this investigation. The probe consists of two closely spaced electrodes at the end of a 0.125 inch diameter tube. Since the insertion of this probe into the vortex required that the pressure tap holes be enlarged to 1/8 inch diameter, the void fraction measurements

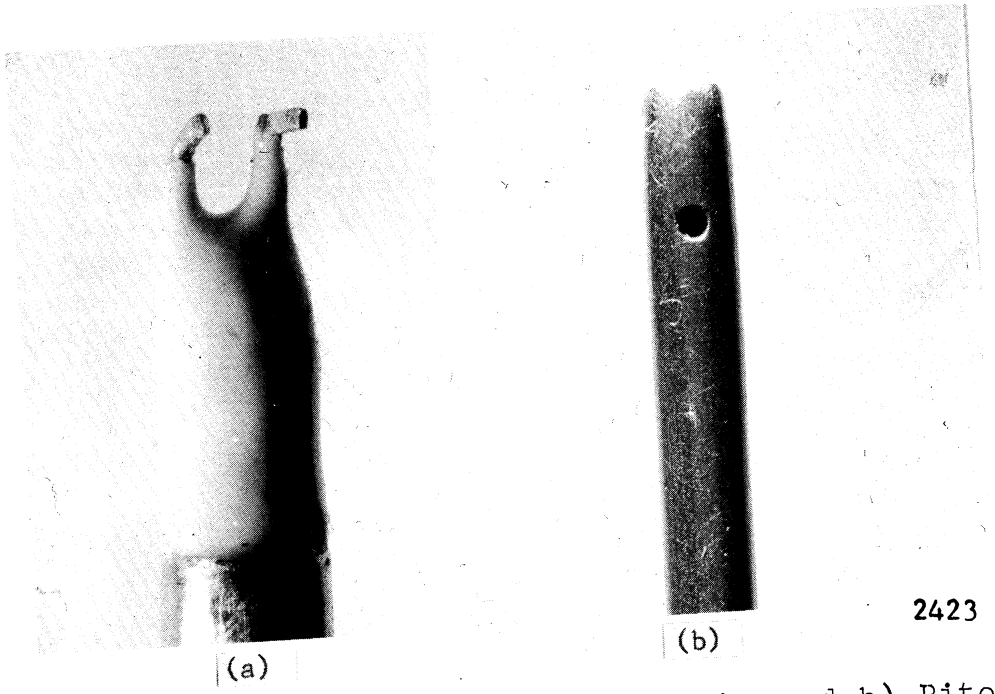

Fig. 2.7 - a) Void Fraction Probe and b) Pitot Tube (seven times actual size).

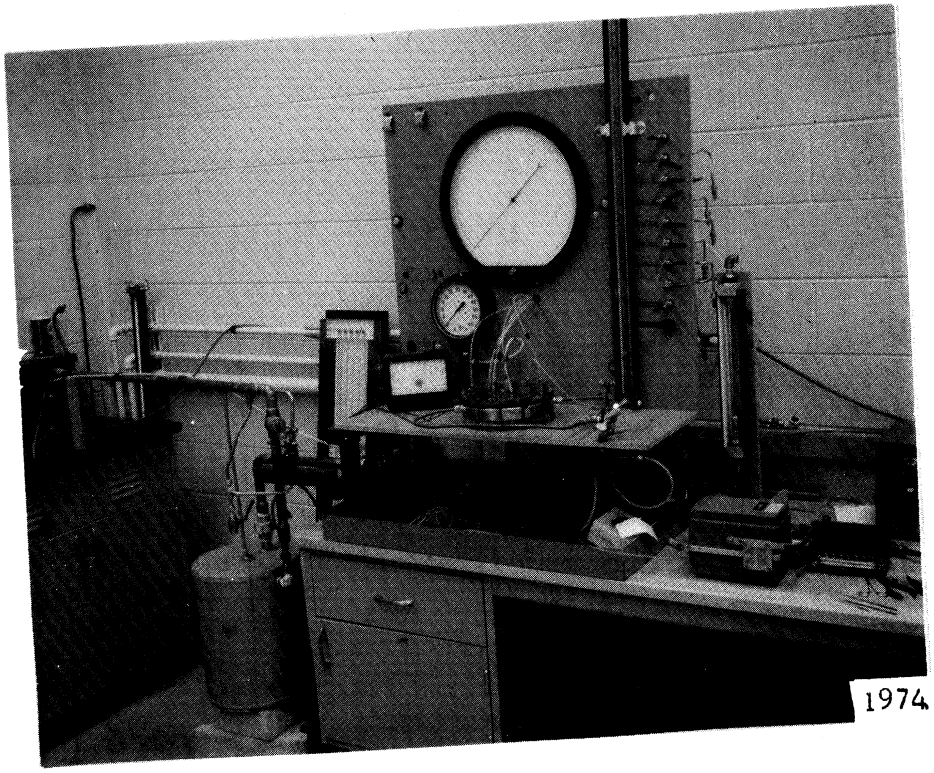

Fig. 2.8 - Test Facility.

were made after completion of the pressure measurements. The current conducted across the two-phase mixture between the probe electrodes was read on a milliammeter and the void fraction determined from the current magnitude relative to that obtained in the water with no voids. The voltage applied to the void fraction probe was obtained from two 22 1/2-volt dry cell batteries connected in parallel. The development and calibration of this probe is described in Chapter III.

4. Miscellaneous Measurements: The air mass flow rate was measured with a calibrated rotameter and the temperatures of the air, water and the two-phase vortex were measured using copper-constantan thermocouples. The magnetic field strength obtained with the coils was measured with a Hall effect magnetometer and the open circuit voltage of the unit, when operated in the presence of the radial magnetic field, was measured with a digital voltmeter with 11.0 megohms input impedance.

Fig. 2.8 is a photograph of the assembled test facility, showing the principal components of the instrumentation.

CHAPTER III

DEVELOPMENT OF THE VOID FRACTION PROBE

A. Introduction

The gas volume fraction in two-phase flow investigations has typically been measured by "trapping" methods[35,36] and, more recently, by gamma ray attenuation.[37] The trapping method isolates a section of the flow and provides a void fraction measurement which is an average value over a length of flow channel.

The gamma-ray attenuation method measures the void fraction across a section of the flow channel and gives an average value for this cross section. In those cases in which the vapor volume fraction is axially symmetric in a cylindrical duct or the flow is in thin rectangular channels, traversing techniques can be used to infer local void fraction.[37,38] In flows in which these conditions do not exist, much more elaborate techniques, in which the radioactive source or the detector or both is inserted into the flow, would be required to obtain local void fractions.

A third alternative, the use of the electrical conductivity of a two-phase mixture to indicate the void fraction averaged over a cross section of the channel, has been recently demonstrated by Petrick.[39] From the conductivity measurements made across the channel the void fractions were obtained by

the relation

$$\frac{\sigma}{\sigma_{TP}} = \frac{2 + \alpha}{2\,(1 - \alpha)} \qquad (3.1)$$

where

σ = the conductivity of the water with no voids

σ_{TP} = the conductivity of the two-phase mixture

α = void fraction = volume of voids/total volume

Equation (3.1) is obtained from a relation derived by Maxwell[40] in which he assumed a dispersion of small spheres in a spherical medium and arrived at an expression for the conductivity for large distances across the mixture. Equation (3.1) is for the case in which the dispersed medium has zero conductivity, e.g., dispersed voids, and is restricted to small values of void fraction. Petrick reported that void fractions obtained by this method were in good agreement with gamma-ray measurements for void fractions up to 0.95.

The inability of any of these methods to provide a reliable means of measuring local void fractions, except in special cases, has prompted the recent development of electrical probes for this purpose. Nassos[41] has reported the development of an a.c. impedance probe which gave very poor agreement with gamma-ray attenuation measurements. Bencze and Ørbeck,[42] however, have been able to obtain very good results with the same type of probe by modification of the associated circuitry. Close agreement between the probe measurements

and those obtained by the trapping method were reported for void fractions from 0.1 to 0.5.

Since the information concerning the a.c. impedance probe was not available at the inception of this investigation, a program was undertaken to develop a d.c. conductivity probe to measure local void fractions.

B. Basis of Calibration

If the conductivity of a two-phase flow is measured across an increment which is of the order of magnitude of the size of the voids, the observed value will obviously be related to the void fraction at that point. However, it is not clear that Equation (3.1) will apply in general since this relation was derived assuming widely separated voids with the conductivity measured across a large distance. If a conducting liquid flows past two closely spaced electrodes, the current resulting from an applied potential would consist of two parts: (a) the current through the surface film of liquid covering the supporting structure connecting the electrodes, and (b) that due to the ions in the flowing liquid which are attracted to the electrodes.

Assuming that the current through the surface film can be neglected compared to that due to the ions collected from the flowing liquid (which would be the case for a properly designed probe), the decrease in the time-averaged current due to a uniform dispersion of voids in the liquid can, as

a first approximation, be considered to be due predominately to either a decrease in the ion density of the two-phase mixture or a decrease in the effective electrode area. Since both of these parameters vary as the liquid fraction $(1 - \alpha)$, either viewpoint results in the conclusion that the ratio of the average currents with and without voids will be approximately

$$I/I_o = (1 - \alpha), \tag{3.2}$$

where

I_o = time averaged current with zero void fraction

I = time averaged current with void fraction α

By using a small conductivity probe to measure the currents as described above, the void distribution in a two-phase flow can be obtained by the use of Equation (3.2). The validity of these results can be examined by comparison to a void fraction measurement made simulaneous with, and independent of, the current measurements. In the absence of a readily available means by which a point-by-point comparison can be made, an independent measurement of the total void fraction in a channel can be used for this purpose. In terms of flow rate measurements and the slip ratio, the total void fraction is, by application of its basic definition,

$$\alpha_F = \frac{1}{1 + (Q_L/Q_g)(v_g/v_L)} \tag{3.3}$$

where

α_F = total void fraction determined from flow rate measurements

Q_L = volume flow rate of the liquid phase

Q_g = volume flow rate of the gas phase

v_L = velocity of the liquid phase

v_g = velocity of the gas phase

v_g/v_L = slip ratio

If the flow is in a cylindrical channel of radius R in which the void distribution is axially symmetric, the total void fraction can also be expressed as

$$\alpha = \frac{\int_0^R r\,\alpha(r)\,dr}{\int_0^R r\,dr} \qquad (3.4)$$

$$= \frac{2}{R^2}\int_0^R r\,\alpha(r)\,dr$$

and defining $y = r/R$, Equation (3.4) becomes

$$\alpha = 2\int_0^1 y\,\alpha(y)\,dy\ . \qquad (3.5)$$

By using the conductivity probe to obtain a series of current measurements along a radius of the channel, $\alpha(y)$ is determined by employing Equation (3.2), and the total void

fraction α_p (based on conductivity probe measurements) can then be obtained from Equation (3.5). Assuming that accurate values for the flow rates and slip ratios can be obtained, agreement between α_F and α_p implies the validity of Equation (3.2). It is recognized that agreement between α_F and α_p obtained in this manner is necessary but not sufficient to verify Equation (3.2); however, since the general variation of void fraction with radius for the proposed flow conditions is known from other investigations,[36,41,42] if, as is shown to be the case, $\alpha(y)$ agrees with these previous measurements and also provides agreement between α_F and α_p, Equation (3.2) is considered to be verified.

C. Probe Construction and Calibration

The electrodes of the conductivity probe were of No. 26 platinum wire passed through a 1/16-inch diameter insulating tube and soldered to the electrical leads. The leads and the solder joints were then covered with a plastic 1/8-inch diameter tube and the ends sealed with epoxy. The construction details of the probe are shown in Fig. 3.1 and 3.2.

To perform the calibration discussed in the preceding section, a cylindrical flow channel was constructed into which air and water could be simultaneously introduced at predetermined rates.

The test section consisted of a vertical lucite tube with a 3/4-inch internal diameter. The air and water were mixed 12 pipe diameters upstream of the probe insertion point. A pump circulated the water from a 10,000 gallon reservoir

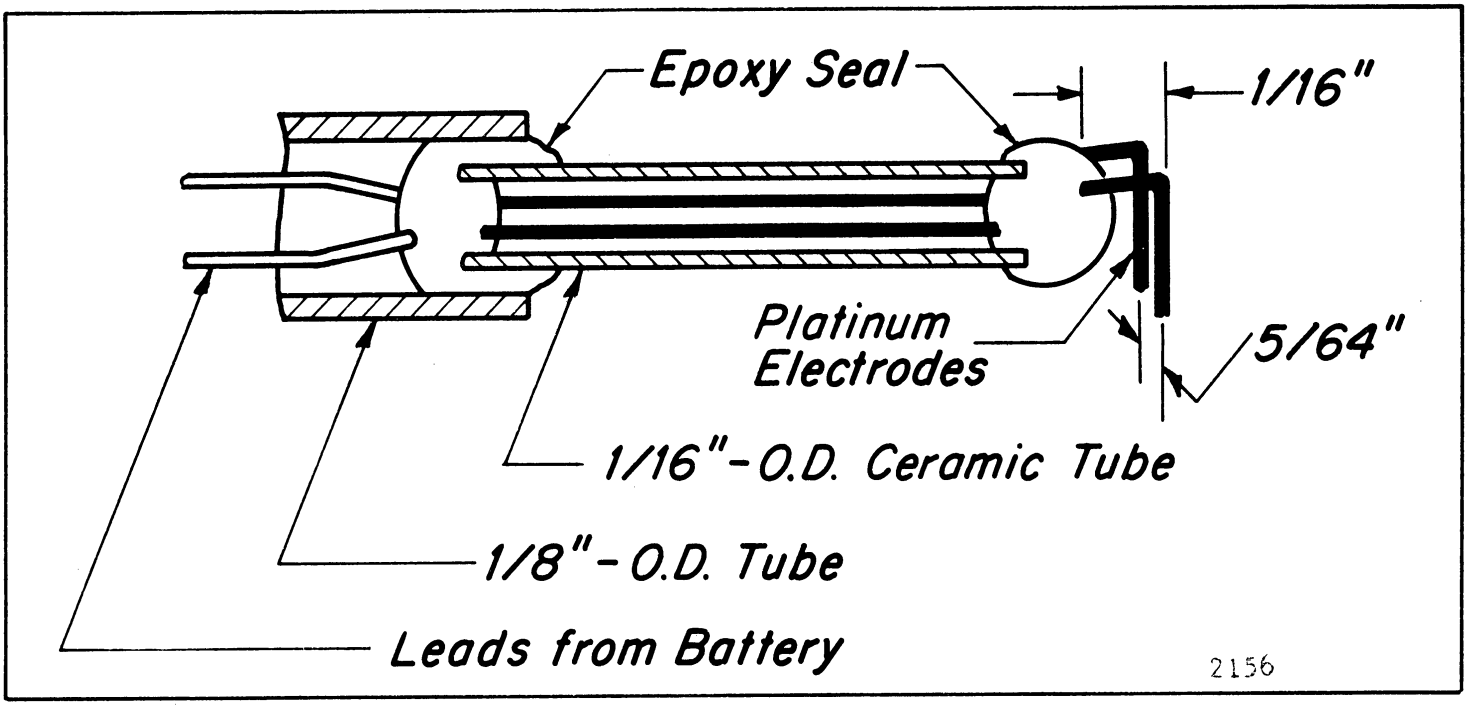

Fig. 3.1 - Sketch of Probe Construction.

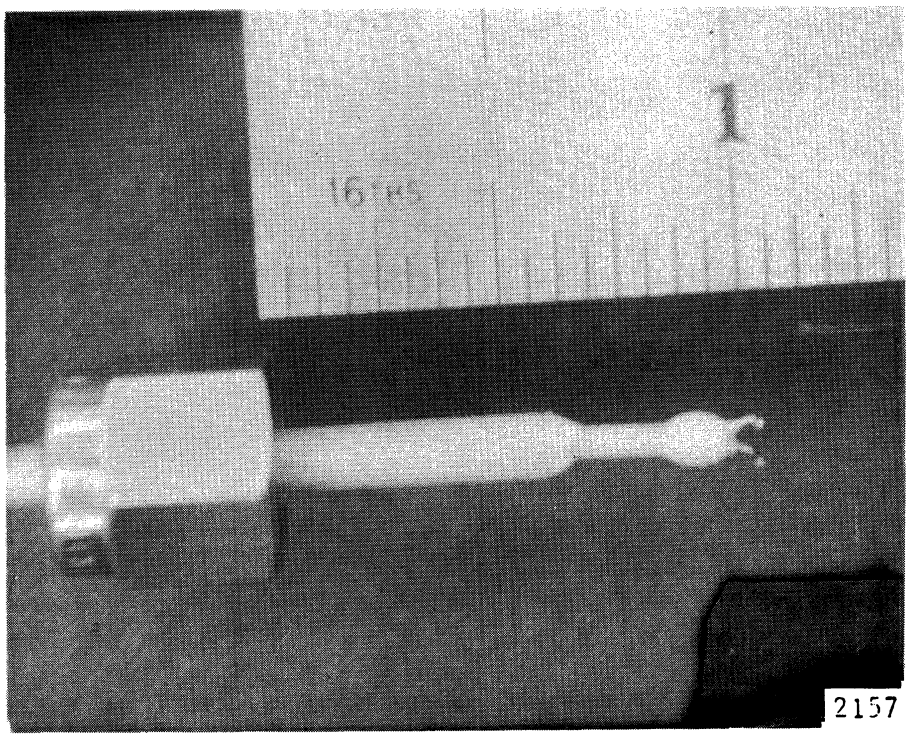

Fig. 3.2 - Photograph of Conductivity Probe.

and provided liquid velocities at zero void fraction up to 20 ft/sec in the test section. The air was taken from the laboratory 100 psig supply line and fed into the water stream through a 1/16-inch diameter orifice in the end of a 1/4-inch diameter tube. The arrangement of the mixing section is shown in the sketch of Fig. 3.3.

The flow rates of the air and water were measured with float-type meters and the static pressures in the test section and the air supply line were measured with standard bourdon-tube gauges. The temperatures of the water and air were measured with gauges inserted into the supply lines. It was assumed that the temperature of the air in the test section was the same as that of the feed water.

The potential to the probe electrodes was supplied by two 22.5 volt dry cell batteries in parallel and the probe current measured by a milliammeter.

With the air and water flow rates set at the desired levels, the test section was traversed radially by the probe which was inserted into the flow 8.19 inches above the entrance to the test section. The probe was positioned radially by a micrometer head and current readings obtained every 0.05 inches across the tube. The portion of the traverse from the center of the tube to the far wall was designated as radius number 1, and from the center to the near wall as radius number 2. In each run two complete traverses were made with measurements every 0.10 inches; the second series of

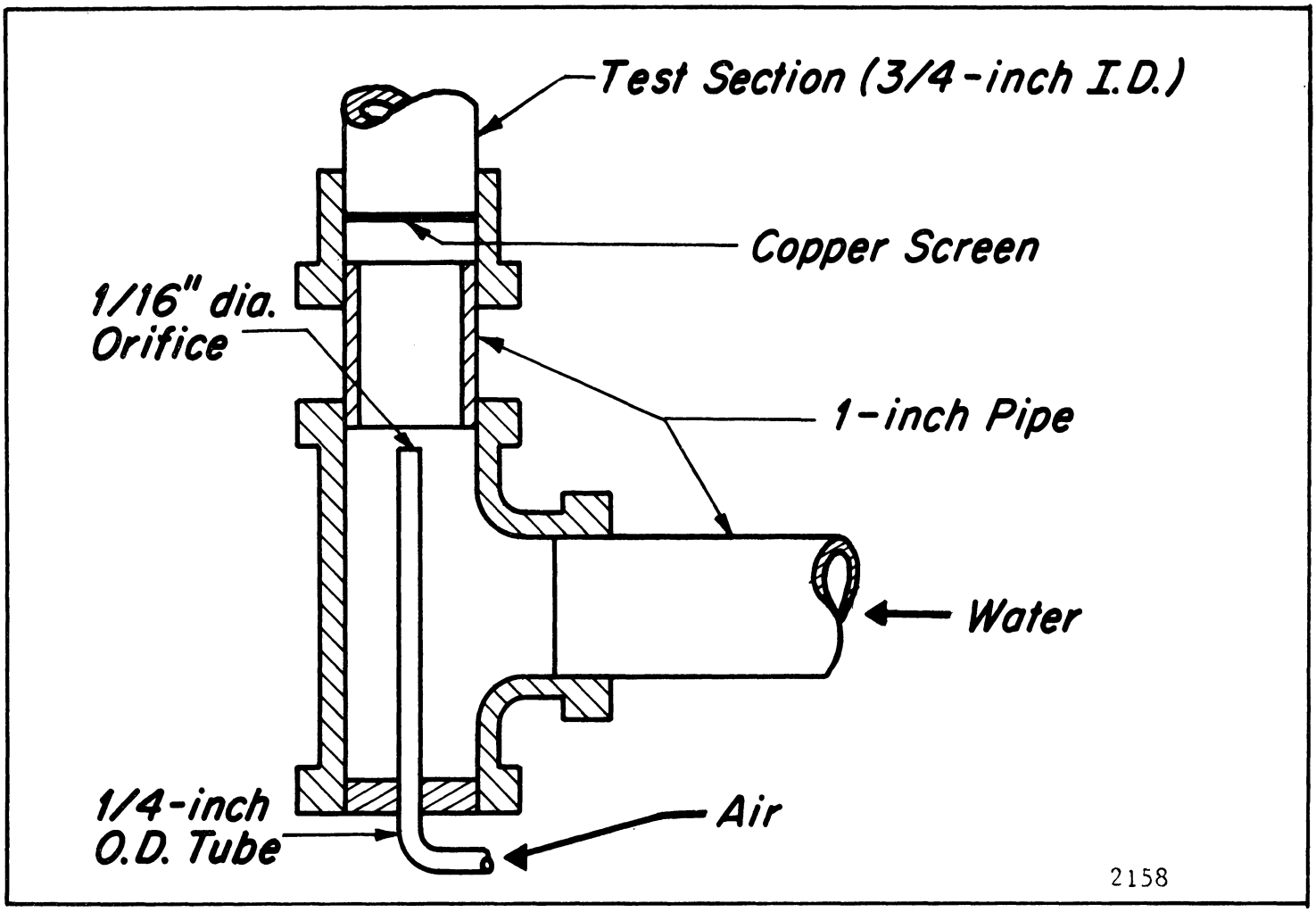

Fig. 3.3 - Sketch of Mixing Section.

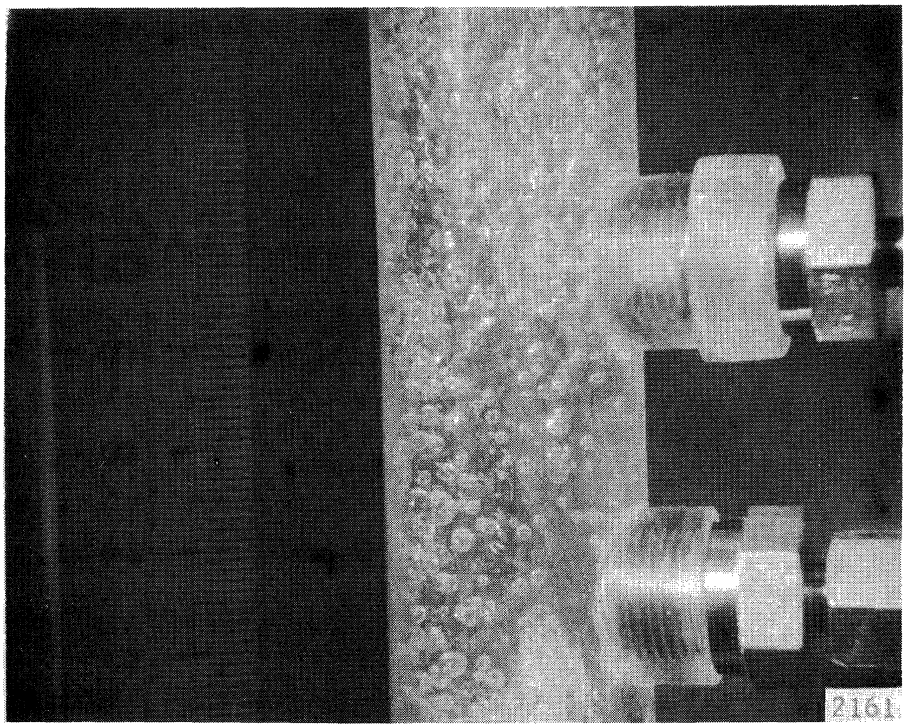

Fig. 3.4 - Representative Flow Conditions with a Void Fraction of Approximately 0.40

measurements staggered 0.05 inches from the first. This procedure provided a check of the consistency and reproducibility of the data.

The water flow rates were varied from 37.7 to 53.4 lb/min and the air flow ranged from 0.018 to 0.252 lb/min giving a range of total void fractions from 0.264 to 0.585, and local void fractions from 0.19 to 0.77. Fig. 3.4 gives a visual indication of the void distribution and flow conditions representative of the tests.

The upper limit of the total void fraction was determined by the maximum air flow rate attainable through the 1/16-inch orifice. For void fractions less than those indicated above, the axial asymmetry was great enough that the evaluation of Equation (3.5) could not be accomplished with a reasonable level of confidence so that no data were taken outside this void fraction range.

With zero void fraction and the probe positioned at the center of the channel, the probe current I_o was recorded for water velocities from about 0.7 ft/sec to 20 ft/sec. The results of these tests are shown in Fig. 3.5, where the probe current is seen to decrease by about one milliamp over this velocity range. The probe current I_{oo} at zero velocity was recorded as approximately 15.5 milliamps; however, the fluctuations of the current due to bubble formation on the electrodes makes this value uncertain. Since the probe current is more sensitive to velocity

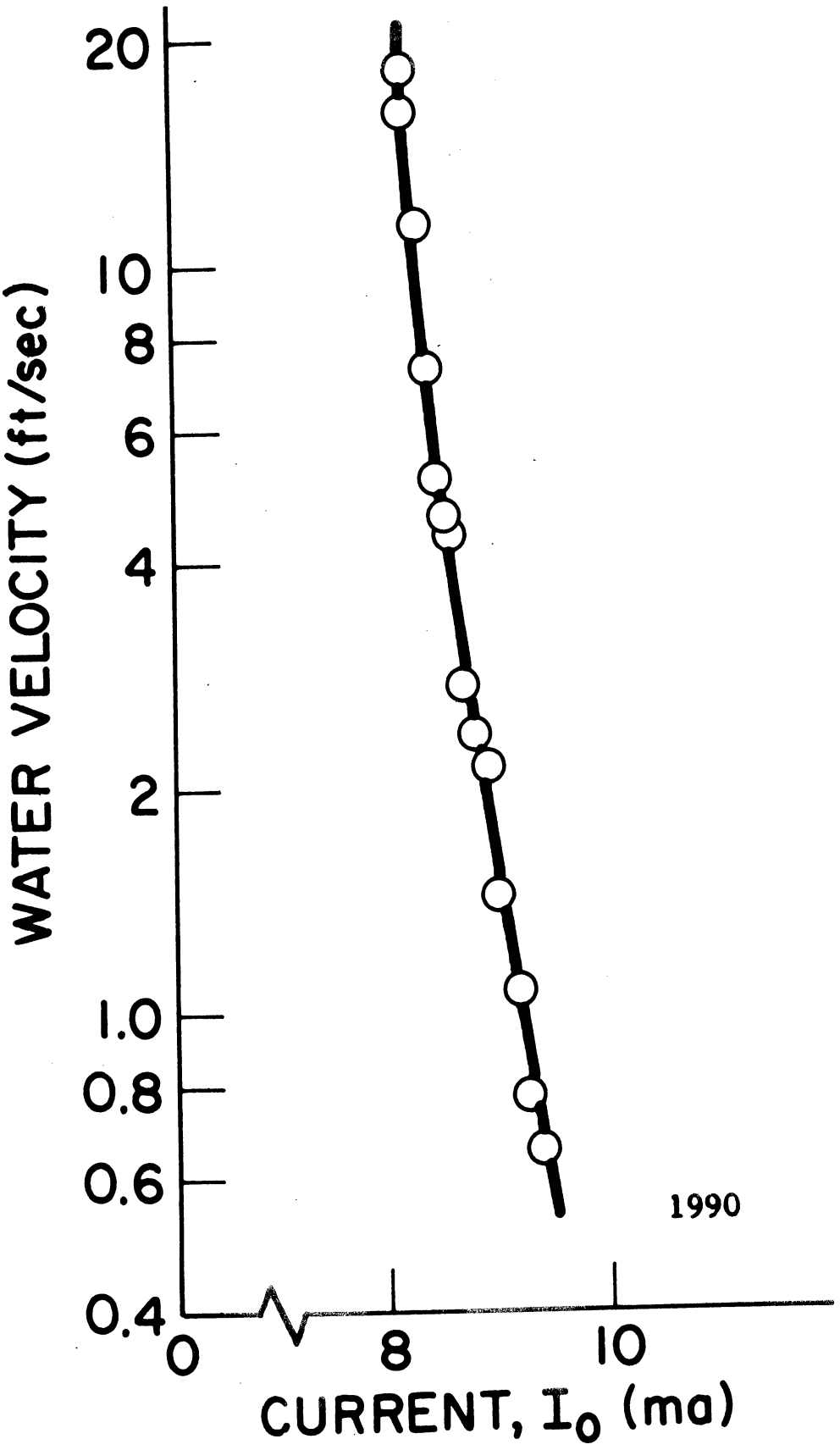

Fig. 3.5 - Variation of Probe Current with Water Velocity with no Voids.

variations at the lower water velocities, the tests to measure void fraction were made at water velocities above 3 ft/sec. The value of I_o used in the computation of local void fractions was that measured for the water velocity corresponding to the specified flow rate with zero voids, i.e., the "superficial" water velocity. Some slight error may have been introduced by using this value of I_o since the water velocity in the test section is increased when air flow is added.

D. Results and Analysis

In calculating the total void fraction α_F based on flow rates, the slip ratio used in Equation (3.3) was obtained from the empirical relation due to Richardson[43]

$$v_g/v_L = 37(x)^{1/2} \qquad (3.6)$$

where

$$x = \frac{\text{Mass flow rate of the gas}}{\text{Total mass flow rate}} = \text{Quality}$$

Equation (3.6) was obtained for flow in horizontal tubes at atmospheric pressure and was later verified by Fohrman.[44] Petrick[37] obtained slip ratios for two-phase vertical up-flow which agree reasonably well with Equation(3.6). There was sufficient dispersion in Petrick's data, however, to introduce some uncertainty in the values obtained from

this relation. Nevertheless, it is felt that Richardson's equation gives sufficiently reasonable estimates of the slip ratios to test the validity of the proposed relationship between the conductivity and void fraction of a two-phase flow. Experimental verification of Equation (3.6) is limited to a minimum value of quality of 0.00078 where the slip ratio is approximately unity. In calculating α_F for Run No. 8, in which the quality was 0.0004, the slip ratio was therefore taken to be unity since there is no physical argument to justify a slip ratio of less than unity in this type of flow.

The values of the local void fractions obtained with the probe, using Equation (3.2), are listed in Table 3.1, and representative radial distributions are plotted as a function of the non-dimensional radius y in Fig. 3.6. The two data points (one for R_1 and one for R_2) for a given value of y were made on different traverses as were adjacent points on the same radius. Thus, the smooth variation of the data for the two radii indicate the consistency and reproducibility of the probe measurements. The divergence of the data for R_1 and R_2 with increasing radius, which is observed in some cases, probably reflects the probe disturbance of the flow, the magnitude of which depends on probe extension, since the probe was always inserted from the same side of the test section.

Using Equation (3.5), the total void fraction α_p was computed from these data by numerically integrating under

TABLE 3.1

VALUES OF LOCAL VOID FRACTIONS OBTAINED USING $\alpha = 1 - I/I_o$

Run No. 1		
$I_o = 8.6$ ma		
$\alpha_F = .415$		
r/R	R_1	R_2
.0187	.678	
.115	.678	
.152		.660
.248	.672	
.286		.638
.382	.614	
.418		.562
.515	.555	
.552		.474
.648	.439	
.685		.368
.780	.322	
.820		.278

TABLE 3.1 (continued)

Run No.	2		3		4		5		6		7		8	
I_o(ma)	8.7		9.1		8.9		9.0		8.7		8.7		10.8	
α_F	.470		.476		.498		.524		.530		.585		.262	
r/R	R_1	R_2	R_1	R_2	R_1	R_2	R_1	R_2	R_1	R_2	R_1	R_2	R_1	R_2
.0665	.770	.776	.730	.730	.750	.750	.817	.828	.860	.862	.911	.906	.245	.230
.200	.747	.753	.720	.697	.750	.716	.789	.811	.845	.845	.902	.897	.245	.220
.333	.724	.713	.697	.652	.716	.693	.756	.778	.828	.816	.887	.870	.250	.190
.466	.644	.678	.652	.562	.682	.557	.689	.722	.759	.782	.851	.822	.245	.160
.600	.582	.553	.550	.460	.591	.512	.578	.589	.702	.667	.794	.748	.266	.103
.734	.425	.472	.426	.372	.432	.398	.489	.398	.540	.540	.690	.621	.188	.066
.866	.345		.315	.180	.318	.186	.356	.276	.438		.530	.460	.130	.037

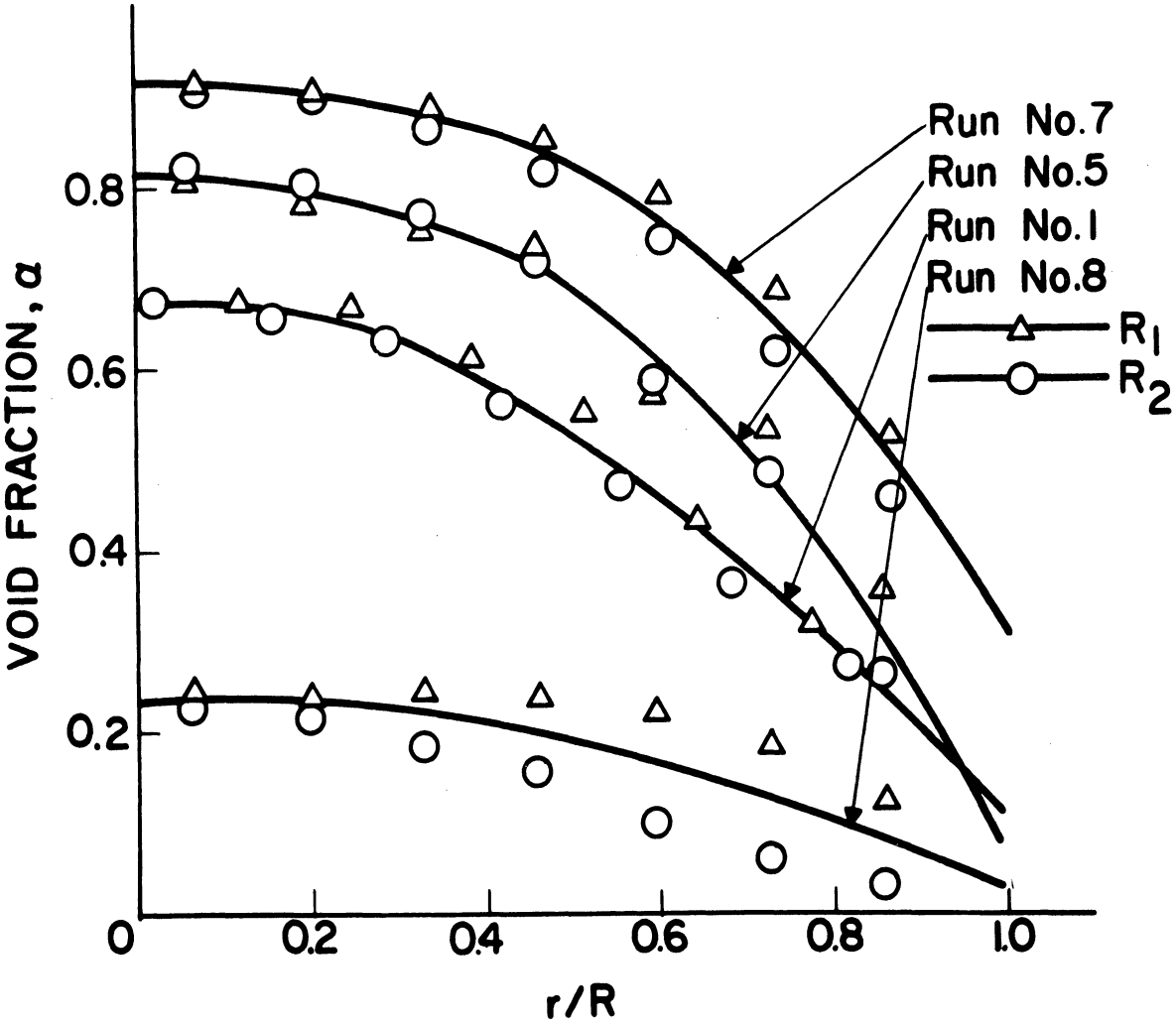

Fig. 3.6 - Representative Radial Distributions of Void Fraction Obtained with the Conductivity Probe and the Use of Equation (3.2).

the distribution curves. The results of the calculations are listed in Table 3.2, where they are compared to the results of the flow meter determinations. The per cent error listed in Table 3.2 was computed assuming the flow meter data to be accurate.

TABLE 3.2

COMPARISON OF TOTAL VOID FRACTION DETERMINATIONS USING $\alpha = 1 - I/I_o$

Run No.	W_L(lb/min)[a]	W_g(lb/min)[b]	X	α_F	α_P	% Error
1	53	.0615	.00116	.415	.389	- 6.26
2	53	.1010	.0019	.470	.476	1.28
3	42	.0814	.00194	.476	.418	-12.2
4	37.75	.0800	.00212	.498	.444	-10.8
5	42	.1220	.00289	.524	.520	- 0.76
6	53	.1810	.0034	.53	.578	8.86
7	53.4	.2520	.0047	.585	.646	10.4
8	44.1	.0175	.0004	.243	.176	-27.6

a. Mass flow rate of water
b. Mass flow rate of air

The comparison of the two determinations is displayed graphically in Fig. 3.7, where it is seen that the probe measurements tend to be too high for α greater than 0.5, and too low

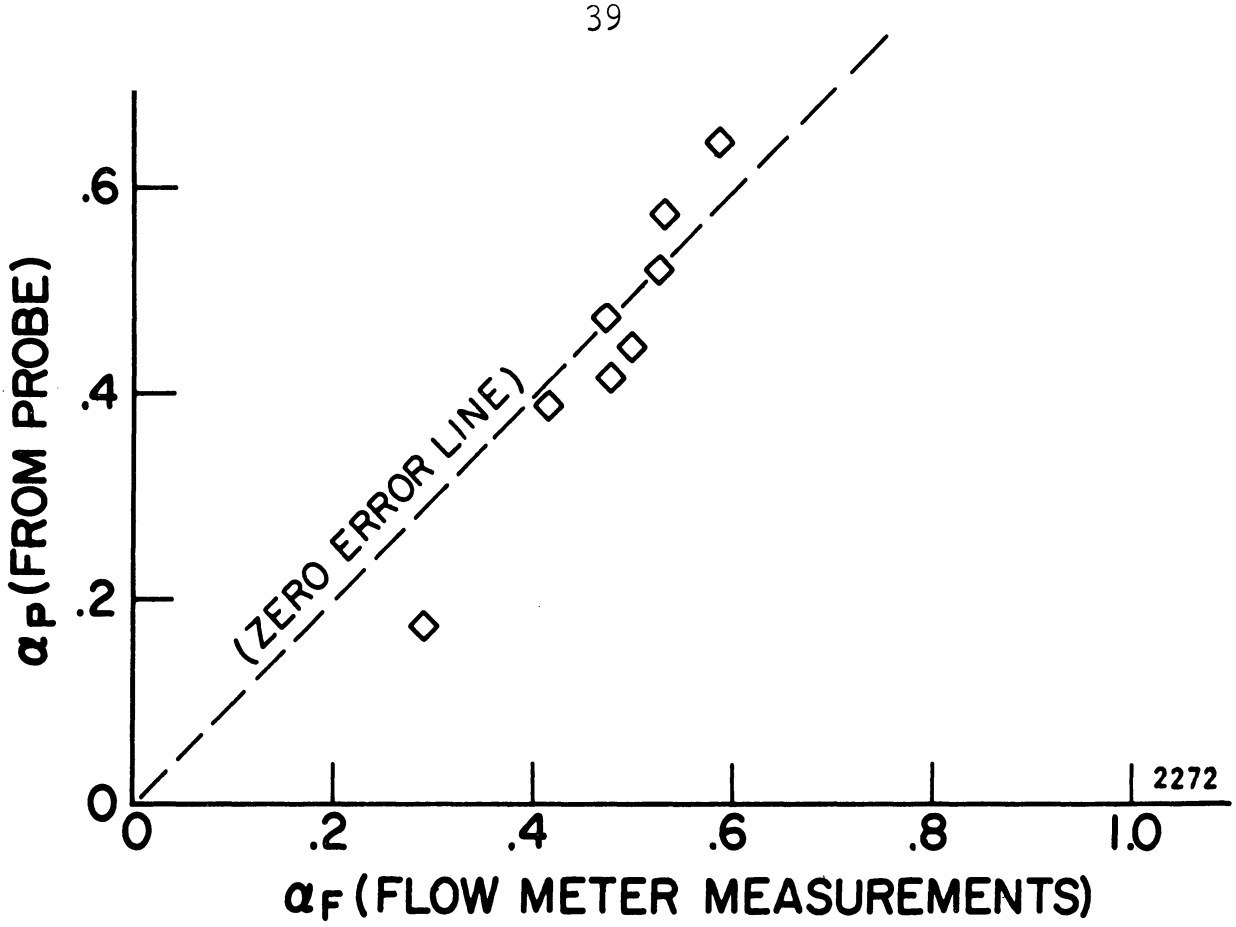

Fig. 3.7 - Comparison of Void Fractions Determined by Flow Rates and by the Conductivity Probe using Eq. (3.2).

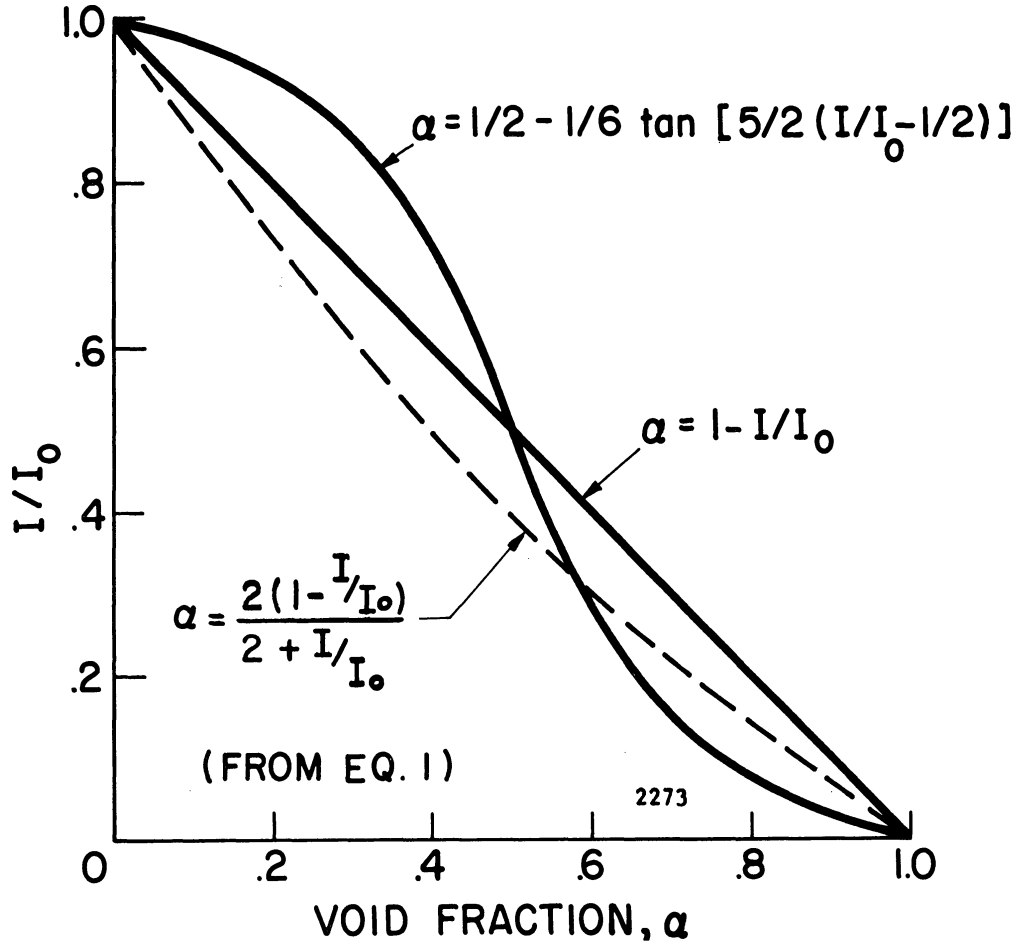

Fig. 3.8 - Comparison of Empirical and Analytical Relationships Between Probe Current and Void Fraction.

for α less than 0.5. Although the accuracy of these measurements (maximum error of about 27%) is within the nominal range of accuracy of gamma-ray attenuation methods, the trend of the variation noted in Fig. 3.7 indicates that an alteration of the relationship between probe current and the void fraction would achieve better agreement between the two sets of measurements. An empirical relation in the form

$$\alpha = 1/2 - 1/6 \tan [5/2 \ (I/I_o - 1/2)] \qquad (3.7$$

was found to reduce the difference between the flow meter and probe measurements to a maximum of 8% over the entire range of void fractions considered.

A plot of this empirical relation is shown in Fig. 3.8, where it is compared to the linear relation predicted by Equation (3.2) and Maxwell's relation (Eq. 3.1). This comparison indicates that Equation (3.1) will give reasonable results for I/I_o less than 3.5 but will predict very low values of void fractions for higher values of the current ratio.

The radial distribution of voids in the pipe obtained by use of Equation (3.7) is shown in Fig. 3.9 for four representative runs. A comparison of the total void fractions obtained from the empirical relation (Eq. 3.7) and those obtained from the flow meter measurements are shown graphically in Fig. 3.10. This comparison, with the corresponding errors, is shown in tabular form in Table 3.3.

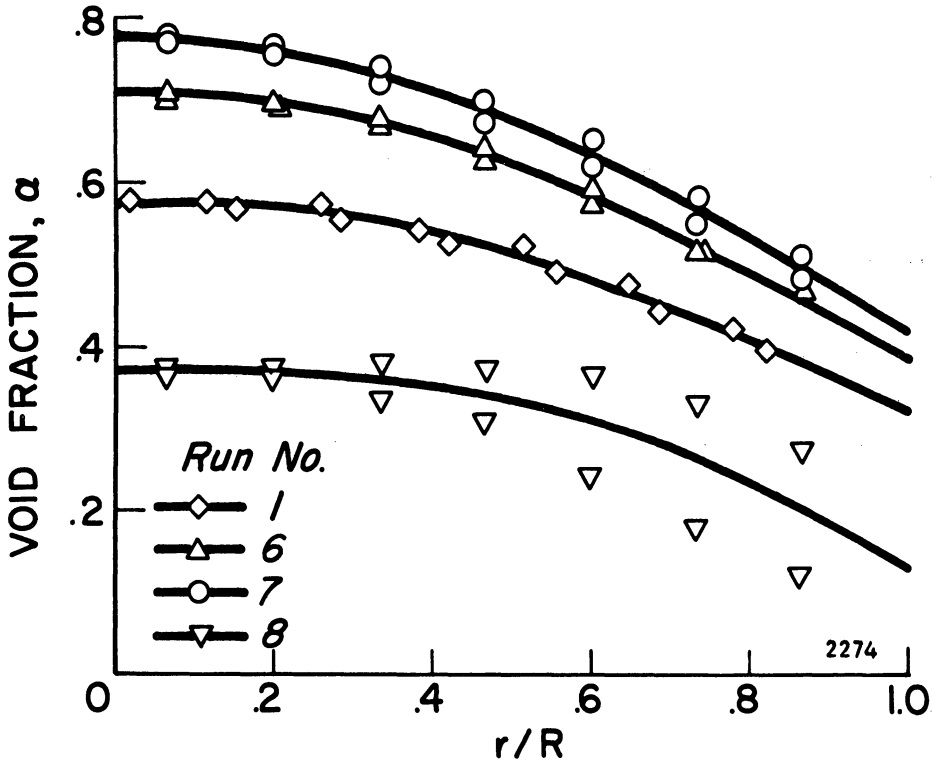

Fig. 3.9 - Radial Distribution of Void Fraction Obtained from Equation (3.7).

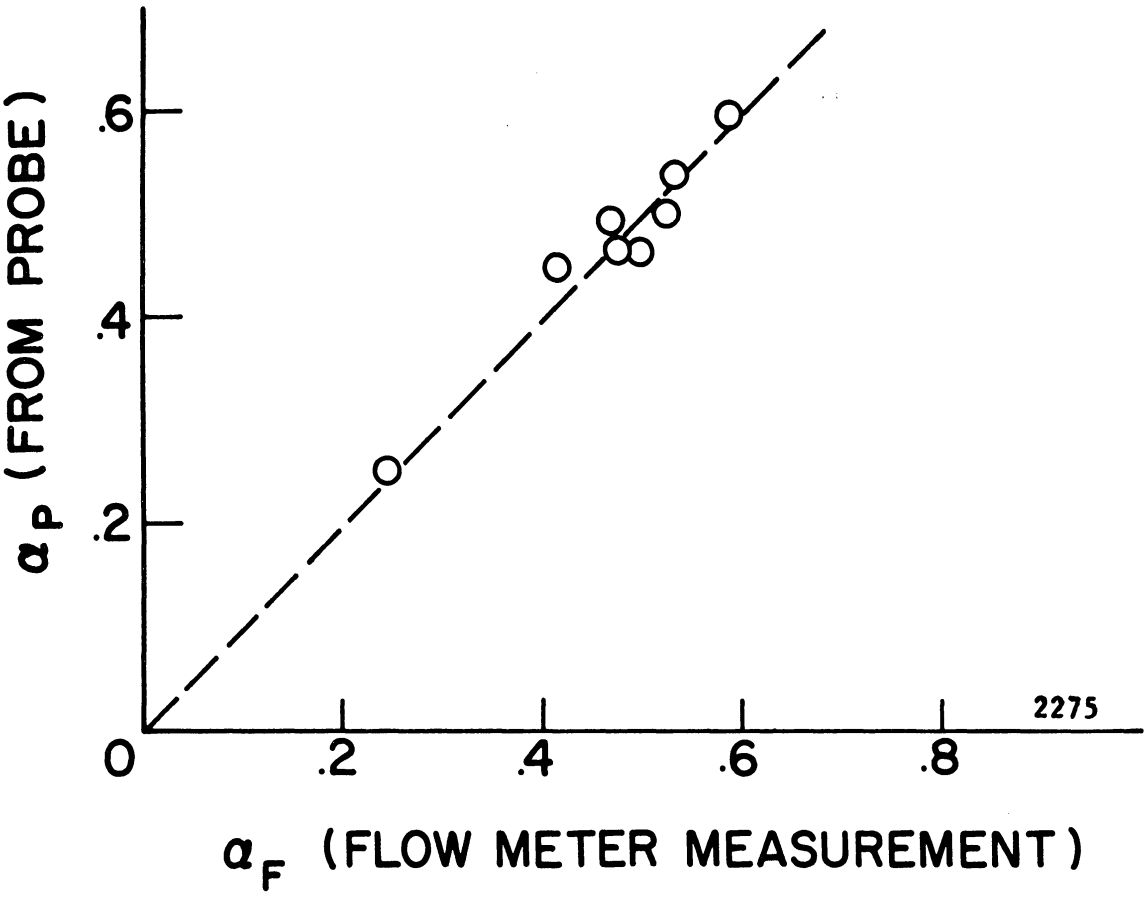

Fig. 3.10 - Comparison of Void Fractions Determined by Flow Rates and by Conductivity Probe using Equation (3.7)

TABLE 3.3

COMPARISON OF TOTAL VOID FRACTION DETERMINATIONS

USING $\alpha = 1/2 - 1/6 \tan \left[5/2 \, (I/I_o - 1/2) \right]$

Run No.	α_F	α_p	% Error
1	.415	.448	8.0
2	.470	.495	5.32
3	.476	.467	-2.0
4	.498	.465	-6.62
5	.524	.502	-4.2
6	.530	.540	1.9
7	.585	.588	0.05
8	.243	.262	7.8

CHAPTER IV

OPERATION OF THE TEST FACILITY

A. Start-Up and Operating Conditions

The vortex flow was normally started by the simultaneous injection of air and water into the chamber. With the back pressure control valve fully open, air from the 100 psig laboratory supply line was admitted to the plenum chamber at a low flow rate ($\sim$1.5 lbm/min) sufficient to provide a pressure drop across the unit of 2 to 5 psi (plenum pressure to exhaust pressure). Water from the laboratory supply line was injected at the outer periphery of the vortex at a rate of approximately 1.0 lbm/min. Under these conditions a vortex was rapidly formed that was stable in the sense that a nominal decrease in the water flow rate did not change the apparent characteristics of the vortex except to decrease the flow of water out of the system through the end-plate boundary layers. After start-up of the vortex, the water flow was reduced to about 0.4 lbm/min for the test runs, although long periods of stable operation were observed for water flow rates as low as 0.1 lbm/min.

When the stable vortex was attained, the air supply valve and back pressure valve were adjusted to give plenum pressures P_a ranging from 5 to 50 psig. For each setting of P_a, the exhaust pressure P_E was varied over as wide a range as possible. The minimum value of $\Delta P = (P_a - P_E)$ was about 2 psi for all

P_a and the maximum was 30 psi at P_a = 50 psig. The values of P_a and the corresponding values of ΔP which were selected for the tests are listed in Table 4.1

TABLE 4.1

SELECTED OPERATING PRESSURES

Without Electrodes Installed			With Electrodes Installed		
P_a (Plenum Pressure) (psig)	P_E (Exhaust Pressure) (psig)	ΔP ($P_a - P_E$) (psi)	P_a (psig)	P_E (psig)	ΔP (psi)
10	8	2	25	20	5
10	6	4	25	15	10
10	4	6	25	9	16
20	16	4	35	30	5
20	14	6	35	25	10
20	12	8	35	19	16
20	10	10	35	15	20
20	8	12	50	45	5
25	21	4	50	40	10
25	17	8	50	34	16
25	13	12	50	30	20
25	9	16	50	20	30
30	28	2			
30	24	6			
30	20	10			
30	18	12			

B. Operation Without Electrodes Installed

The facility was first operated with the nozzle ring containing the two 2-dimensional nozzles to verify that the two-phase vortex could be maintained and to develop techniques for visual observations. For the latter purpose, small tracers in the form of colored plastic beads were placed in the flow and the vortex photographed, using a strobe light, in an attempt to determine the velocity of the water.

On the basis of the observations from these initial tests, the second nozzle ring containing 12 nozzles was designed and installed prior to making the detailed measurements of pressure and void fraction distributions. This modification was made to provide a more stable and symmetric flow. The second nozzle ring design was successful in that it provided much greater axial symmetry and permitted the mass flow rate to be adjusted by closing some of the nozzles. While the vortex operated quite well with all twelve nozzles open, it was found that the high air mass flow rate severely limited the operating range of pressures due to limited air aupply available. Four of the nozzles were therefore closed and the final tests made with eight nozzles. The eight-nozzle configuration, showing the relative location of the nozzles to the azimuthal position ϕ, is illustrated in Fig. 4.1.

With the plenum and exhaust pressures set at the desired levels, the static pressure measurements were made at three

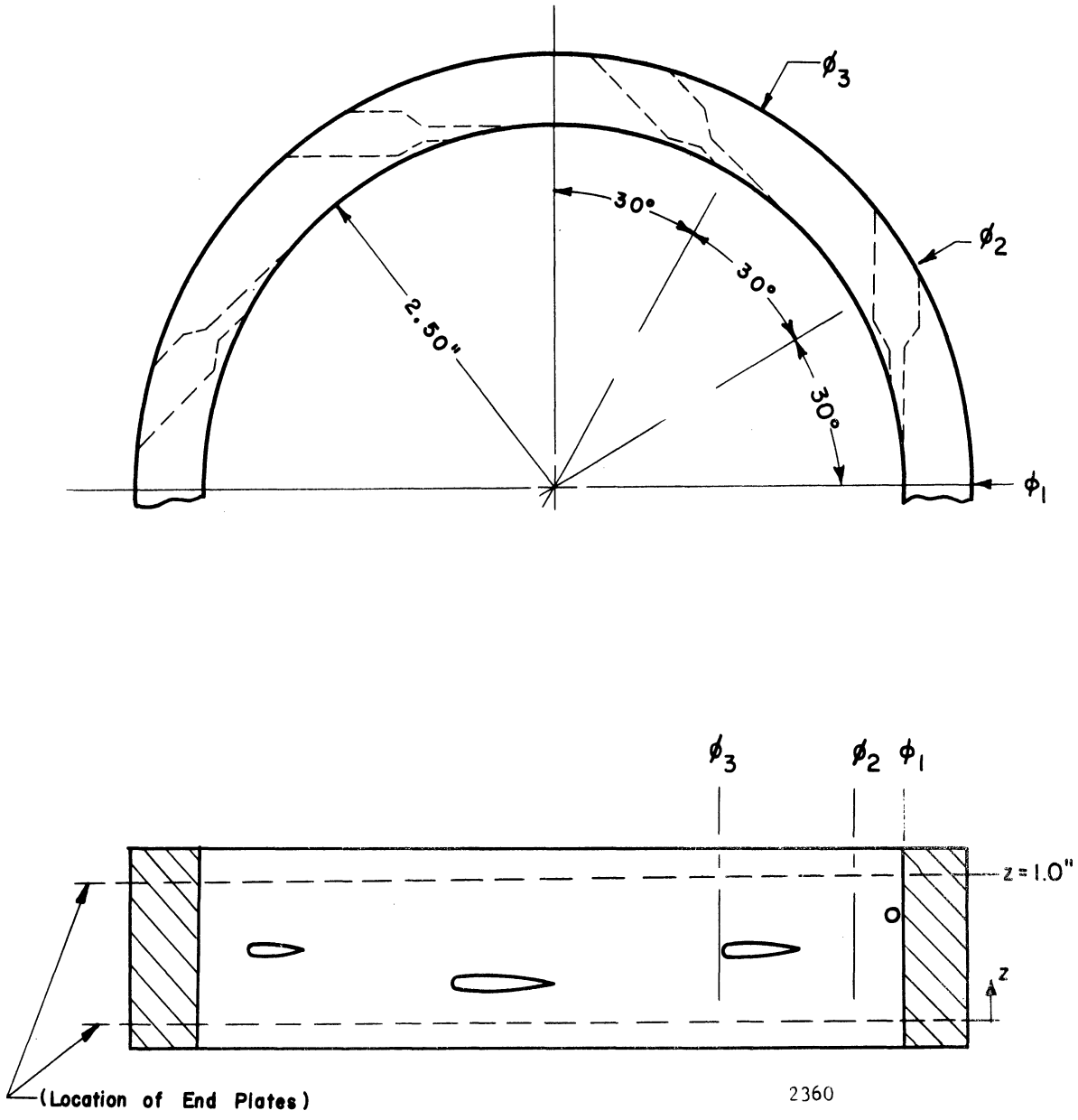

Fig. 4.1 - Sketch of Nozzle Ring showing Nozzle Locations Relative to Ø.

azimuthal positions (ϕ_1, ϕ_2, and ϕ_3, as shown in Fig. 4.1) and six radial positions. The total pressures and void fractions were measured at five axial positions for each radial and azimuthal combination. The radial and axial positions at which the measurements were made are tabulated in Table 4.2.

Prior to making the detailed pressure and void fraction measurements the air flow rates were measured as a function of P_a and ΔP, and the corresponding static pressure in the throat of one of the nozzles was recorded. These measurements were taken at the beginning of the tests to avoid the necessity of repeating the flow rate measurement for each data point.

TABLE 4.2

RADIAL AND AXIAL MEASUREMENT LOCATIONS

Pressure Tap No.	r/r_o (r_o = 2.5 in.)	Axial Position No.	Z (in.)
1	0.975	1	0.125
2	0.900	2	0.250
3	0.825	3	0.500
4	0.750	4	0.750
5	0.675	5	0.875
6	0.600		

By rotating the top plate (containing the pressure taps) of the vortex chamber in increments of 30° relative to the nozzle ring, complete radial traverses (six radial positions) could be obtained in 360° (twelve azimuthal positions). However, considering the axial symmetry provided by the nozzle arrangement, this can be accomplished in 180° (six azimuthal positions) rotation of the top plate, and this latter procedure was used for all pressure and void fraction measurements.

When making total pressure measurements, the probe was oriented so as to measure the tangential component only. Since this type of probe is not highly sensitive to small changes in flow direction, the probe was not used to determine the direction associated with the maximum value of the total pressure at a point in the flow.

After developing the pressure measuring techniques (using the air-bleed system) and the conductivity probe, the only major operating difficulty arose from pressure fluctuations in the air supply line due to the duty cycle of the laboratory compressors. Even with a pressure regulator in the line, the plenum pressure varied on the order of ±4.0 psi if the control valve was not adjusted to regulate the pressure in the plenum during operation; thus a measurement often had to be made several times to assure that the data were obtained under the specified operating conditions.

C. Operation With the Electrodes Installed

In the tests conducted without the electrodes installed, the maximum values of P_a and ΔP, as listed in Table 4.1, were controlled primarily by the pressure drop in the air supply line due to the pressure regulator and flow meter. During the modification of the assembly to install the electrodes and magnetic field coils, the regulator and flow meter were removed from the air supply line and larger pipe was installed. This modification permitted P_a and ΔP to be increased to the values shown in Table 4.1.

With the connectors to the static pressure taps removed from the end plates to permit installation of the magnetic field coils, it was no longer possible to insert probes through the tap holes. An alternate arrangement was made (Fig. 2.5) to insert the probes radially through the plenum ring and nozzle ring walls at the axial mid-point (Z = 0.5 inch) and at the $\emptyset_1$ azimuthal position. Since the radial insertion of the probes at any other axial or azimuthal position would require the probes to pass through one of the nozzles, the total pressure and void fraction measurements were restricted to $\emptyset_1$ at Z = 0.5 inch in this series of tests. Static pressures were measured at five radial positions and three azimuthal positions as in the previous series of tests except that the No. 6 pressure tap was eliminated in the modification of the unit. This tap was eliminated because the inner edge of the electrode plate coincided with the

centerline of the No. 6 tap hole.

After completion of the pressure and void fraction measurements at the pressure settings listed in Table 4.2, the magnetic field coils were installed and the vortex operated in the presence of radial magnetic fields ranging from 200 to 800 gauss. In these tests the variation of the vortex pressures and the conductivity probe current were observed under the influence of both steady and suddenly applied magnetic fields. These tests were performed under both open-circuit and short-circuit conditions of the vortex electrodes.

The open-circuit voltages generated by the vortex in the presence of the magnetic fields was measured as a function of the field strength B, P_a and ΔP. The initial attempts to make these measurements were complicated by the build-up of electrostatic charge on the electrode plates in the vortex. This charge was often 2 to 3 times greater than the open-circuit voltage produced by the vortex. The difficulty arose from making the initial measurements with an oscilloscope which was electrically grounded. When the oscilloscope leads were attached to the vortex electrodes, one electrode was grounded and the oscilloscope then indicated a voltage difference equal to the static charge on the ungrounded electrode. While the voltage produced due to the magnetic field could be measured above this electrostatic bias, the measurements thus obtained were not repeatable within the

desired range of accuracy. It was found that the use of a digital millivolt meter with an electrically floating measuring circuit gave much better reproducibility of the data. When making measurements with this meter, the potential difference across the electrodes due to the unequal electrostatic charge build-up was recorded before and after the magnetic field was applied. If this bias changed more than 1.0 millivolt during the test, the data was discarded and the test re-run. It was found that the minimum variation in the electrostatic bias was obtained when the electrodes were shorted just prior to the tests. The data obtained in this manner was found to be highly reproducible.

CHAPTER V

EXPERIMENTAL RESULTS

A. Visual Observations

Over the range of operating pressures indicated in Table 4.1 and Table 4.2, the two-phase portion of the vortex was observed to terminate at r/r_o = 0.55 to 0.60, depending on the rate at which water was injected. If the water injection rate was low enough that the apparent inner diameter of the two-phase vortex increased much beyond r/r_o = 0.60, the vortex became unstable in the sense that the water carry-over in the exhaust exceeded the water injection at an increasing rate. If, after this type of instability was initiated, the water make-up flow rate was not increased, the liquid fraction in the vortex decreased until the vortex stabilized at a condition resembling the typical gaseous forced vortex. In this region of operation no liquid was apparent in the flow except for a film on the nozzle ring and on the end plates.

In normal operation, the two-phase flow appeared to be a frothy mixture which is commonly referred to as the mist-flow, spray-flow, fog-flow or dispersed-flow regime.[45,46,47] In attempting to use photographic techniques to determine flow patterns and velocities, it was found, for either front or back lighting, that the light reflection from the surface and the dispersion within the flow made it impossible to obtain

photographs which would yield any information about the internal flow characteristics. An indication of the general type of flow which was observed and the degree of azimuthal symmetry obtained is shown in Fig. 5.1.

When the total-pressure probe (0.062 inch diameter) was inserted into the vortex there was no visual indication of substantial disturbance of the flow except in the region immediately down stream of the probe. This disturbance appeared to quickly damp out in the high turbulence. The void fraction probe (0.125 inch diameter) produced a similar effect at the higher values of r/r_o; however, at the two inner tap positions (r/r_o = 0.60 and 0.675) where the probe was near the inner diameter of the two-phase region, some of the water striking the probe was deflected inward and the flow did not recover before the disturbance propagated back on itself. This disturbance increased over a period of 10 to 15 seconds at which time the flow again reached a steady-state condition. During this transient period, the current of the conductivity probe decreased to about 20% of the maximum observed value after a rapid insertion.

During the second series of tests (with electrode plate installed), a tuft, about 0.25 inches long on the end of a 0.062 inch diameter tube, was inserted radially into the flow. This was done in an attempt to observe the direction of the air flow exiting from the two-phase region. These observations were made at P_a = 50 psig and ΔP = 16 and 20 psi. The air at these conditions was observed to exit from the

two-phase region (at $r/r_o = 0.55$) at an angle of 20° to 25° with the tangent at that point.

B. Air Flow Rates and Injection Velocities

The mass flow rate $\dot{m}$ of the air was measured directly by use of the flow meter and was also calculated, assuming an isentropic expansion, using the plenum pressure P_a and the static pressure measured in the throat of the nozzles. These results are given in Table 5.1. With one exception, the calculated flow rates are higher than those measured with the flowmeter as would be expected since the calculation is based on the isentropic ideal case. The measured values have an average deviation from the calculated values of 4.9% implying a nozzle efficiency of approximately 90% which is common in this type of nozzle. The magnitude of the mass flow rates indicates that the mass ratio of the input air flow to water loss is on the order of 10 and the corresponding volume separation ratio is about 10^4. These quantities are important in conjunction with the cavity reactor concept.

Assuming that the air flow through the nozzles is adiabatic, the mass continuity equation and the ideal gas law predict that the ratio $P_a/\dot{m}$ is a unique function of the pressure ratio P_a/P. Taking P as the nozzle throat pressure and assuming that it is approximately the same as the nozzle exhaust pressure P_o (the static pressure at $r/r_o = 1$),

these ratios are plotted in Fig. 5.2, where it is seen that they are uniquely related as expected. Although this correlation gives no new information concerning the air mass flow rates, it gives an indication of the accuracy of the measurements, since all three variables were experimentally determined. The success of the correlation also provides justification for using the continuity relation and the perfect gas law and assuming an adiabatic process in the calculation of the air velocity in the nozzle throat. The result of the velocity calculations is shown in Fig. 5.3 where the velocity is plotted as a function of the pressure ratio P_a/P_o.

C. Static Pressure Distributions

During the tests without the electrodes installed in the vortex chamber (test series No. 1), the radial distributions of the static pressure were measured at the three azimuthal positions indicated in Fig. 4.1. Representative results of these measurements are shown in Fig. 5.4 to indicate the variation of P with $\emptyset$ as a function of r/r_o, P_a and ΔP. From these data it is seen that the maximum variation of P with $\emptyset$ is about $\pm 10\%$ near the outer radius. This dispersion near r_o was expected due to the discontinuities in the flow resulting from discrete nozzle locations. With decreasing R the data dispersion with $\emptyset$ decreases indicating that the air from the nozzles becomes more uniformly dispersed in the flow.

The radial distributions of P averaged over Ø are shown in Fig. 5.5 through 5.8 for all of the selected operating conditions. The distributions are seen to vary smoothly from maximum values of magnitude and slope at the outer radius to minimum values at the innermost position at $r/r_o = 0.60$. In each case the magnitude of the static pressure at $r/r_o = 0.60$ is less than 0.2 psi above the exhaust pressure which implies that the air has lost most of its angular momentum at this point. For $P_a = 10$ psig (Fig. 5.5) the pressure at $r/r_o = 0.60$ was measured to be below the exhaust pressure P_E. This seems impossible since no diffuser action can be expected in this portion of the vortex and it may be due to error in reading the pressure gauge used to monitor the back pressure. The value of the static pressure P_o at $r/r_o = 1$ was determined by extrapolating the curves to the outer radius.

For the tests with the electrode plates installed (test series No. 2), the static pressure traverses could be taken only from $r/r_o = 0.675$ to the outer radius since the innermost pressure-tap at $r/r_o = 0.60$ was eliminated in the modification of the unit. The resulting distributions are displayed graphically in Fig. 5.9, 5.10 and 5.11. The purpose of the second series of tests was to obtain data at the higher values of P_a which could be attained due to modification of the air supply system. The pressure distributions at the lower pressures were not expected to change from the previous tests. Measurements at $P_a = 25$ psig were included, however, to compare

the results with those of the earlier tests. Comparison of the results of the two sets of measurements at this P_a show very good agreement as seen in Fig. 5.9 where the results of the first series of tests at $\emptyset_1$ and ΔP = 16 psi are repeated for comparison.

Examination of the static pressure distributions suggests that a function of $(P - P_E)$ normalized by the maximum pressure drop $(P_o - P_E)$ would provide a correlation of the pressure with the radius. A plot of the ratio $(P - P_E)/(P_o - P_E)$ was found to be a unique function of r/r_o, as shown in Fig. 5.12, for all P_a and ΔP for both series of tests. The close correlation obtained by the use of this ratio is rather impressive when it is considered that the pressure differences used in the ratio are often quite small, and obtained as the difference of two relatively large experimentally determined values. This effect is most prominent at the lower values of r/r_o where the values of $(P - P_E)$ are on the order of 1% of P.

D. Total Pressure Distributions

The radial distributions of the total pressures for two representative values of P_a and ΔP showing the results for all five axial positions is displayed in Fig. 5.13, 5.14 and 5.15 for the azimuthal positions $\emptyset_1$, $\emptyset_2$ and $\emptyset_3$ respectively. The effect of the nozzle proximity is quite evident in the plots. In Fig. 5.13 the data points for Z = 0.75 are much

higher than the average at the outer radius, reflecting the fact that the radial traverse at this Z and Ø terminates at a nozzle outlet. The traverses for $Ø_2$ in Fig. 5.14 show the same effect, to a lesser degree, for Z = 0.50 due to the nozzle 15° upstream at that Z position. The traverses for $Ø_3$ show a great deal of scatter at intermediate values of r/r_o for the low Z positions. This dispersion is due to the air from the nozzle 30° upstream of $Ø_3$ moving radially inward (as observed visually) so that when it reaches $Ø_3$ the principal effect is most prominent at r/r_o values from 0.8 to 0.9.

The axial distribution of the total pressure at the outer radius at the $Ø_1$ position is shown in Fig. 5.16 to demonstrate the effect of the nozzle at that location for three values of ΔP. The variation of the axial distributions with radius at this same Ø is presented in Fig. 5.17 for six radial positions (including that used in Fig. 5.16) at a constant ΔP. It is evident from these results that at r/r_o = 0.90 the principal effect of the nozzle at $Ø_1$ has moved downstream toward $Ø_2$. The radial distributions of the total pressure averaged over Ø and Z for all the tests in the first series are plotted in Fig. 5.18 and 5.19. These distributions display more dispersion of the data than do the static pressure distributions due to the discontinuities resulting from the nozzles and disturbances resulting from inserting a probe into the flow. It is noted that the total pressure for P_a = 10 psig (Fig. 5.19) and a ΔP of 4 psi at

r/r_o = 0.6 is very nearly equal to the exhaust pressure of 6 psig which indicates that a small error in measurement or the setting of P_E could account for the invalid result obtained for the static pressure at this point (Fig. 5.5).

The radial distributions of total pressure for the second series of tests are displayed in Fig. 5.20, 5.21 and 5.22. These traverses were restricted to $\emptyset_1$ and Z = 0.50 since axial access to the vortex was not possible because of the electrode plates (only one radial access port could be attained without disrupting one or more of the nozzles). As is evident in these plots, advantage was taken of the ability to make measurements at several more radial positions than was possible in the first series of tests.

In Fig. 5.20 the results of the first series of tests for ΔP = 16 psi at $\emptyset_1$ is superimposed on the results of the second test series to show the agreement between the two sets of data. Near the outer radius at r/r_o = 0.975 the radial probe gave slightly ($\sim$5%) higher values which probably results from the difference in the drag exerted on the vortex in the two cases. In the axial insertion, the probe extends 0.62 inches into the flow to measure P_t at r/r_o = 0.95 while the radial probe was inserted only 0.12 inches to make a measurement at the same point.

The data for each radial distribution of the total pressure in the second series of tests was obtained during the same test run in contrast to the first series of tests

in which each data point in a radial distribution was obtained during a different run. The agreement between these two sets of data indicates the degree to which operating conditions and measurements could be repeated.

E. Void Fraction Measurements

In the first series of tests the void fraction distribution throughout the two-phase region did not change, within the accuracy of the measurements, as a function of P_a and ΔP. This is illustrated in Fig. 5.23 for Z = 0.75 at $\emptyset_1$ over a wide range of P_a and ΔP. This distribution, which exhibits the greatest variation with radius, would be expected to show the greatest data dispersion. The close grouping of the data points observed in this plot is typical of all the void fraction measurements in this test series. The data displayed in Fig. 5.23 is also encouraging in that the void fraction approaches a value of 1.0 at r/r_o = 1.0 where the traverse intersects a nozzle outlet.

Since the void fraction appears not to be a function of the pressures over this range of operating conditions, the results were averaged over P_a and ΔP for each axial, radial and azimuthal combination. Due to the disturbance of the flow caused by the void fraction probe at the two innermost tap locations (r/r_o = 0.60 and 0.675) the data for these radial location were discarded and, after the first few tests, no attempt was made to obtain void fraction measurements at these locations.

The radial distributions of void fraction (averaged over P_a and ΔP) are shown in Fig. 5.24, 5.25 and 5.26 as functions of ϕ and Z. In Fig. 5.27, 5.28 and 5.29 the axial distributions are displayed as functions of r/r_o and ϕ. In these axial profiles the effect of the nozzle locations is quite evident (as in the case of the axial profiles of the total pressures) and shows an increasing aximuthal displacement with decreasing radius. Since the probe was free to move to any axial position at a given radial location, the approximate axial location of the maximum void fraction value was recorded during each traverse and is indicated on the plots by a cross.

In the second series of tests the measurements were restricted to ϕ_1 and Z = 0.50 as in the case of the total pressure measurements. The resulting radial distributions for representative values of P_a and ΔP are shown in Fig. 5.30, 5.31 and 5.32. Although the variation of the void fraction appears to be fairly insensitive to changes in both P_a and ΔP as before, these data do show some tendency for the void fraction to increase with increasing ΔP for r/r_o greater than 0.85. In Fig. 5.33, where the distributions are presented for a constant value of ΔP with various values of P_a, it is seen that for r/r_o greater than 0.85 the void fraction tends to decrease with increasing P_a. Although these trends are quite definite and uniform, the maximum variations are less than $\pm 10\%$ which is within the range of error of the probe and any conclusions based on these observations would be only speculative without a knowledge of the void variation with ϕ and

Z at these pressures.

Since the static pressure measurements were limited to a minimum radial position of $r/r_o = 0.675$ in this series of tests, the bulk of the void fraction measurements were made over this same range. For $P_a = 50$ psig, however, the void fraction probe was inserted to its maximum depth which permitted measurements to be made at values of r/r_o as low as 0.45, as indicated in the plots of Fig. 5.32 and 5.33. The validity of the data for r/r_o less than 0.55 is in doubt since the probe tip was in a relatively clear region and the visability was sufficient to observe liquid droplets trailing from its tip. It is possible that much of this liquid originated in the regions of higher liquid concentration and traveled along the probe to the tip due to the radial air flow. If this were the case, the observed void fractions in this region are too low.

The radial distribution of the void fraction averaged over Ø and Z for the first series of tests is shown in Fig. 5.34 superimposed upon the average values obtained in the second series of tests. To obtain a representative radial distribution, the results of the two series of tests were not averaged since the second set of data is restricted to one value of Ø and Z. For r/r_o less than 0.75 the flow appears to have little variation with Ø judging from the results of the total pressure measurements. An examination of the axial void fraction profiles suggest that the Z dependence of the flow is also insensitive to Ø-variations at the small values

of r/r_o. Assuming this to be the case, a fairly representative distribution of the void fraction over the entire two-phase region is obtained by joining the distribution for low r/r_o obtained in the second series of tests (radial probe) to the average distribution obtained in the first series (axial probe) at the higher values of r/r_o. The resulting estimate of the radial distribution is shown by the solid curve in Fig. 5.34 where it is seen that the two distributions join quite smoothly at $r/r_o = 0.7$.

F. Operation with the Magnetic Field

Since the magnetic field could not be measured when the coils were installed on the vortex chamber due to the impracticality of placing a magnetometer within the chamber, the measurements of the magnetic flux density were made before installation. The coils were arranged in the orientation in which they would be assembled with the vortex chamber and the magnetic field was measured as a function of Z, r/r_o and the current. The calibration of the flux density as a function of the coil current was made so that the magnitude of the field could be determined by recording the current during a test. The variation of the magnetic flux density B with the coil current was found to be linear over the range of current attainable (4 to 45 amperes) as shown in Fig. 5.35.

The arrangement of the magnetic field coils provided a radial magnetic field which was very nearly constant over the

region of the two-phase vortex as illustrated in Fig. 5.36 and 5.37. In these plots of the normalized flux density it is seen that, over the region of the vortex, the field has a maximum variation of about 10% in both the radial and axial directions.

With the electrodes shorted, the vortex was operated with the maximum magnetic field of about 800 gauss to determine the effect of the field on the flow characteristics. There was no measurable effect on either the pressure or void fraction. This result was as expected due to the low conductivity of the water and the resulting low current induced. The open circuit voltage produced by the vortex operated in the presence of the magnetic field was then determined as a function of the flux density. Fig. 5.38 shows a typical result for a ΔP of 10 psi and P_a = 50 and 15 psig. These results show the open circuit voltage E_o to vary linearly with the magnetic field, which indicates that the difference in the electrical losses for low and high flux densities is negligible or that the losses are proportional to B. If, for a given value of B, E_o is proportional to the tangential water velocity, the results also indicate that there is little difference in the water velocities over the range of P_a investigated at ΔP = 10 psi. Fig. 5.39 illustrates the variation of E_o with B and ΔP at P_a = 50 psig. Here, again, the linear variation of E_o with B at a constant ΔP is evident.

G. General Characteristics of the Vortex

The two-phase annulus resulting from the confined vortex configuration is characterized by the following approximate values:

1.	Mass of water in the two-phase annulus:	0.21 lbm
2.	Through-flow rate of water:	0.1 to 0.4 lbm/min
3.	Air mass flow rate:	1.3 to 7.3 lbm/min
4.	Average void fraction	0.53
5.	Outer radius of two-phase annulus:	2.5 in ($r/r_o = 1$)
6.	Inner radius of two-phase annulus:	1.5 in ($r/r_o = 0.6$)
7.	Height of annulus:	1.0 in
8.	Temperature of feed water	54°F
9.	Temperature of plenum air	63°F
10.	Temperature of two-phase mixture	55°F
11.	Water retention time $(m/\dot{m})_L$	0.5 to 2.0 min

H. Accuracy of the Measurements

The gauge used to measure the pressures could be read accurately to ± 0.05 psi. The critical factor in making the pressure measurements was the setting and control of the exhaust pressure, since this back pressure acted as a bias for both the static and total pressures. Control of the back pressure was sometimes difficult due to the fluctuations of

of the air supply pressure which varied as much as ±8 psi with a frequency of about 2 minutes (the duty cycle of the compressors). Once the desired balance between plenum air pressure P_a and the back pressure P_E was achieved, it could be maintained by adjusting the air supply valve to maintain P_a at the desired level. Although continuous manual control was applied to maintain the desired settings of P_a and P_E, it was difficult to restrict the fluctuations of P_E to a range less than ±0.10 psi.

At the higher values of ΔP the turbulence of the vortex flow often caused fluctuations in P_E as high as ±0.10 psi at a frequency of 4 or 5 cycles per second. Although an effort was made to read the mean of these fluctuations, they were sufficiently irregular that a potential error of the order of magnitude of the fluctuations must be assumed. The combination of the errors restricts the precision of the pressure measurement to about ±0.25 psi which corresponds to about 6% error at the low pressures and 1.0% at the high pressures. In repeating measurements from time to time it was found that the agreement was usually better than implied by these values; however, an occasional measurement was observed to exhibit a variation of the magnitude indicated.

J. Probe Effects on the Vortex Flow

The insertion of a probe into a confined vortex creates a greater disturbance than it would for flow in a channel

since the disturbance may propagate back on itself as was observed with the void fraction probe in this investigation. In addition, the drag which a probe exerts on the flow has been found to cause significant changes in the mass flow rates and pressure profiles in a vortex. In the investigations of an air vortex, Savino and Keshock[23] estimate that the presence of a probe in the high velocity region of the vortex resulted in a maximum shift of the static pressure of about 16%. Roschke[31] investigated the effect of probe insertion into a single-phase water vortex by placing wires of varying diameters across a diameter of the vortex. For a wire diameter of 1.0% of the vortex diameter it was found necessary to increase the mass flow of the water by about 10% to maintain a fixed pressure at the outer diameter. It was also noted that the insertion of a probe resulted in a significant rise in the static pressure at the center of the vortex (measured at the end wall) and that the insertion of a second probe did not produce a further change of comparable magnitude.

In the investigation of a confined gas vortex, Pivirotto[33] found that a probe with a diameter of $0.025r_o$ placed across a diameter of the vortex resulted in a 20% decrease in the maximum Mach number at constant plenum pressure. He also found that the pressure drop across the vortex decreased substantially with increasing probe diameter.

These considerations indicate that, although the pressures may be measured with reasonable precision, the results

obtained by the use of probes may deviate significantly from free stream values. In the two-phase vortex the effect of the probe insertion is expected to be even greater due to the additional consideration of the disruption of the phase volume distributions.

TABLE 5.1

AIR MASS FLOW RATES

P_a (psig)	ΔP (psi)	$\dot{m}$ (calculated) (lbm/min)	$\dot{m}$ (measured) (lbm/min)	Deviation (%)
5	2	1.42	1.32	7.0
5	3	1.65	1.57	4.8
5	3.5	1.76	1.70	3.4
10	2	1.54	1.35	12.3
10	4	2.12	2.00	5.7
10	6	2.45	2.35	4.1
10	8	2.68	2.52	6.0
15	2	1.68	1.58	6.0
15	4	2.24	2.10	6.2
15	6	2.66	2.58	3.0
15	8	2.98	2.77	7.0
15	10	3.30	3.15	4.5
15	12	3.44	3.34	2.9
20	2	1.87	1.75	6.4
20	4	2.44	2.30	5.7
20	6	2.95	2.81	4.7
20	8	3.29	3.15	4.2
20	10	3.57	3.40	4.8
20	12	3.80	3.65	6.6
20	14	4.02	3.96	1.5
20	16	4.15	3.97	4.3
25	2	1.83	1.72	6.0
25	4	2.64	2.50	5.3
25	6	3.17	3.00	5.4
25	8	3.58	3.42	4.5
25	10	3.92	3.77	3.9
25	12	4.25	4.00	5.9
25	14	4.38	4.38	0.0
25	16	4.55	4.45	2.2
25	18	4.72	4.67	1.1
30	2	2.03	1.87	7.9
30	4	2.80	2.53	9.6
30	6	3.30	3.07	7.0
30	8	3.77	3.62	4.0
30	10	4.10	4.04	1.5
30	12	4.38	4.38	0.0
30	14	4.67	4.48	4.1

TABLE 5.1 (Continued)

P_a (psig)	ΔP (psi)	$\dot{m}$ (calculated) (lbm/min)	$\dot{m}$ (measured) (lbm/min)	Deviation (%)
35	2	2.07	1.90	8.2
35	4	2.83	2.70	4.6
35	6	3.46	3.22	6.9
35	8	3.90	3.75	3.8
35	10	4.30	4.22	1.9
35	12	4.67	4.55	2.6
40	2	2.14	1.95	8.9
40	4	2.98	3.00	-0.7
40	6	3.59	3.40	5.3
40	8	4.08	3.95	3.2
40	10	4.56	4.52	0.9
45	2	2.19	2.00	8.7
45	4	3.19	3.00	6.0
45	6	3.79	3.57	5.8
45	8	4.29	4.24	1.2
50	2	232	2.17	6.5
50	4	3.32	3.12	6.0
50	6	4.10	3.75	8.5

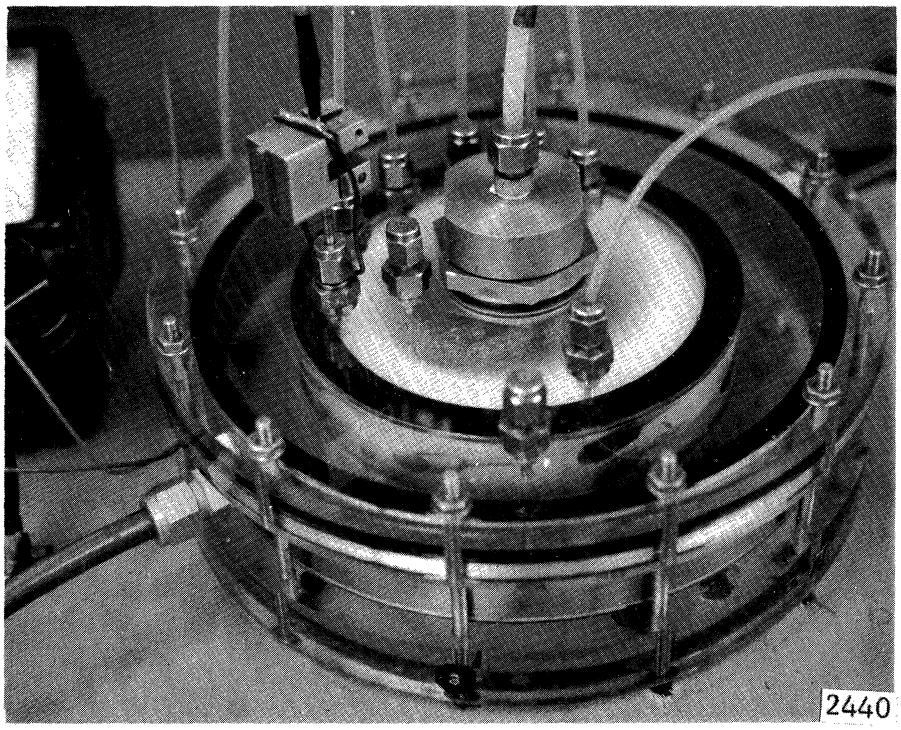

Fig. 5.1 - Typical Appearance of the Two-Phase Vortex.

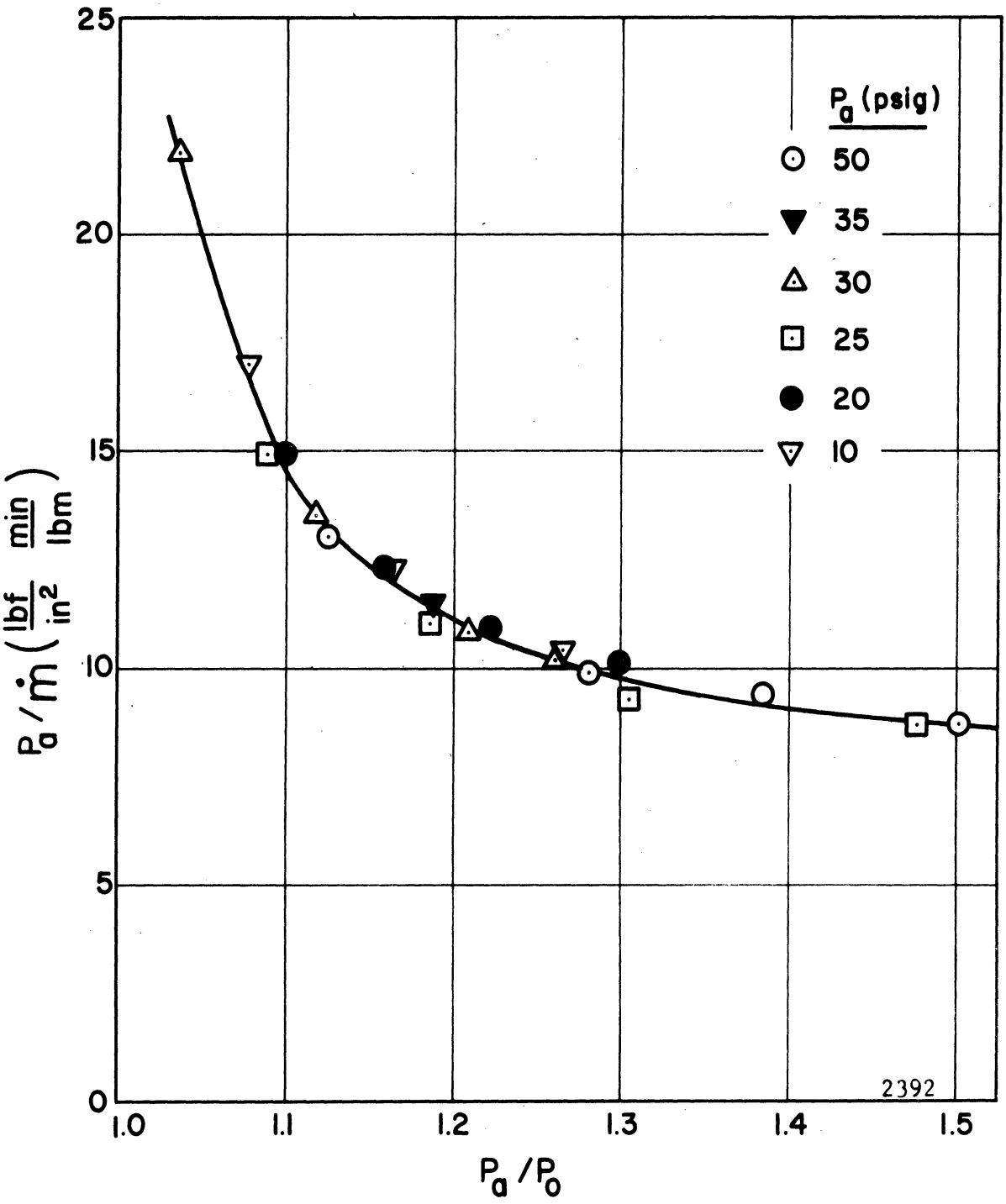

Fig. 5.2 - Air Mass Flow Rate as a Function of the Pressure Ratio P_a/P_o.

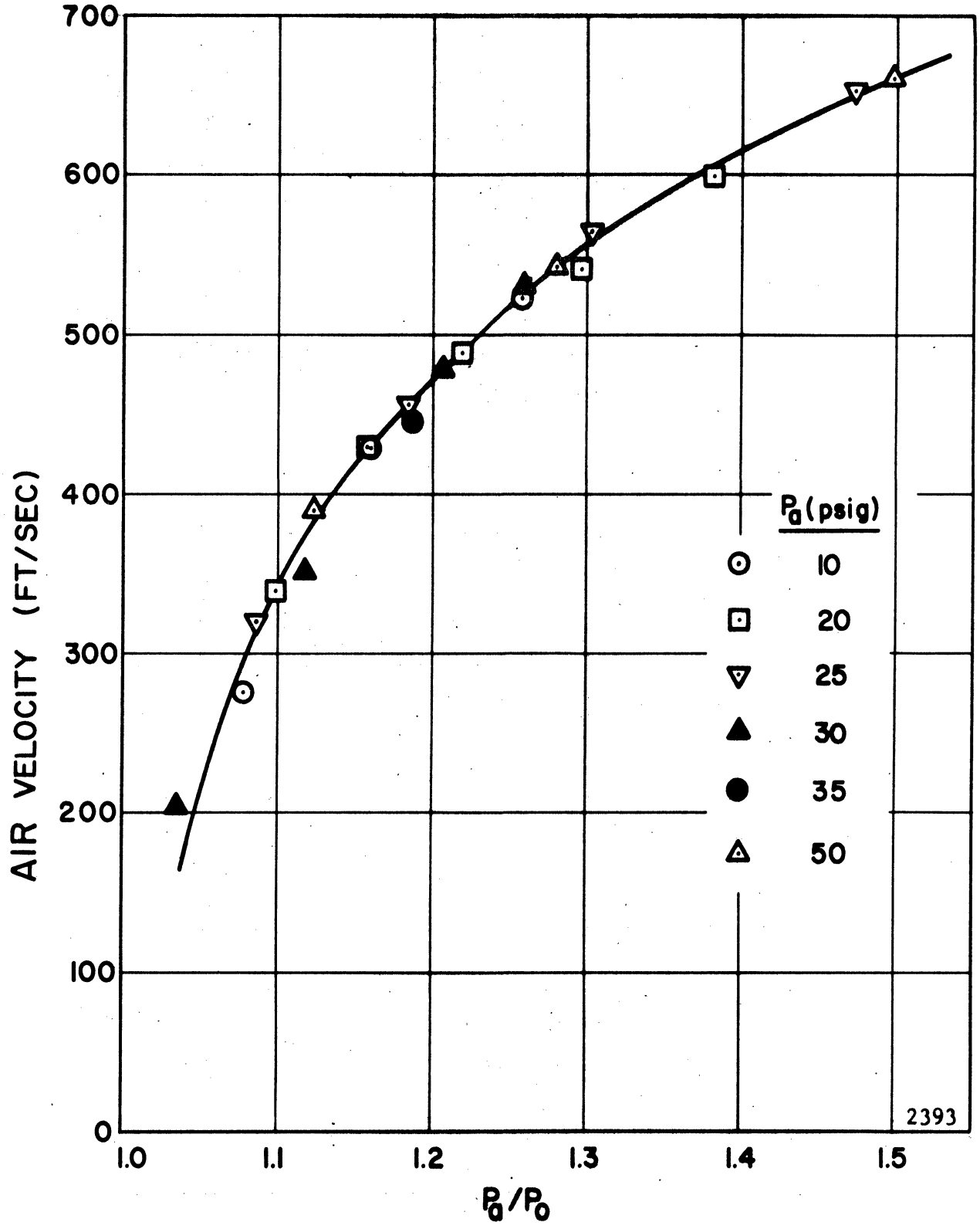

Fig. 5.3 - Air-Jet Velocity at the Nozzle Exits as a Function of the Pressure Ratio P_a/P_o.

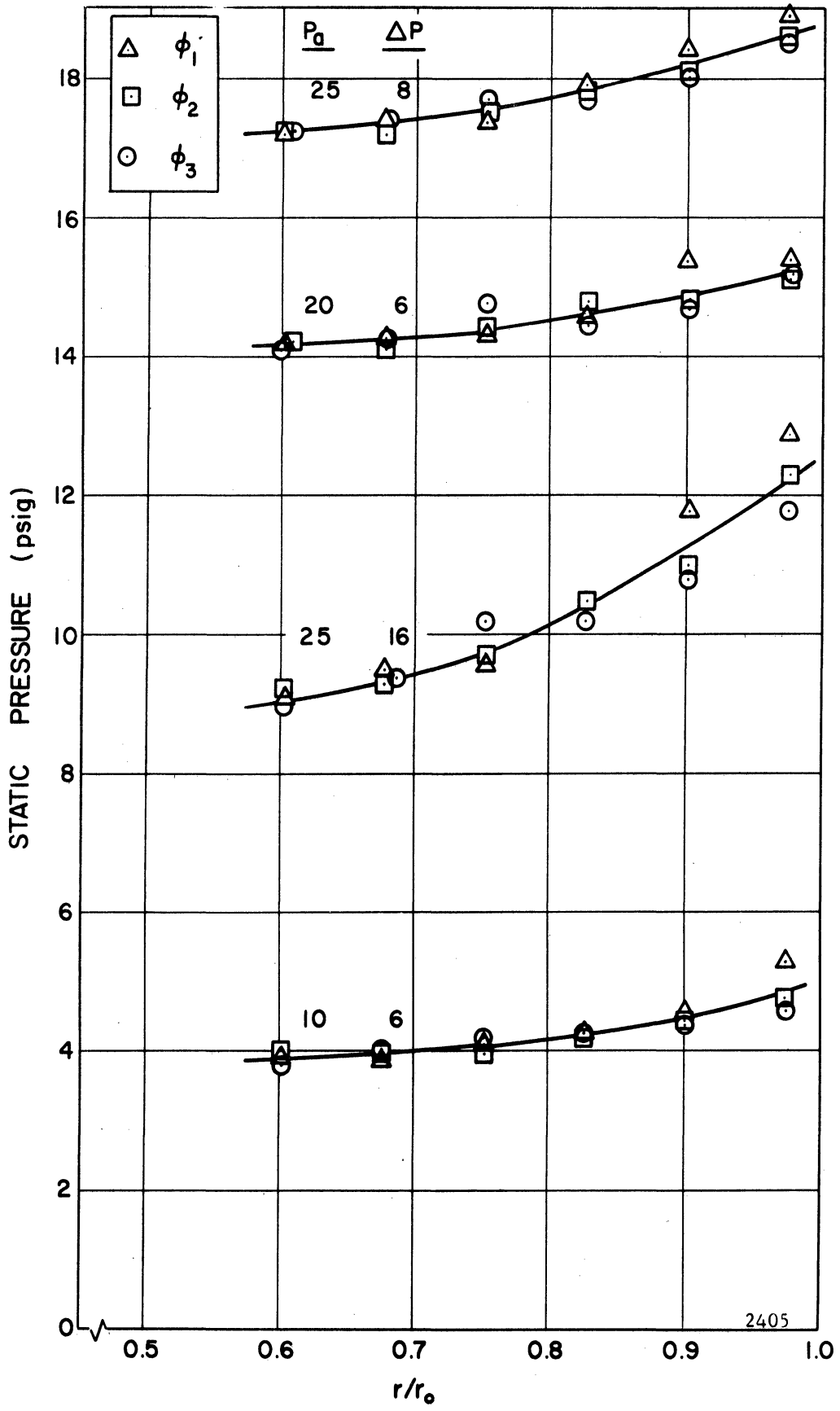

Fig. 5.4 - Radial Distribution of Static Pressure as a Function of Ø and ΔP. P_a = 25 psig, Test Series No. 1.

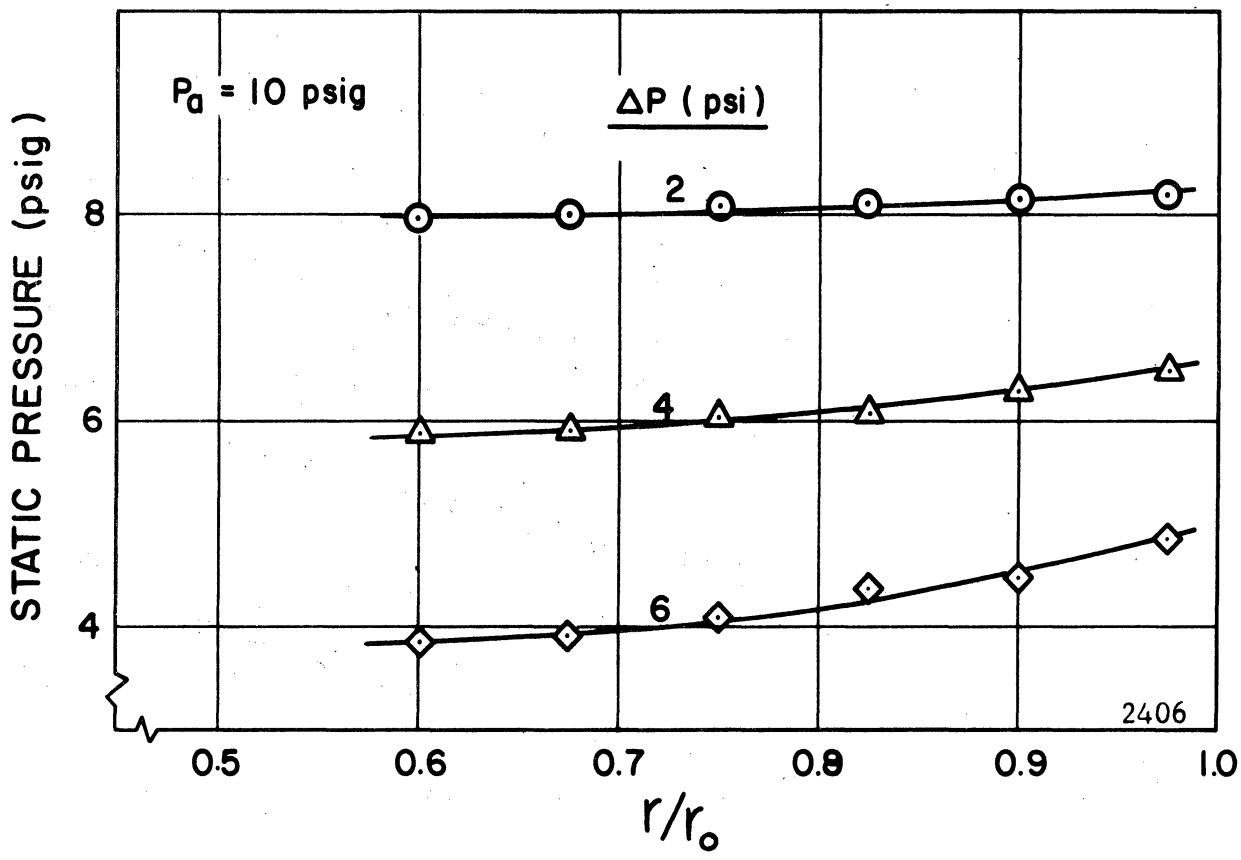

Fig. 5.5 - Radial Distribution of Static Pressure as a Function of ΔP (Averaged over $\emptyset$). P_a = 10 psig, Test Series No. 1.

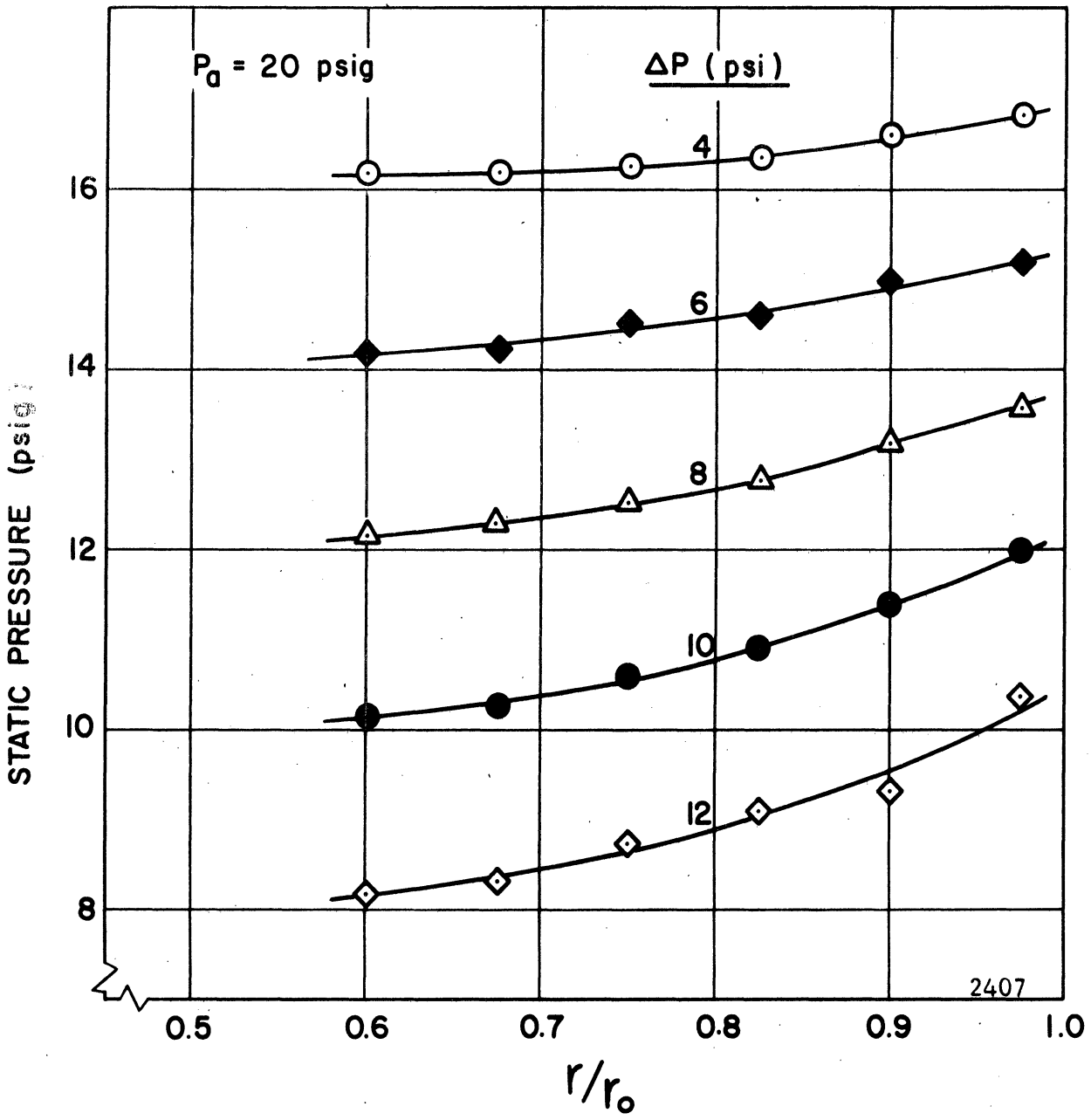

Fig. 5.6 - Radial Distribution of Static Pressure as a Function of ΔP (Averaged over Ø). P_a = 20 psig, Test Series No. 1.

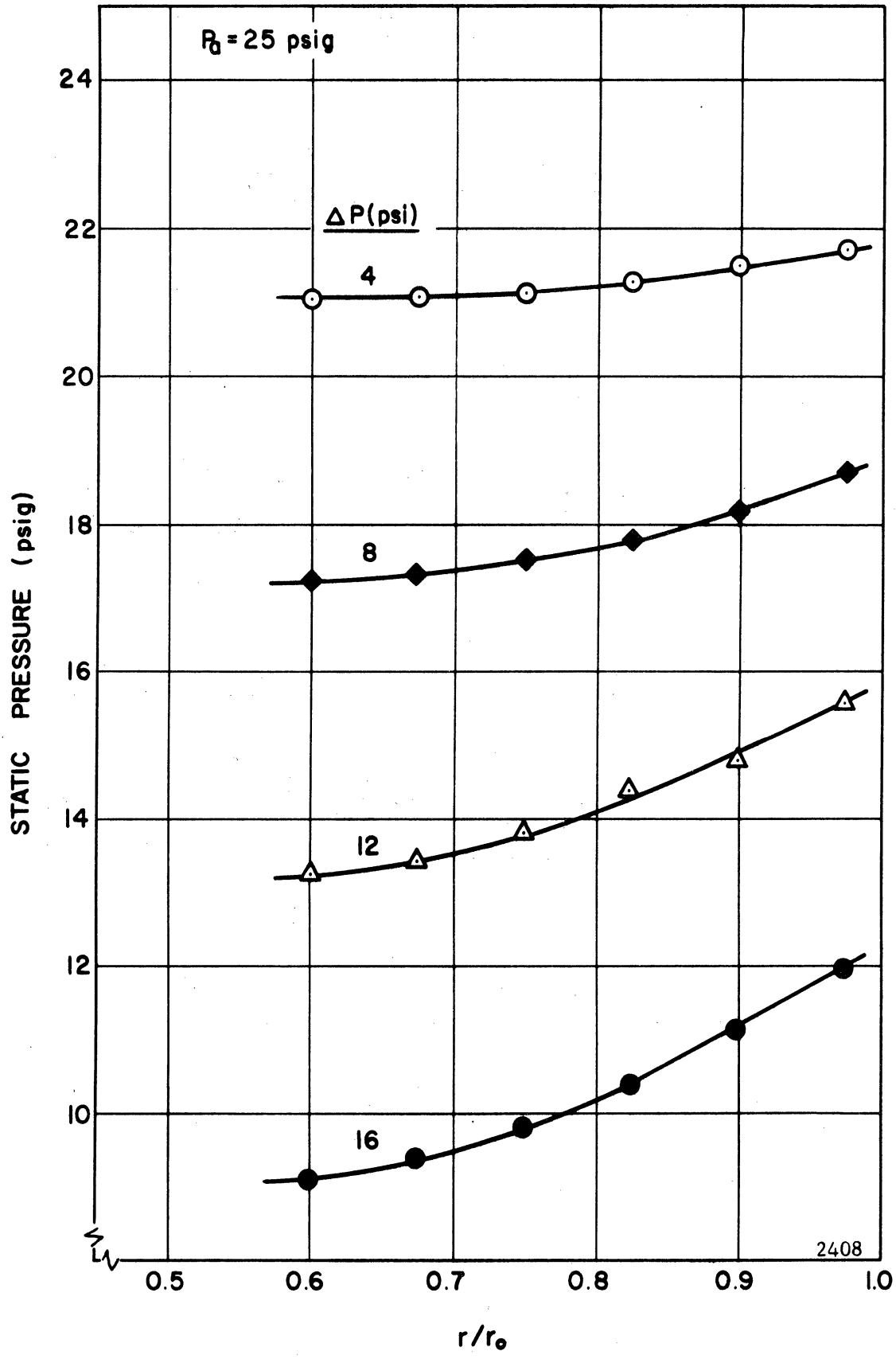

Fig. 5.7 - Radial Distribution of Static Pressure as a Function of ΔP (Averaged over Ø). P_a = 25 psig, Test Series No. 1.

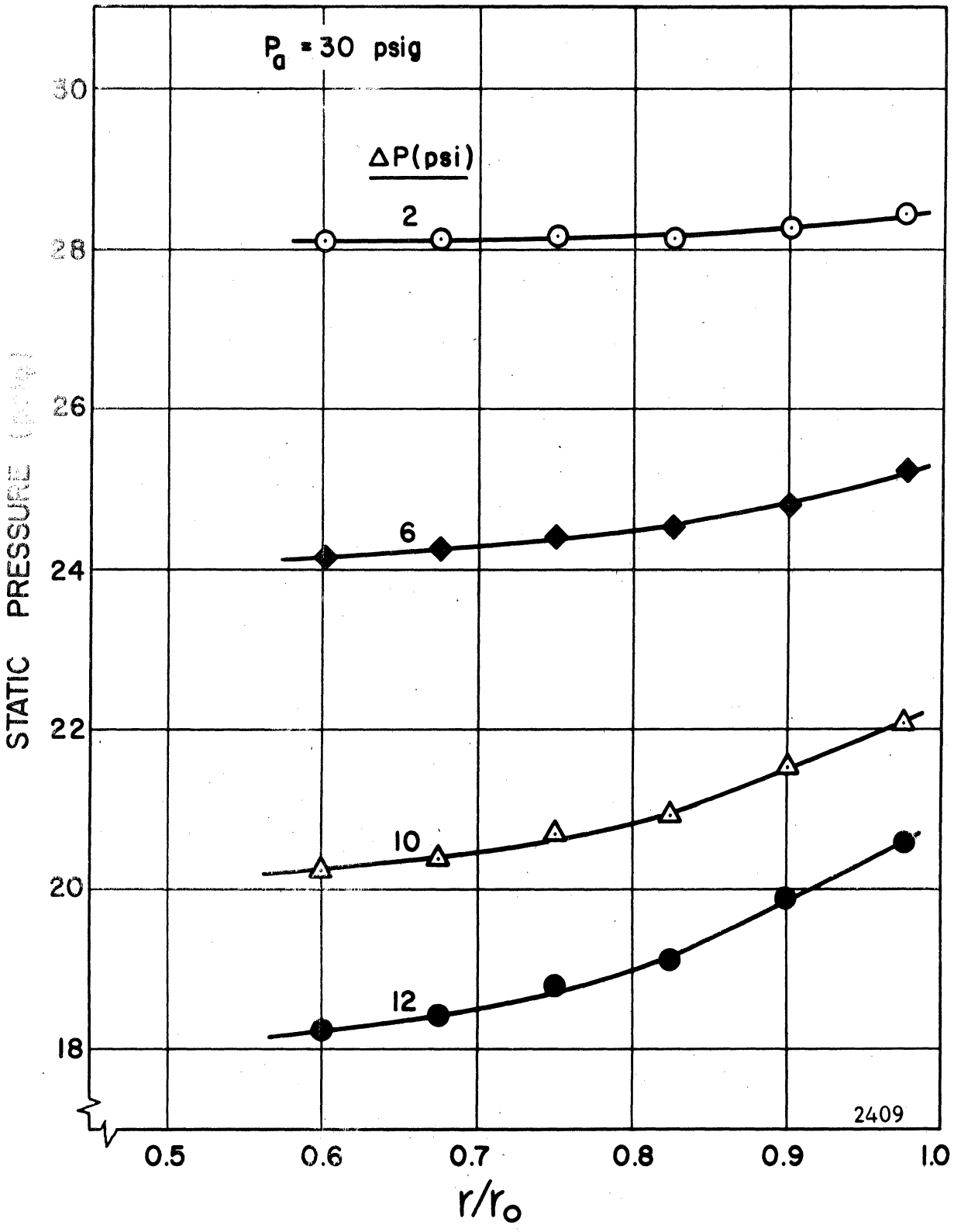

Fig. 5.8 - Radial Distribution of Static Pressure as a Function of ΔP (Averaged over Ø). P_a = 30 psig, Test Series No. 1.

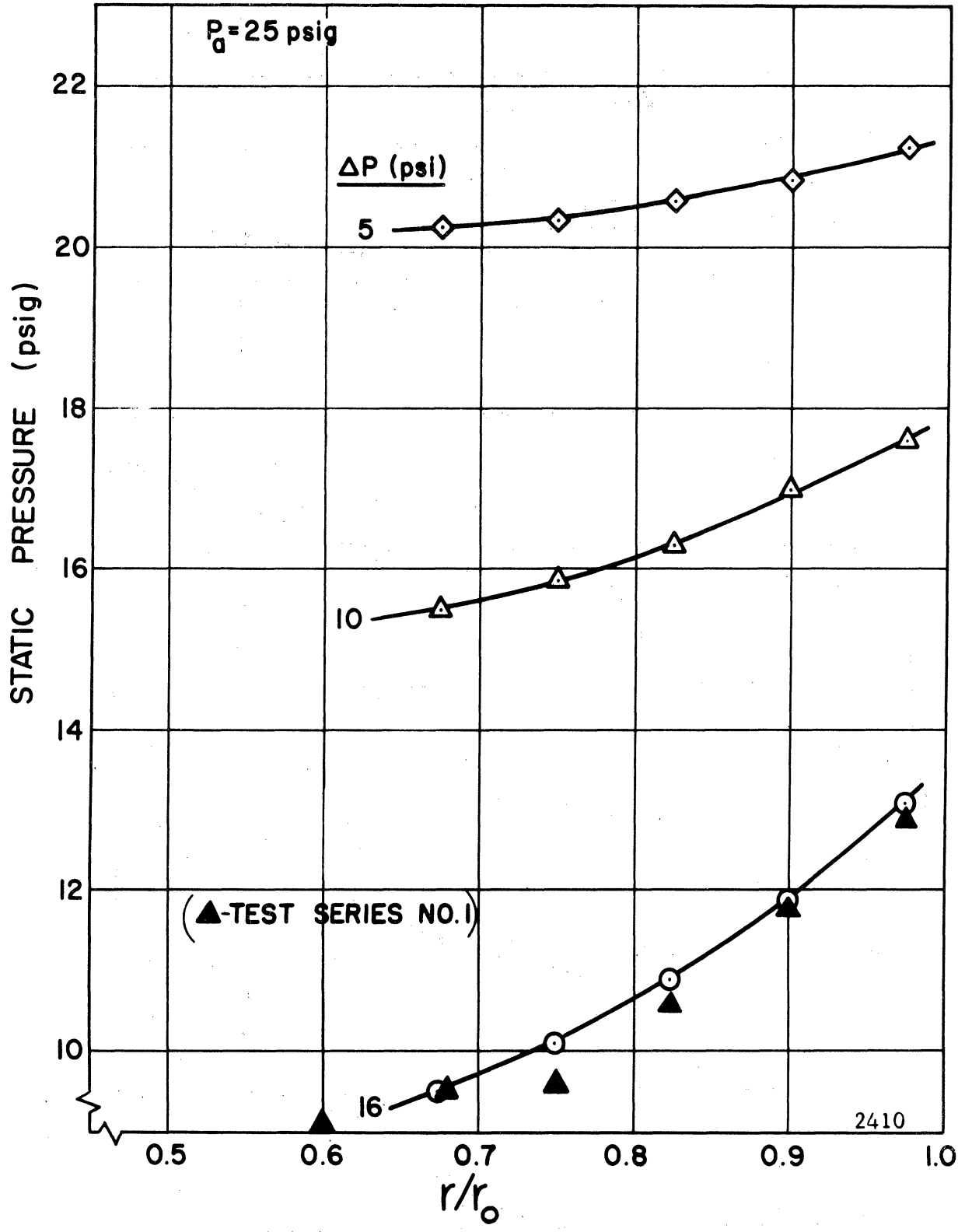

Fig. 5.9 - Radial Distribution of Static Pressure as a Function of ΔP. P_a = 25 psig, Test Series No. 2.

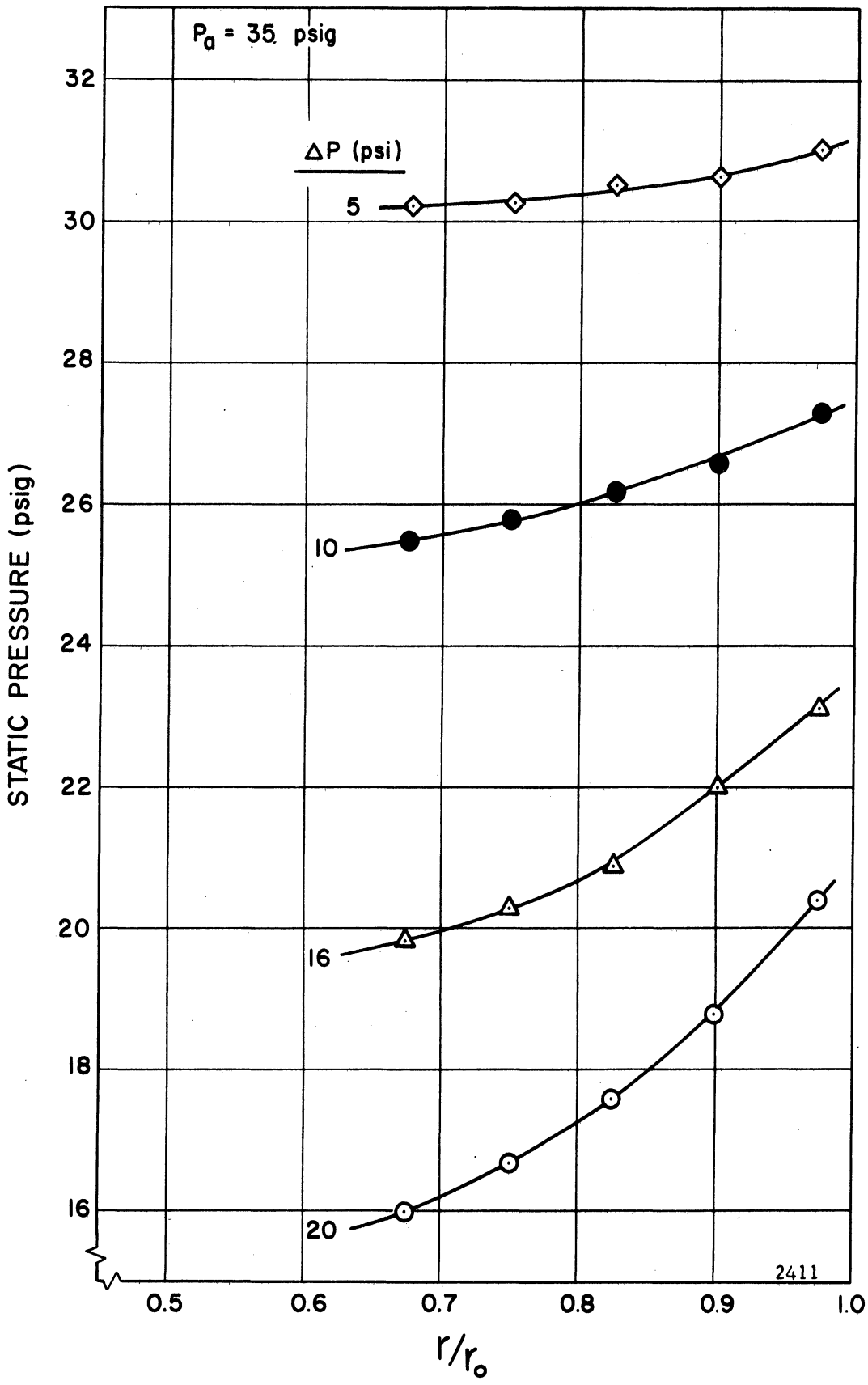

Fig. 5.10 - Radial Distribution of Static Pressure as a Function of ΔP. P_a = 35 psig, Test Series No. 2.

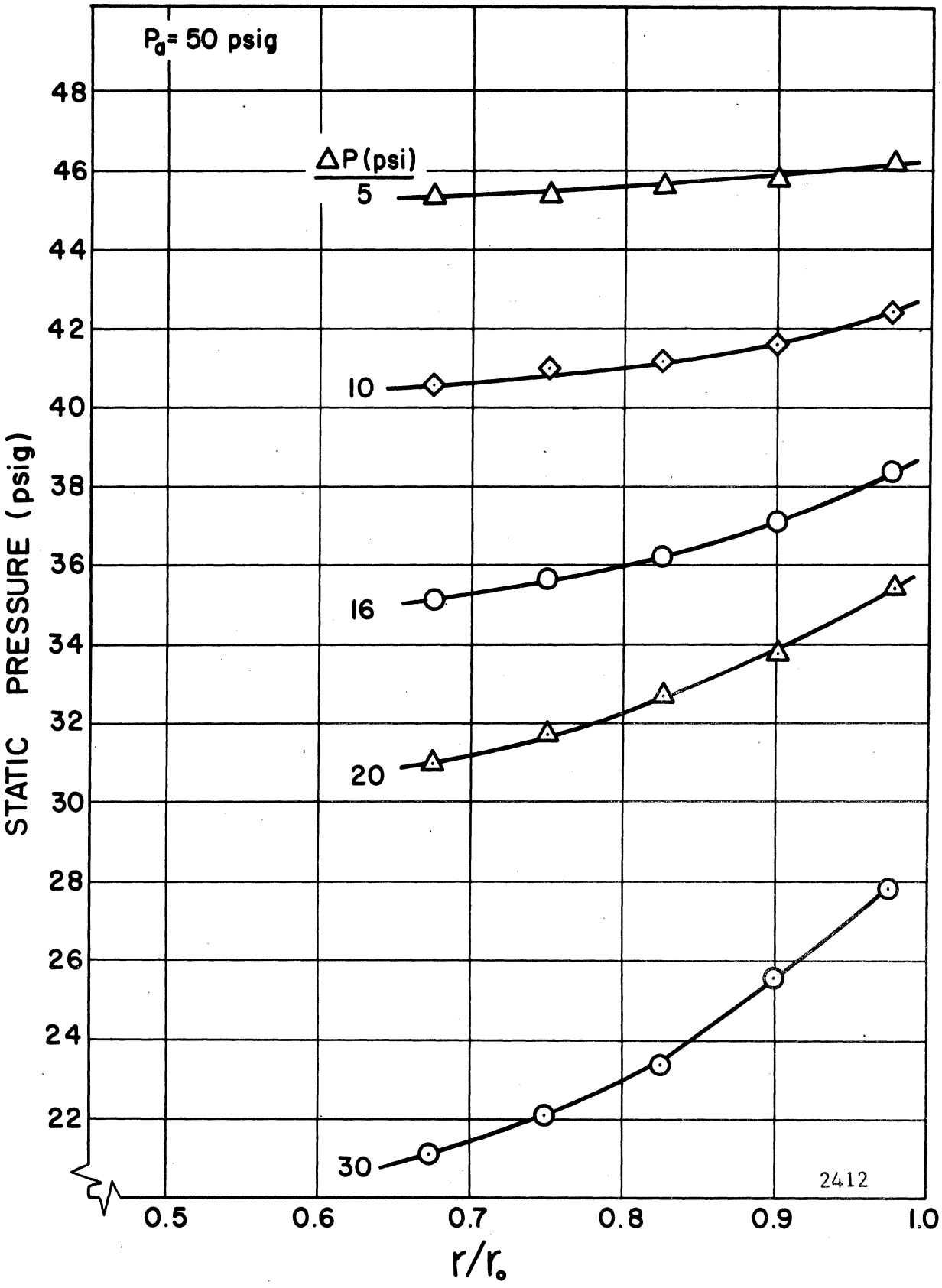

Fig. 5.11 - Radial Distribution of Static Pressure as a Function of ΔP. P_a = 50 psig, Test Series No. 2.

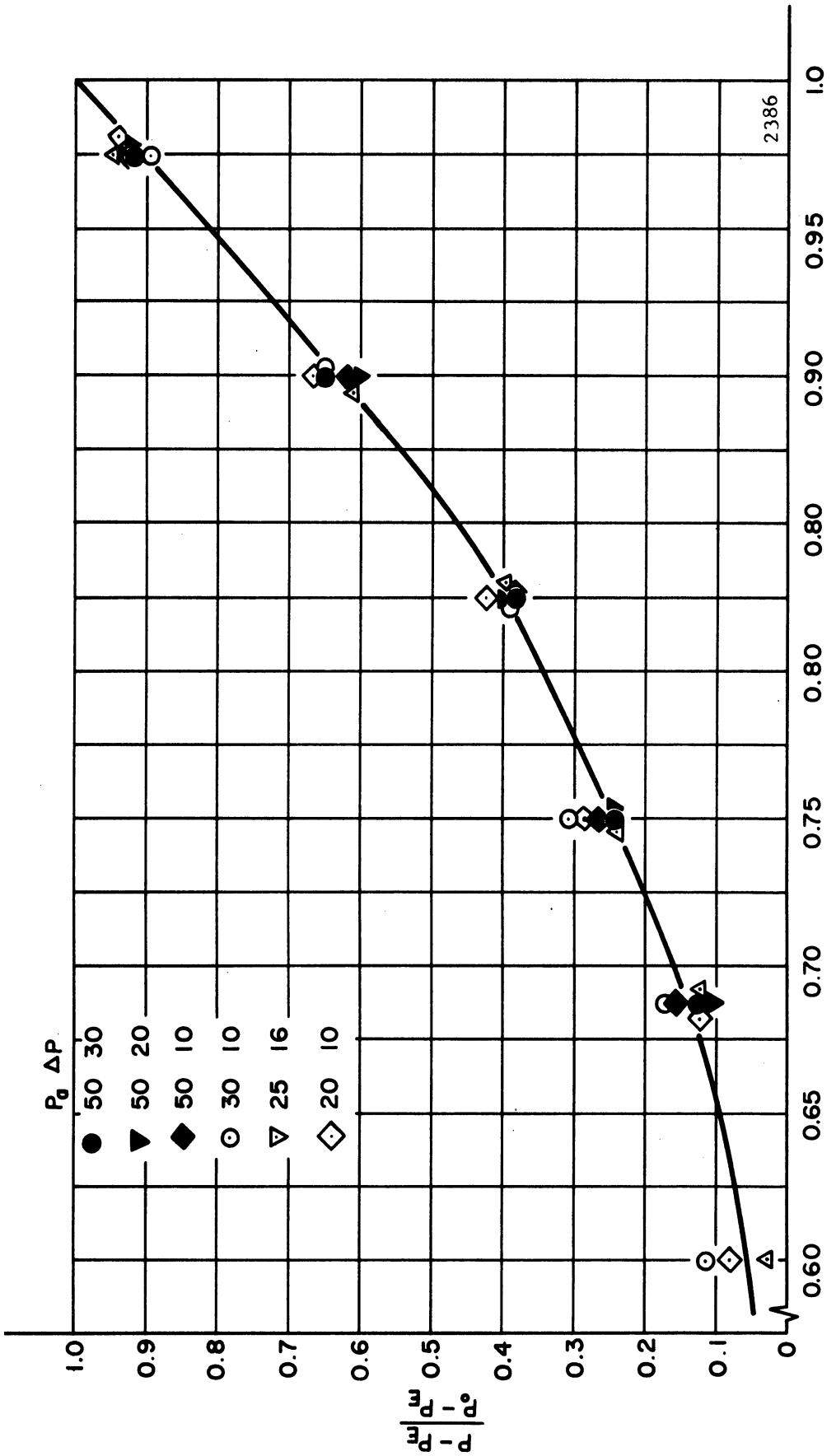

Fig. 5.12 - Radial Distribution of the Pressure Difference Ratio.

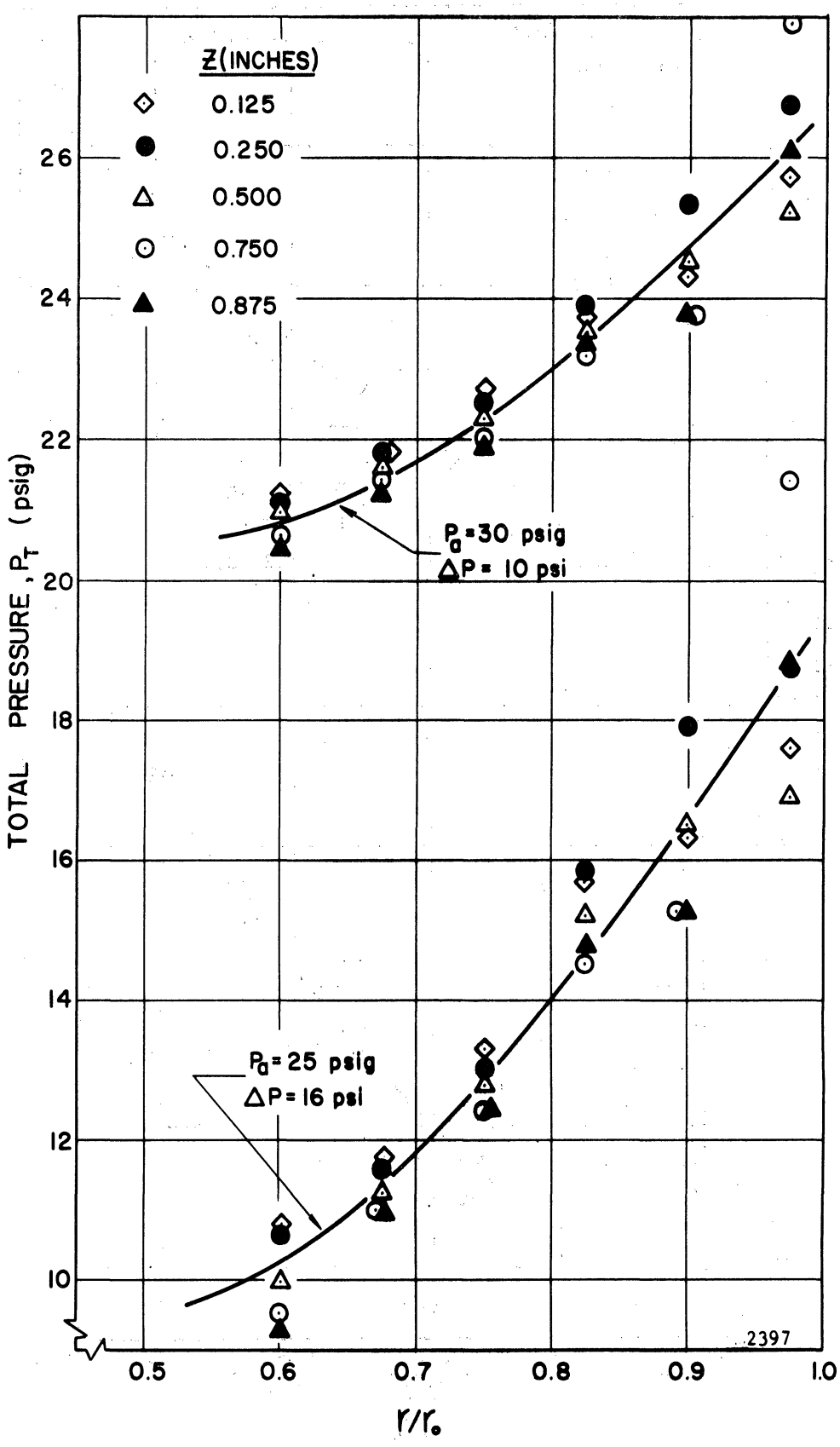

Fig. 5.13 - Radial Distributions of the Total Pressure as a Function of Axial Position for Representative Values of P_a and ΔP. Test Series No. 1 at $\emptyset_1$

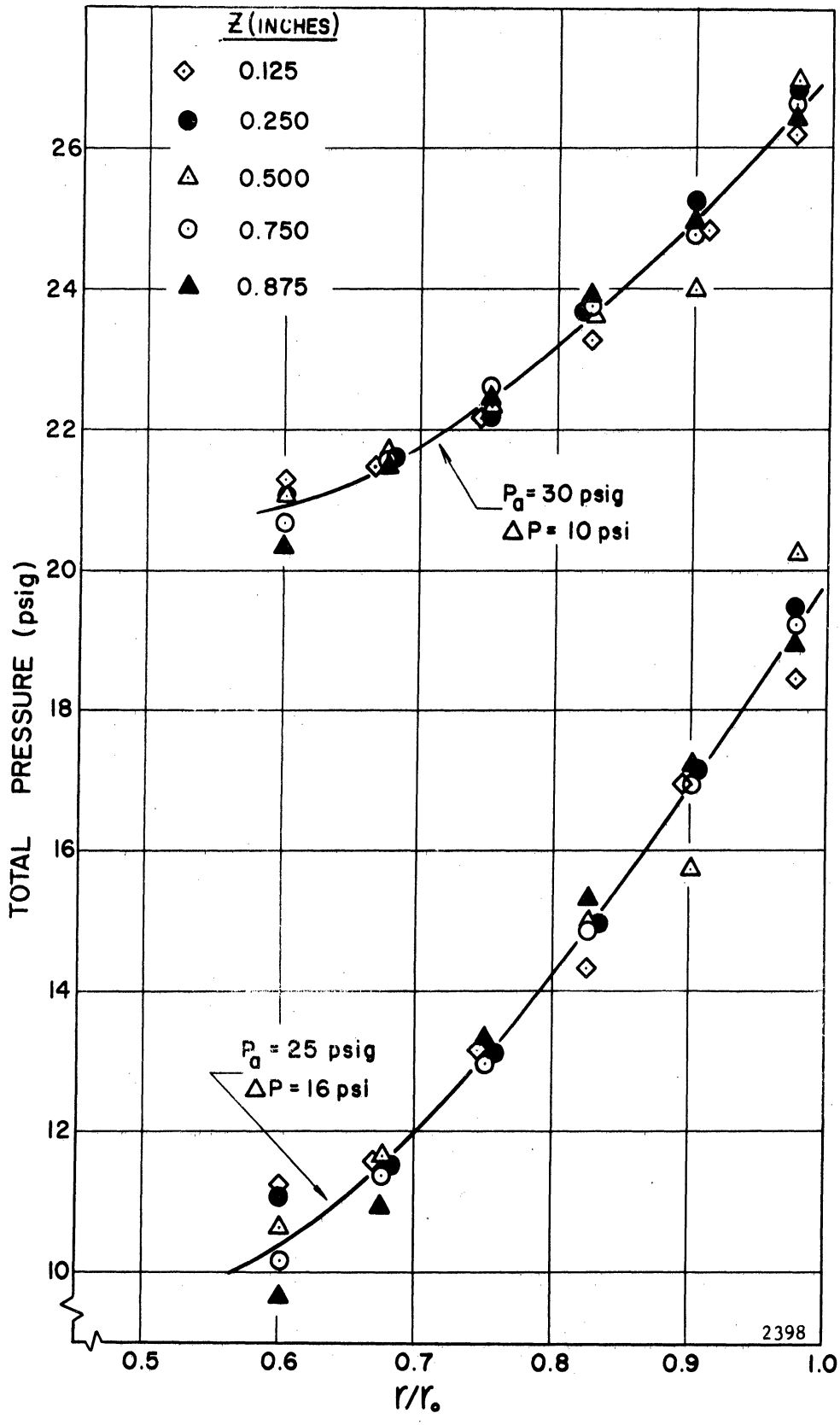

Fig. 5.14 - Radial Distributions of the Total Pressure as a Function of Axial Position for Representative Values of P_a and ΔP. Test Series No. 1 at ϕ_2.

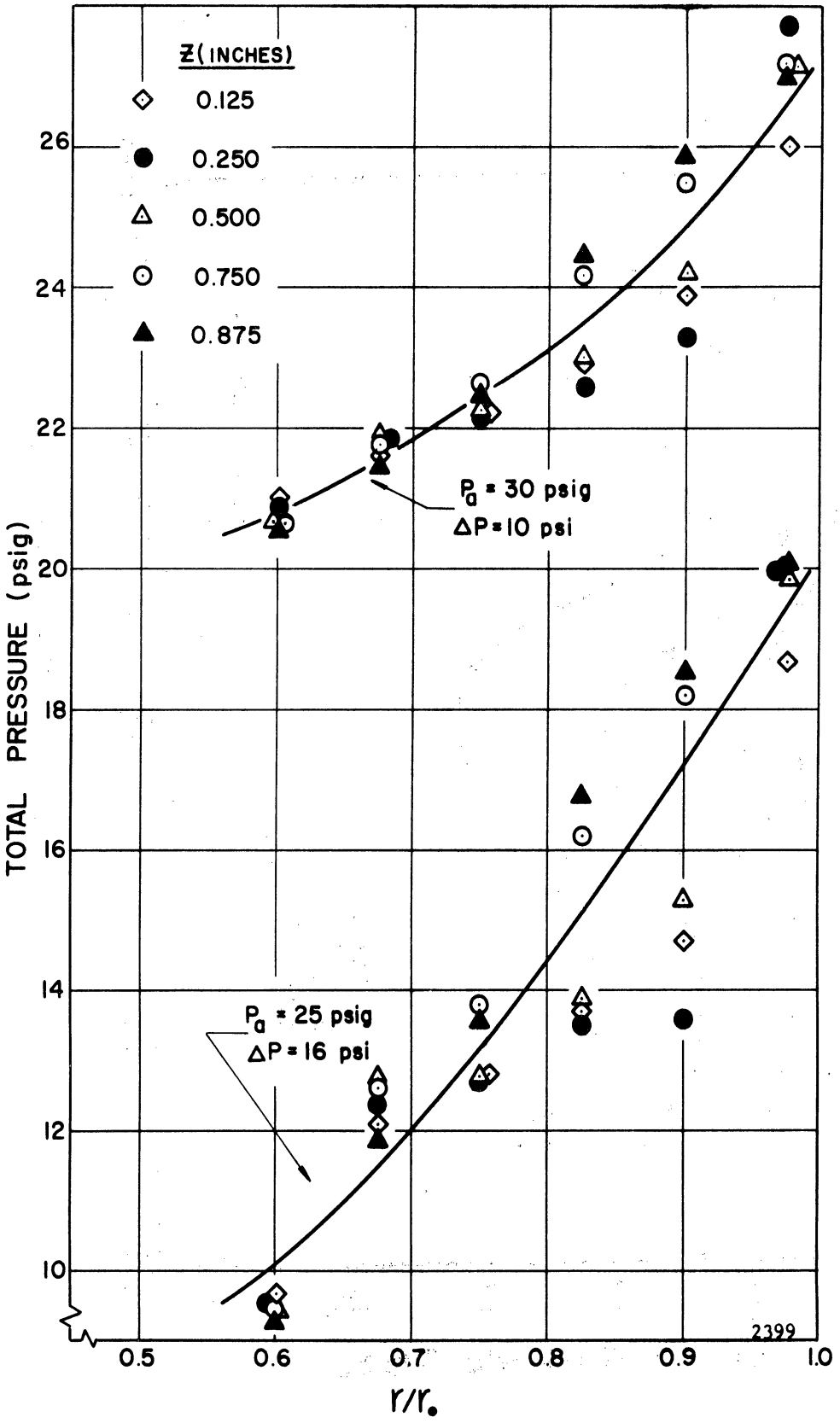

Fig. 5.15 - Radial Distributions of the Total Pressure as a Function of Axial Position for Representative Values of P_a and ΔP. Test Series No. 1 at $\emptyset_3$.

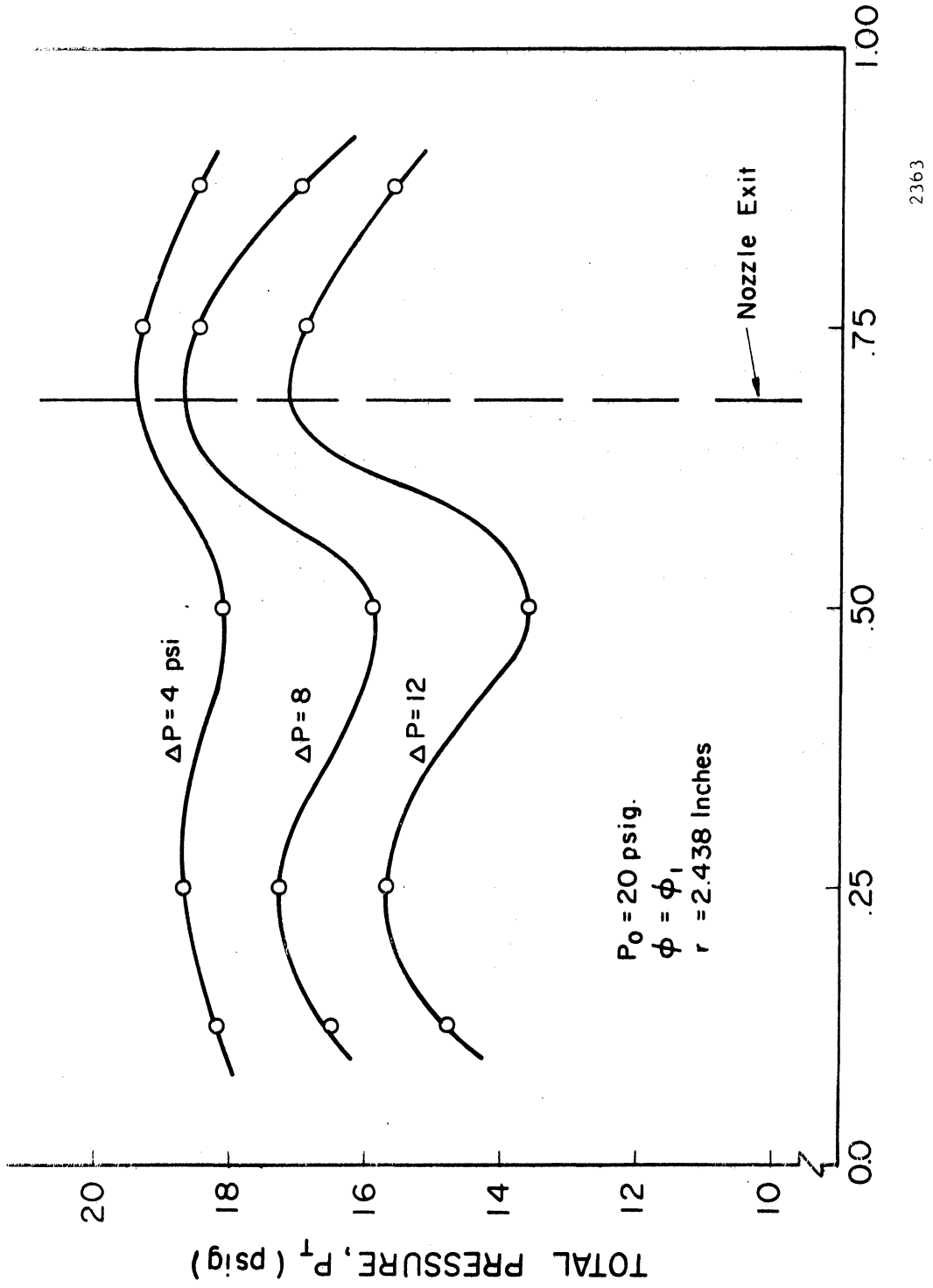

Fig. 5.16 - Axial Distribution of Total Pressure as a Function of ΔP. Test Series No. 1.

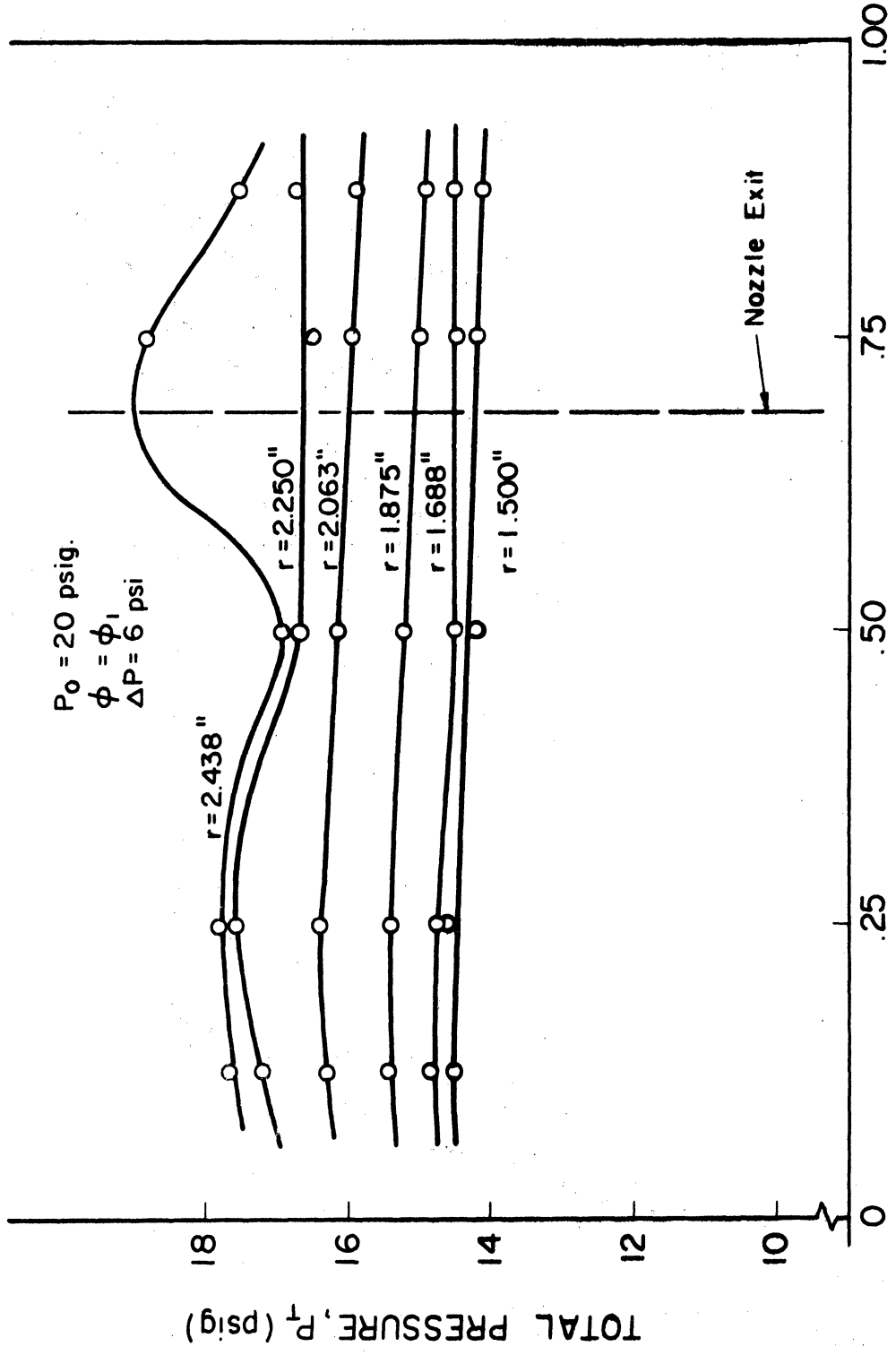

Fig. 5.17 - Axial Distribution of Total Pressure as a Function of Radius. Test Series No. 1.

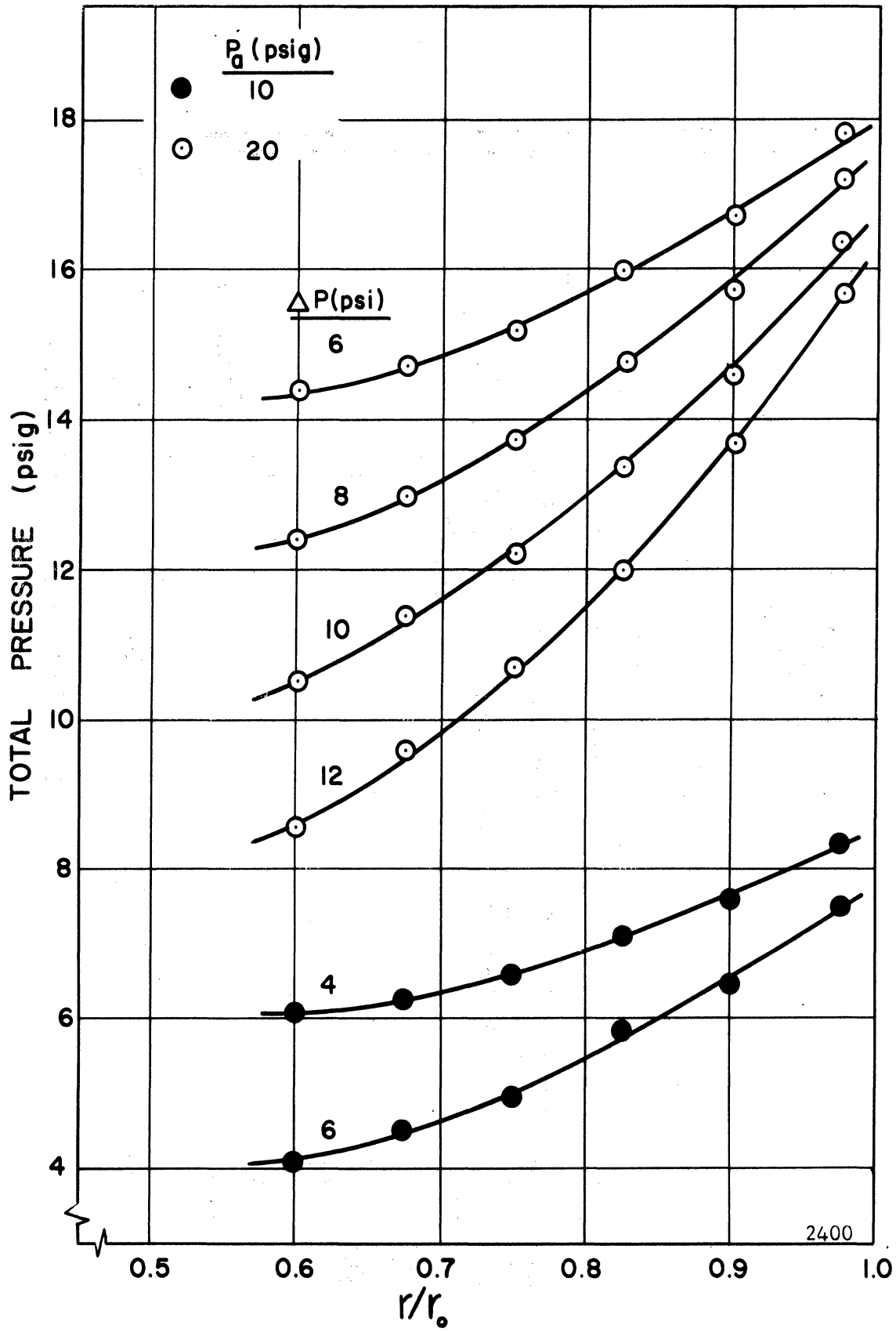

Fig. 5.18 - Radial Distributions of Total Pressure Averaged over Z and Ø. Test Series No. 1.

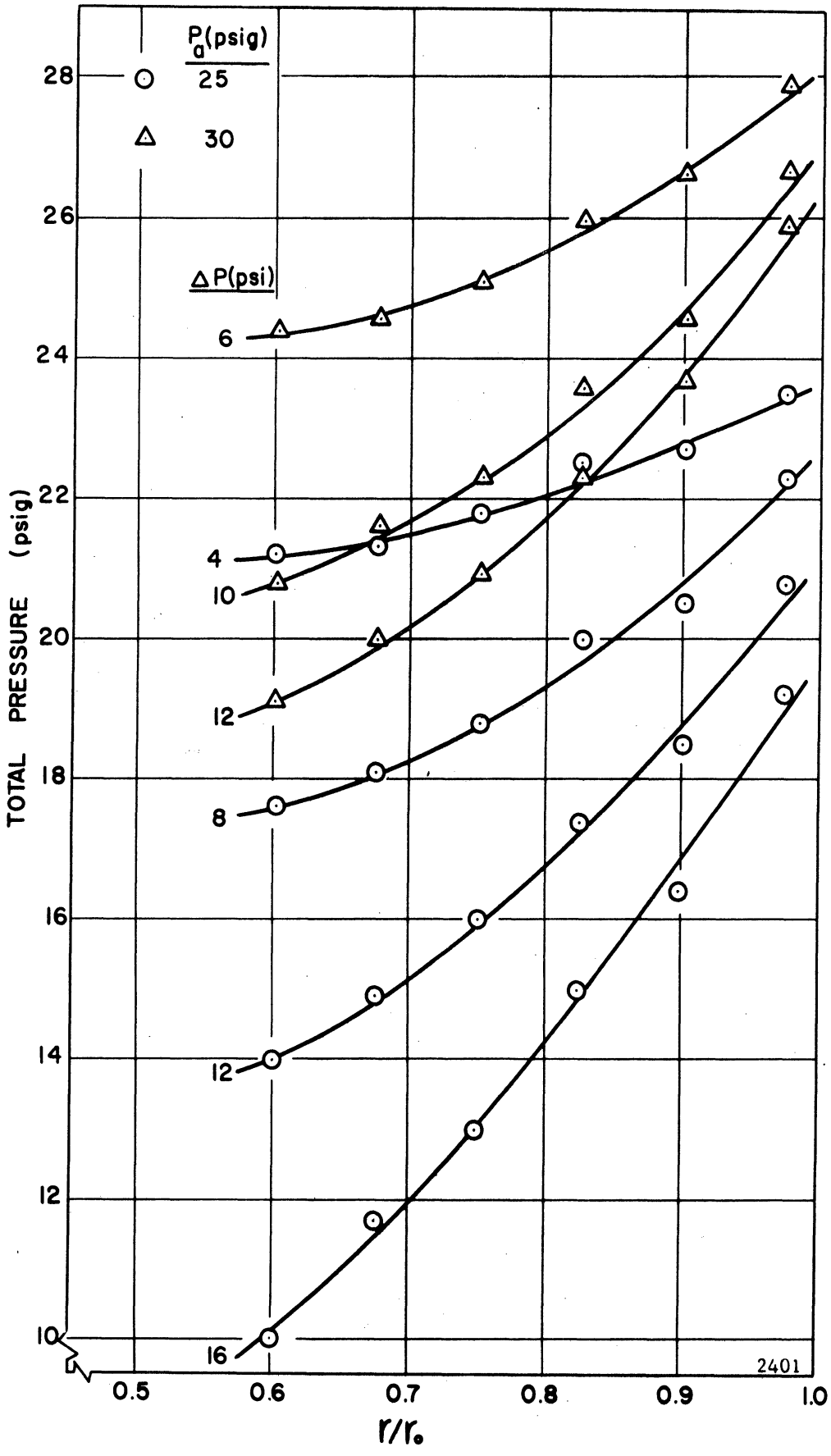

Fig. 5.19 - Radial Distributions of Total Pressure Averaged over Z and Ø. Test Series No. 1.

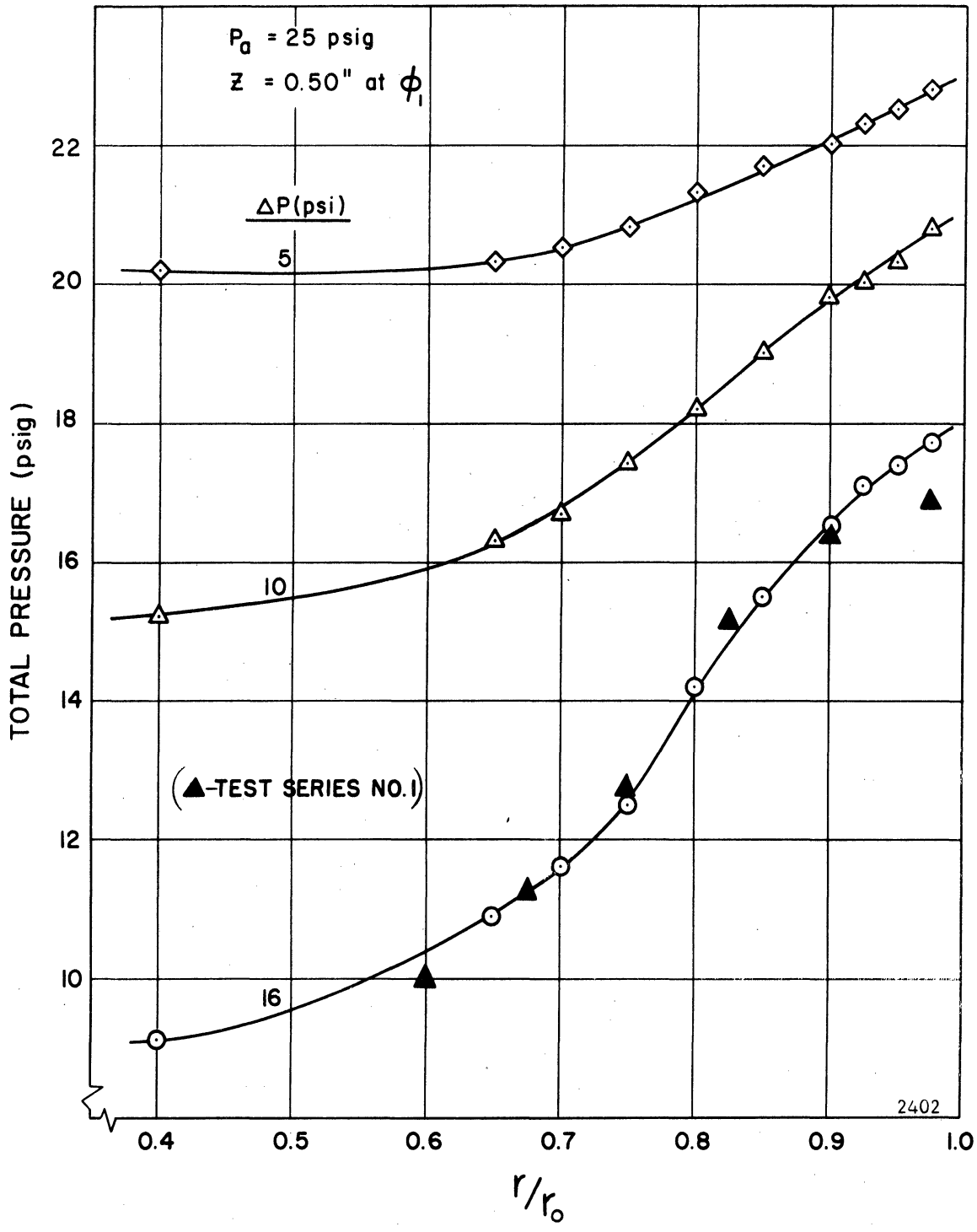

Fig. 5.20 - Radial Distributions of Total Pressure as a Function of ΔP. P_a = 25 psig, Test Series No. 2.

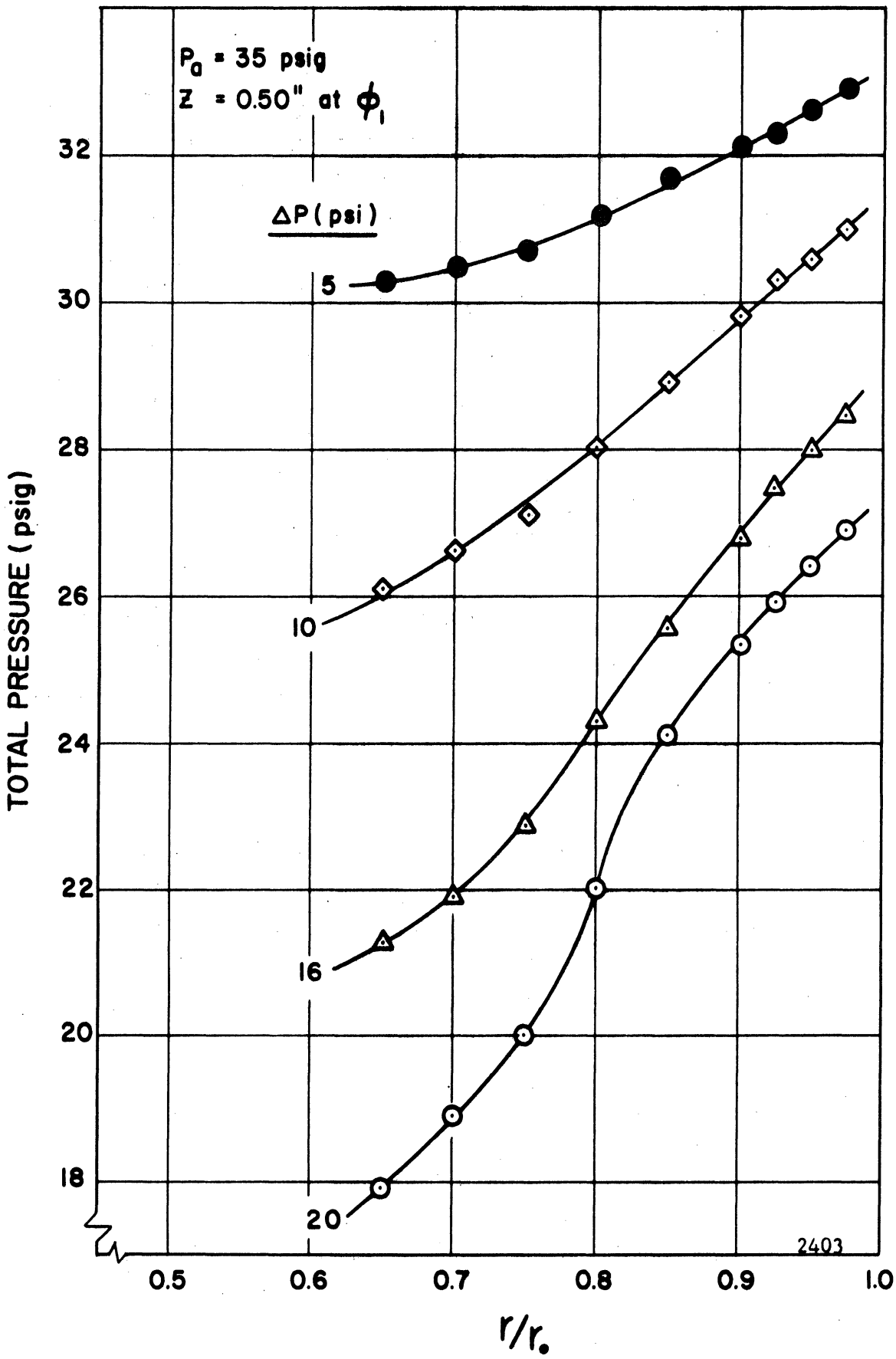

Fig. 5.21. - Radial Distributions of Total Pressure as a Function of ΔP. P_a = 35 psig, Test Series No. 2.

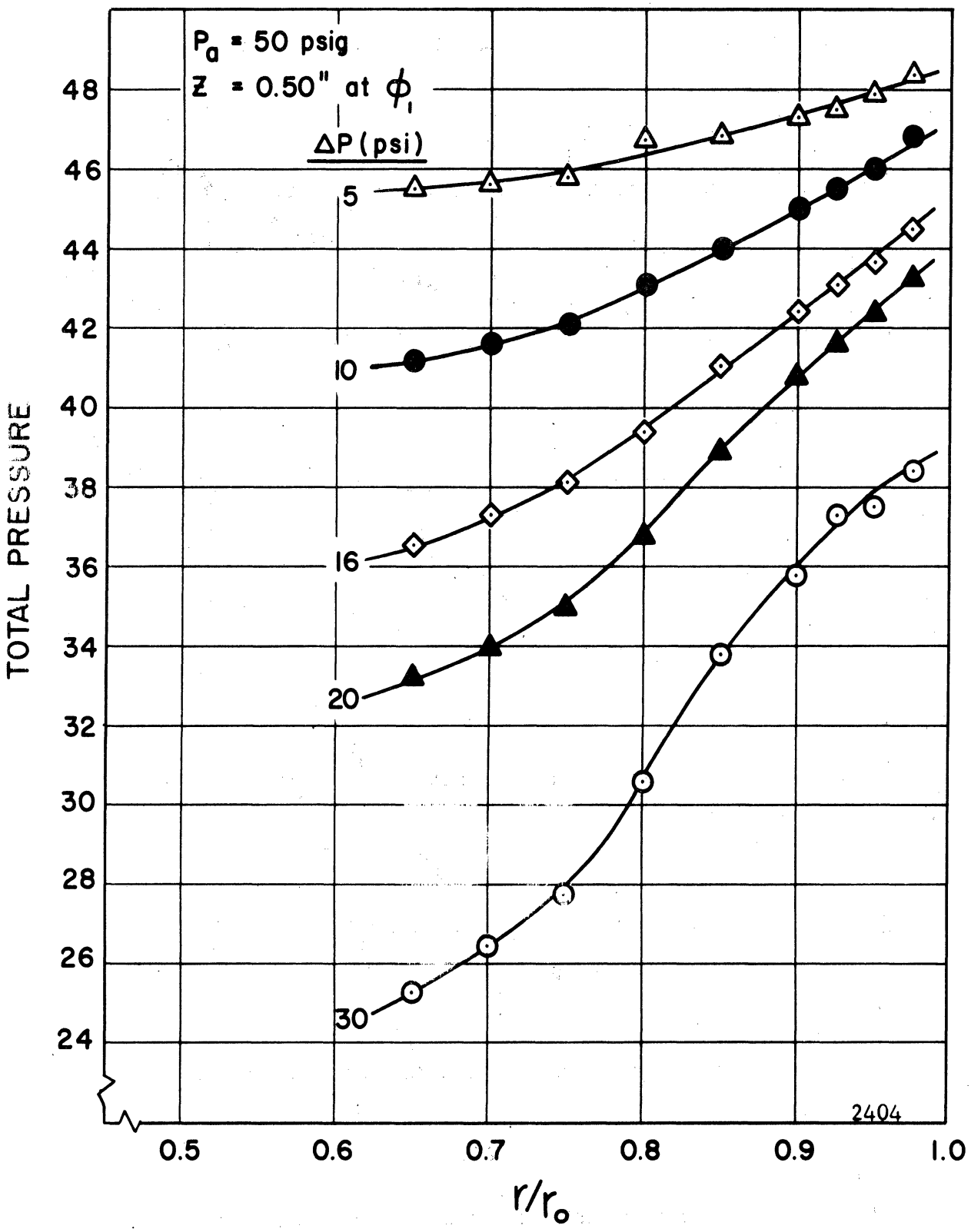

Fig. 5.22 - Radial Distributions of Total Pressure as a Function of ΔP. P_a = 50 psig, Test Series No. 2.

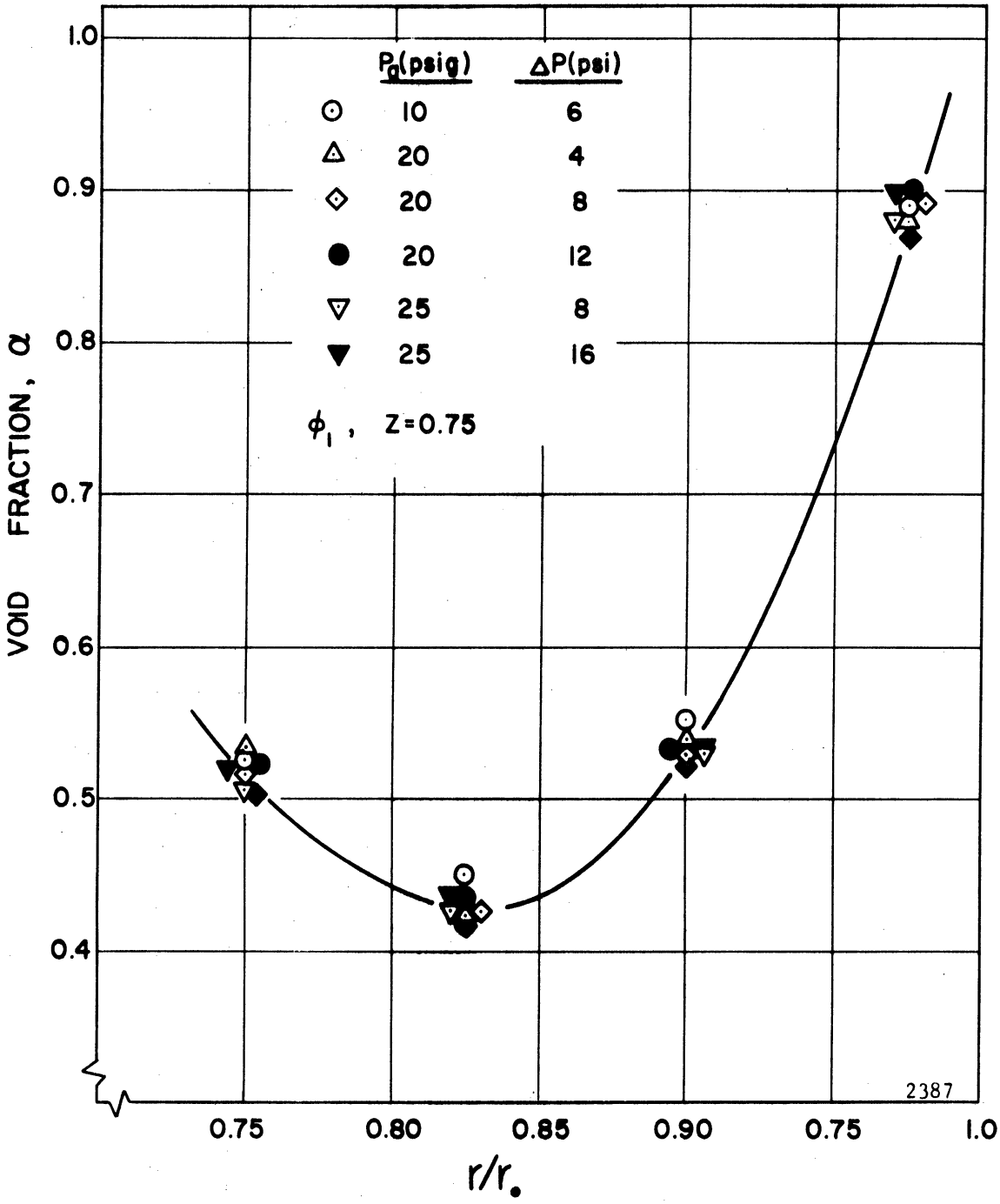

Fig. 5.23 - Radial Distribution of Void Fraction at ϕ_1 and Z = 0.75.

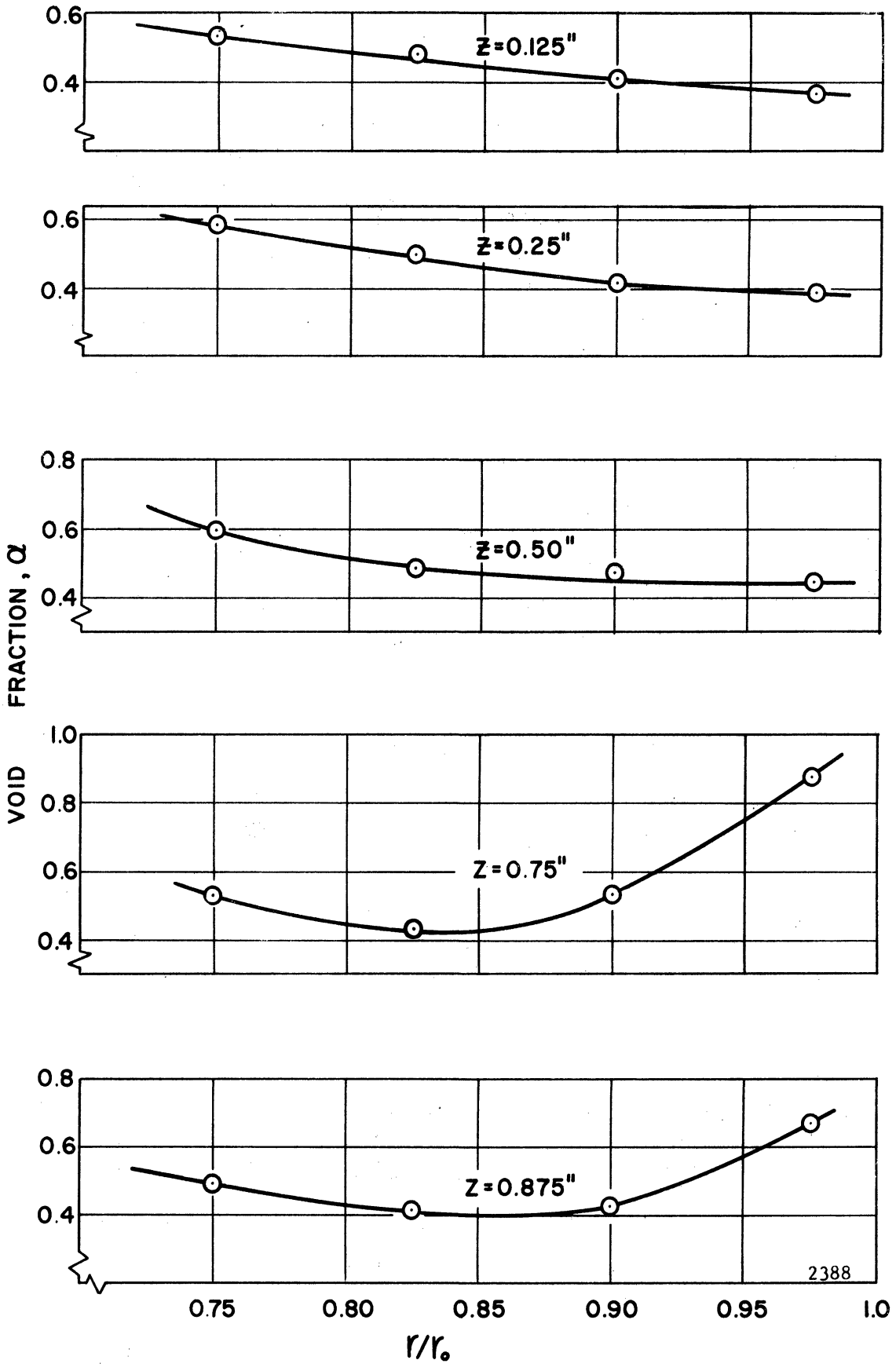

Fig. 5.24 - Radial Distribution of Void Fraction as a Function of Z at $\emptyset_1$. Test Series No. 1.

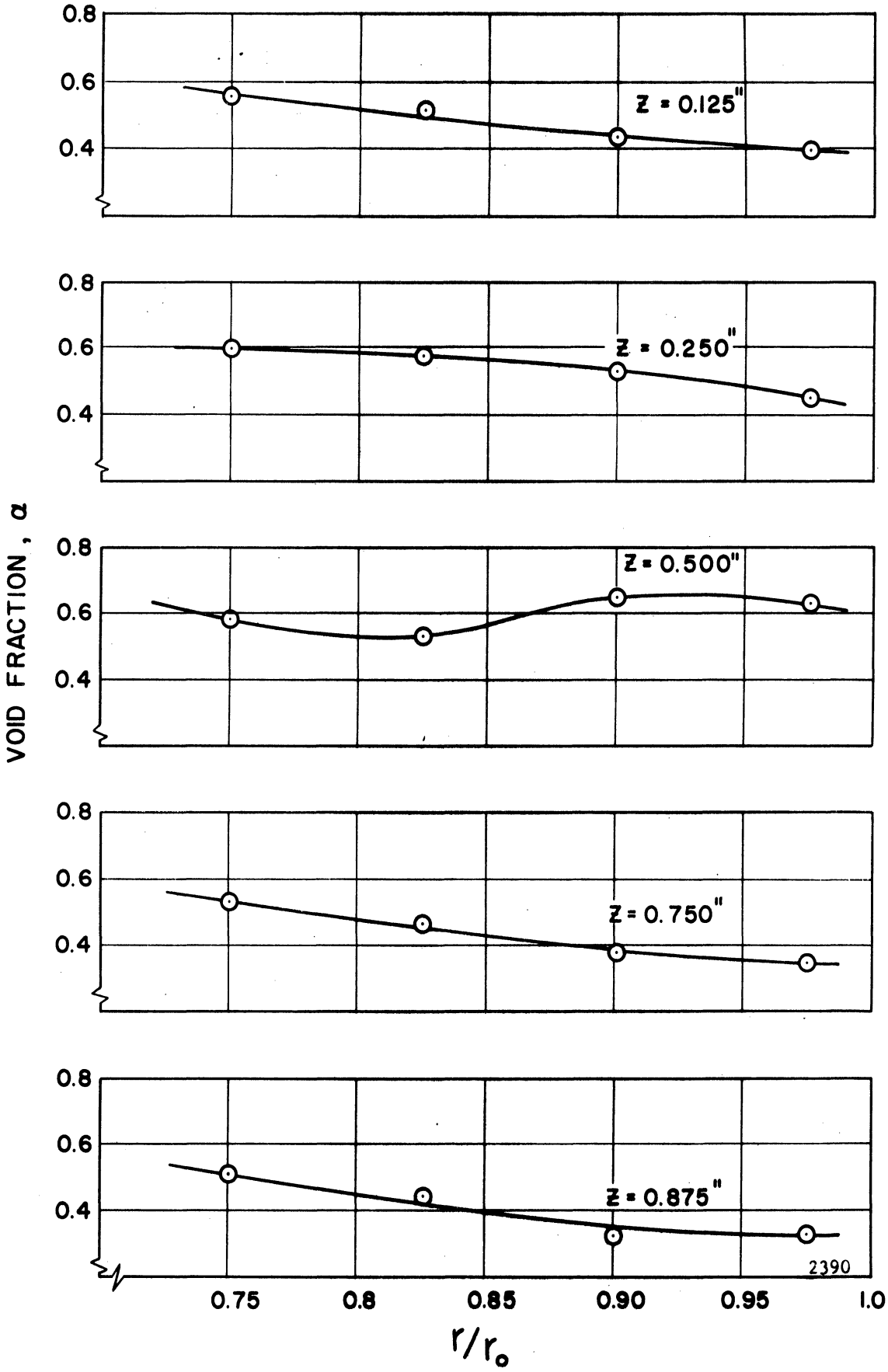

Fig. 5.25 - Radial Distribution of Void Fraction as a Function of Z at $\emptyset_2$. Test Series No. 1.

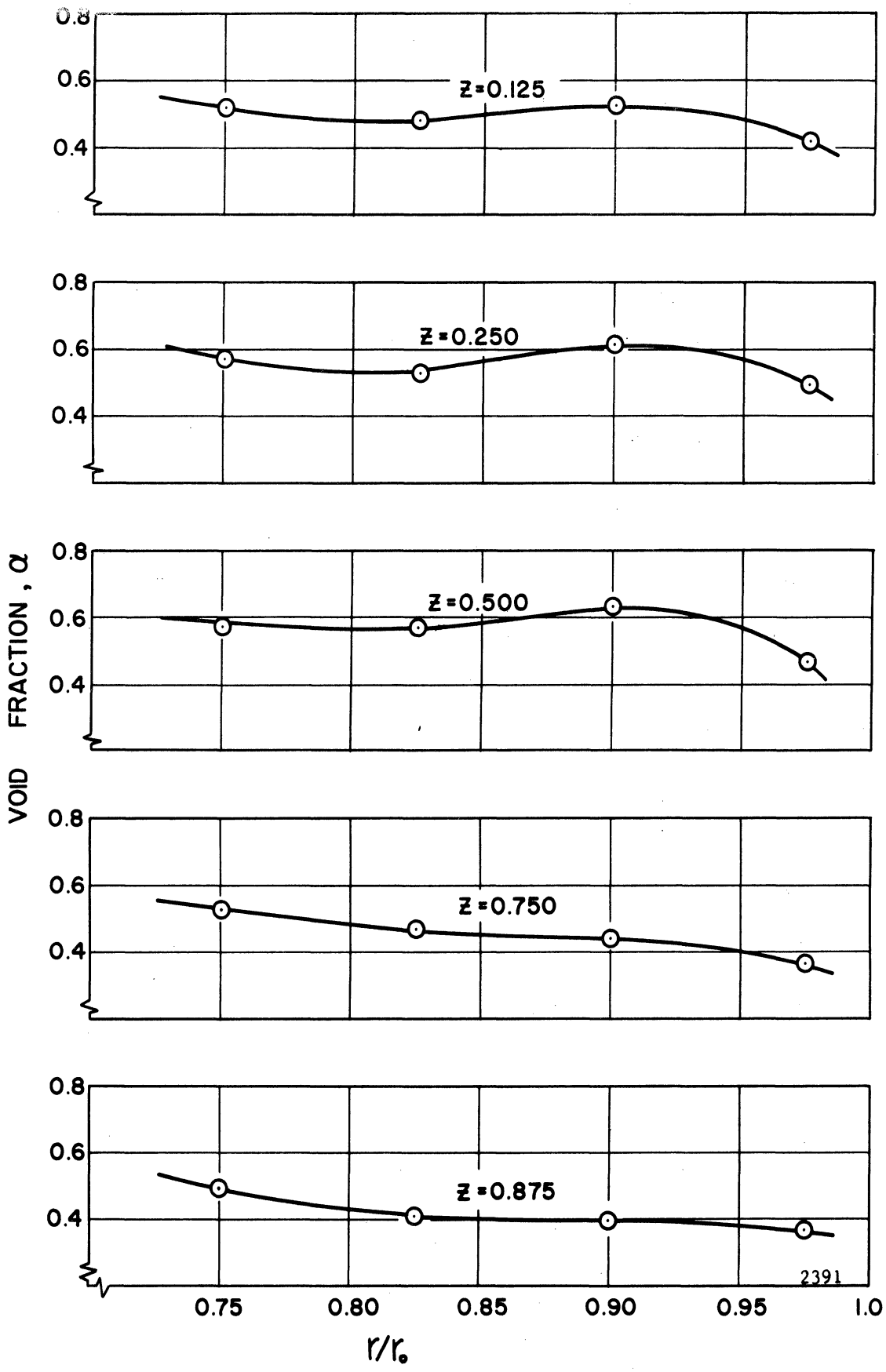

Fig. 5.26 - Radial Distribution of Void Fraction as a Function of Z at $\emptyset_3$. Test Series No. 1.

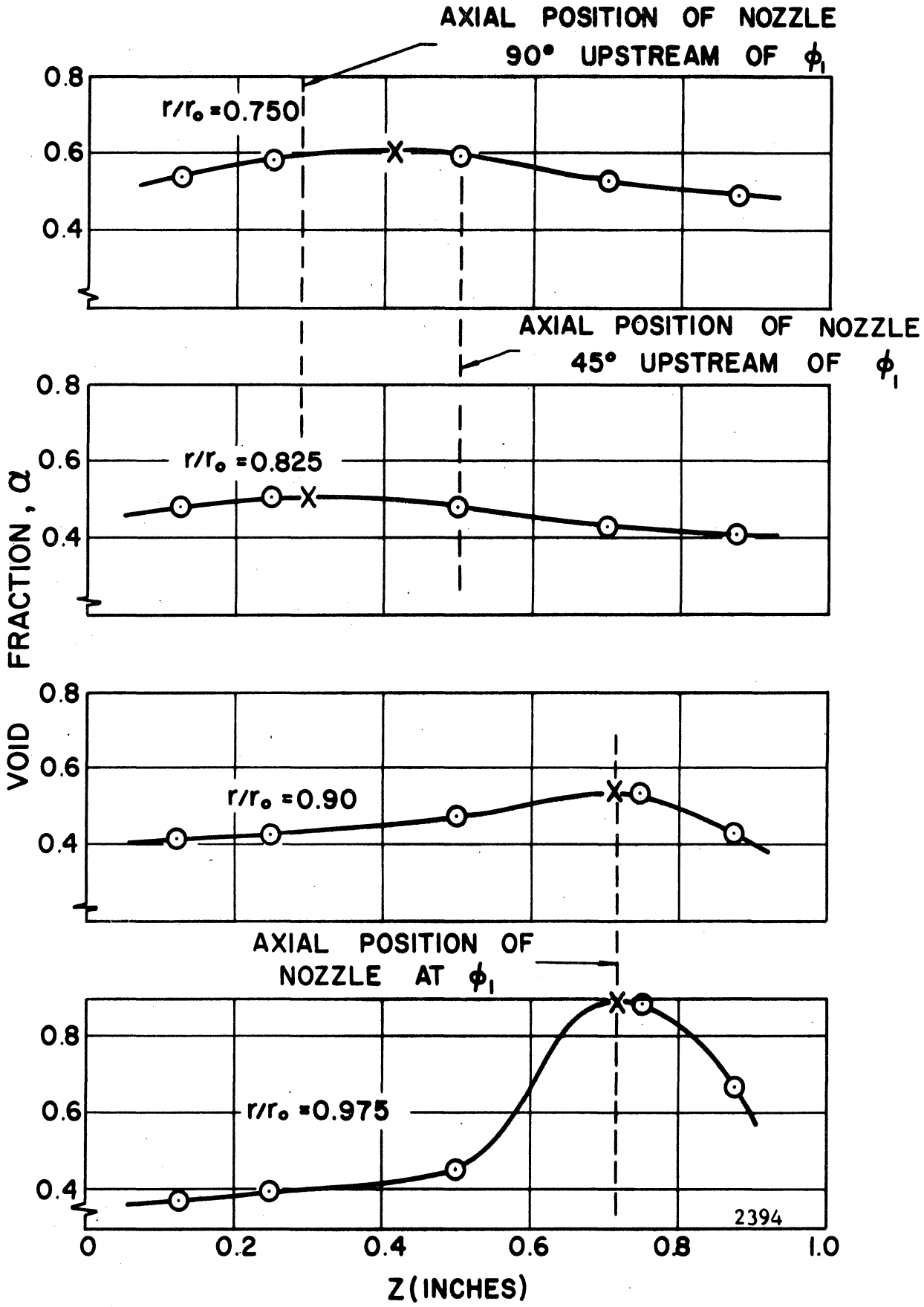

Fig. 5.27 - Axial Distribution of Void Fraction as a Function of Radius at ϕ_1. Test Series No. 1.

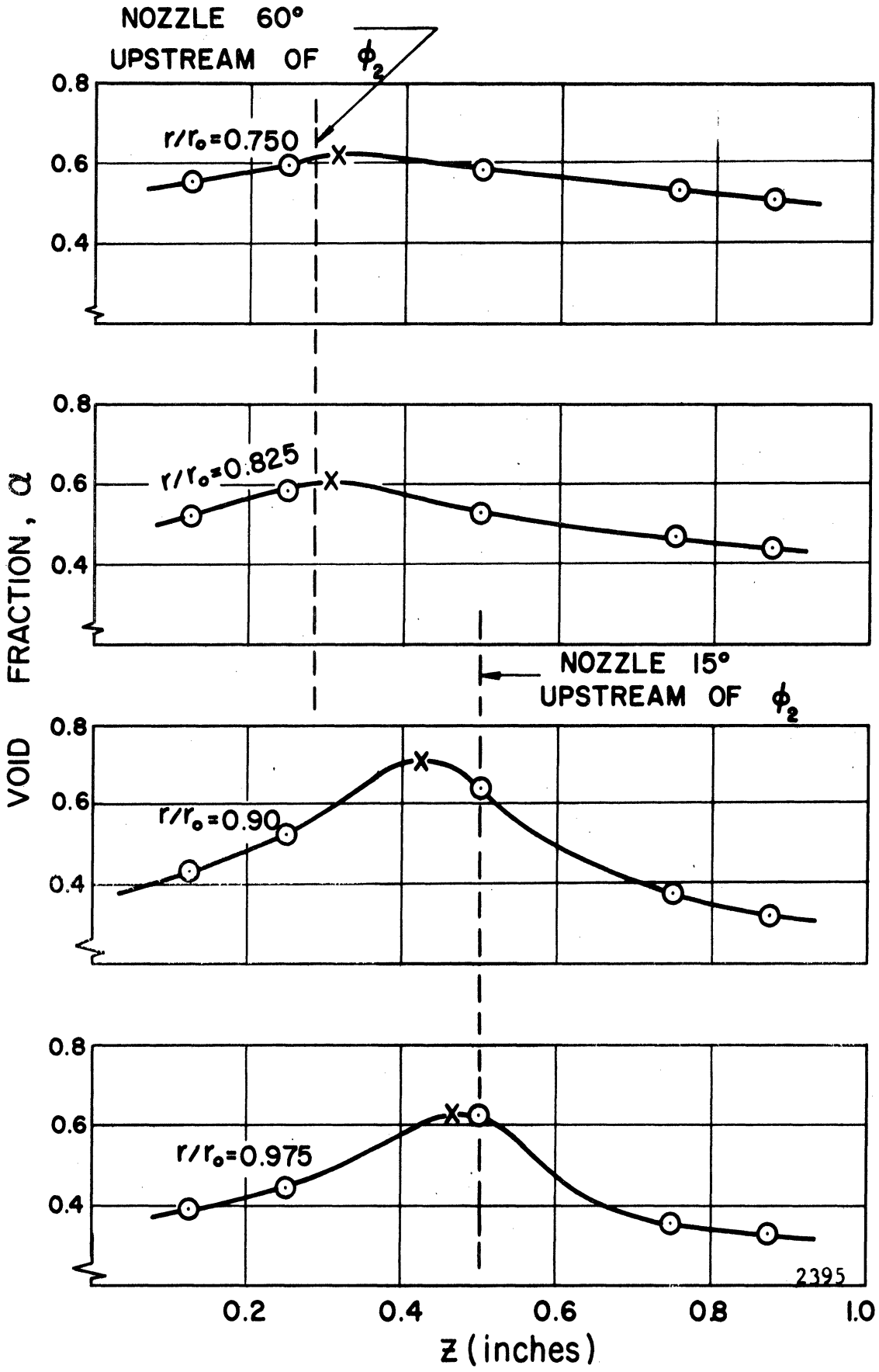

Fig. 5.28 - Axial Distribution of Void Fraction as a Function of Radius at $\emptyset_2$. Test Series No. 1.

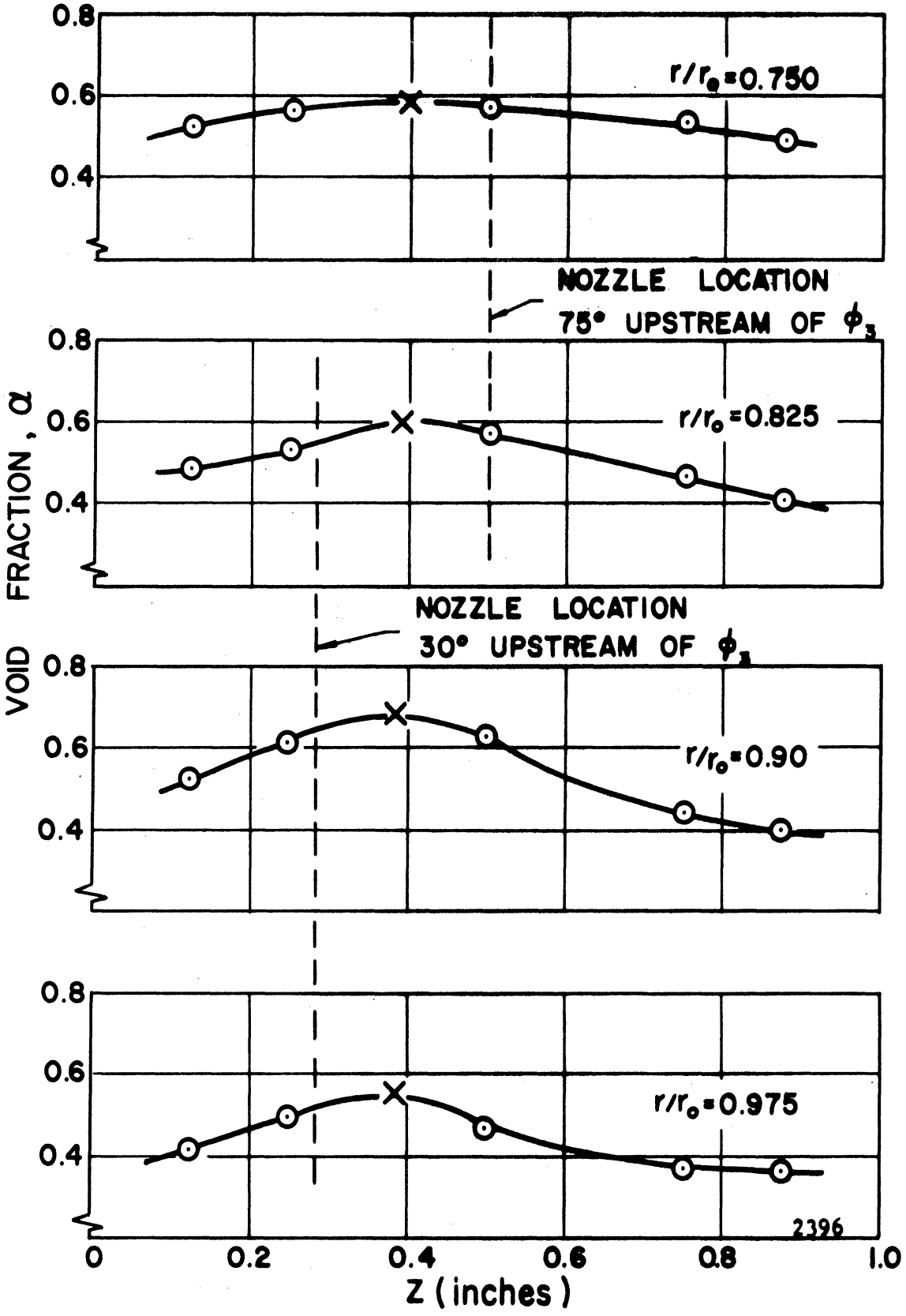

Fig. 5.29 - Axial Distribution of Void Fraction as a Function of Radius at $\emptyset_3$. Test Series No. 1.

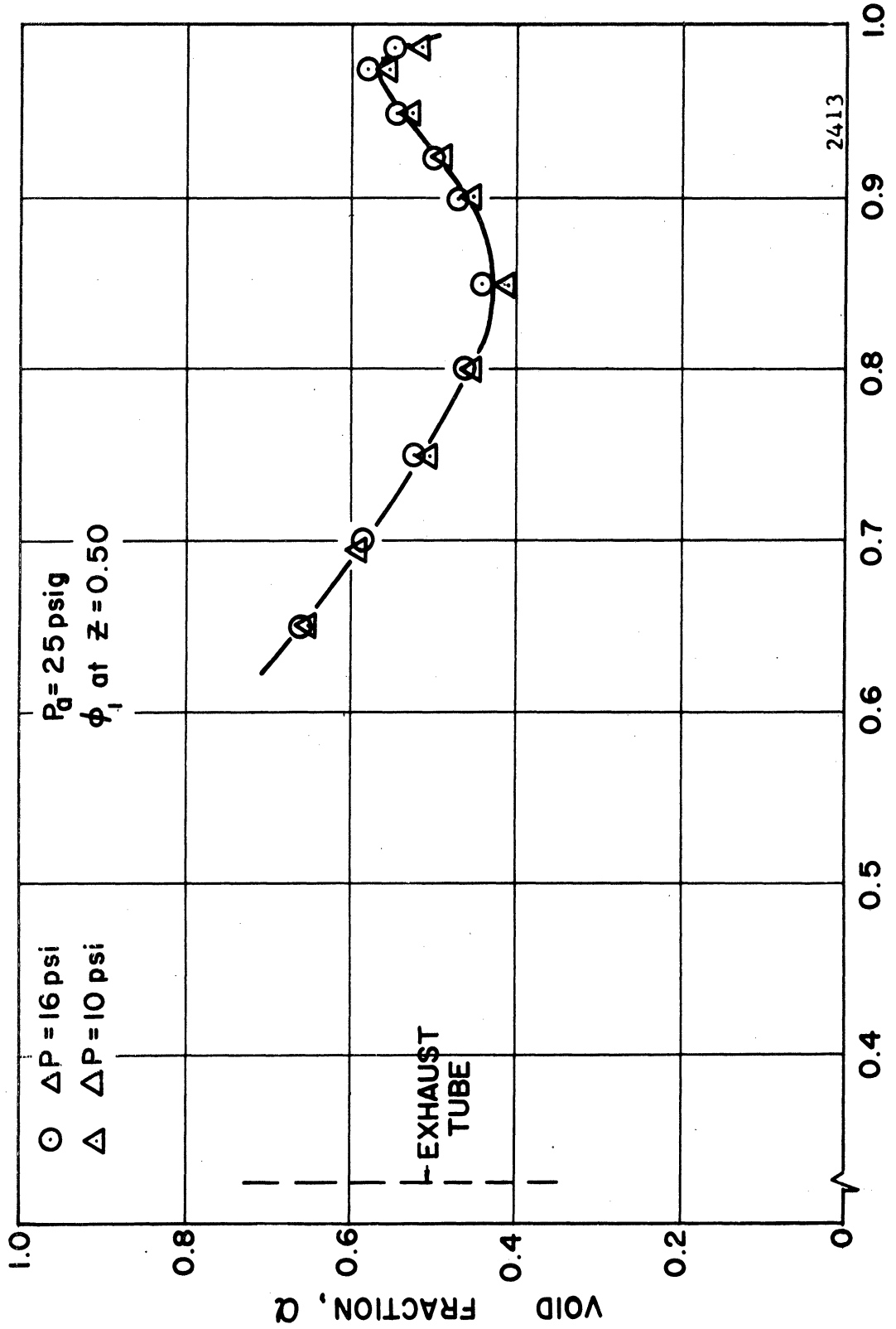

Fig. 5.30 - Radial Distribution of Void Fraction.
Test Series No. 2.

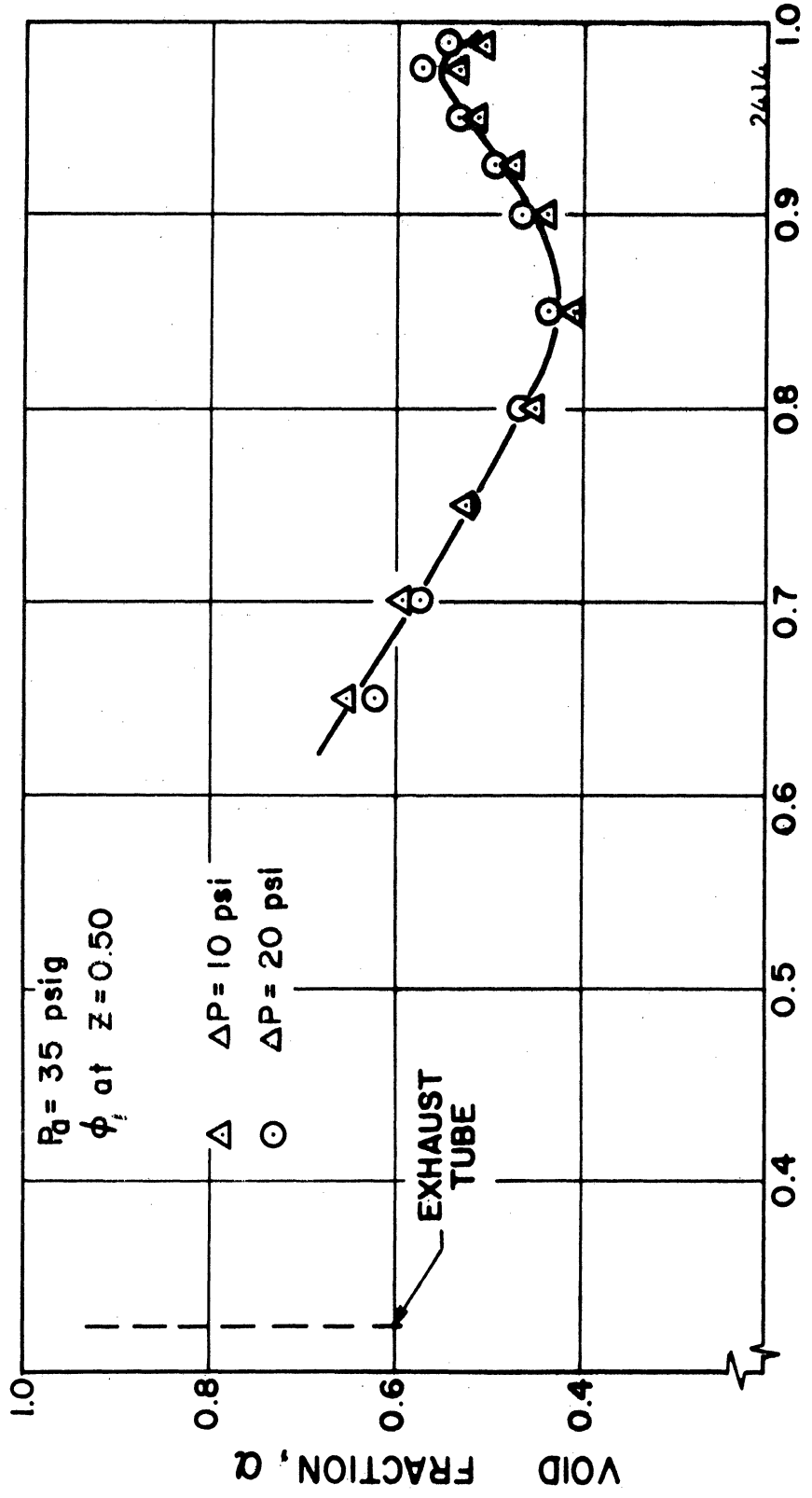

Fig. 5.31 - Radial Distribution of Void Fraction.
Test Series No. 2.

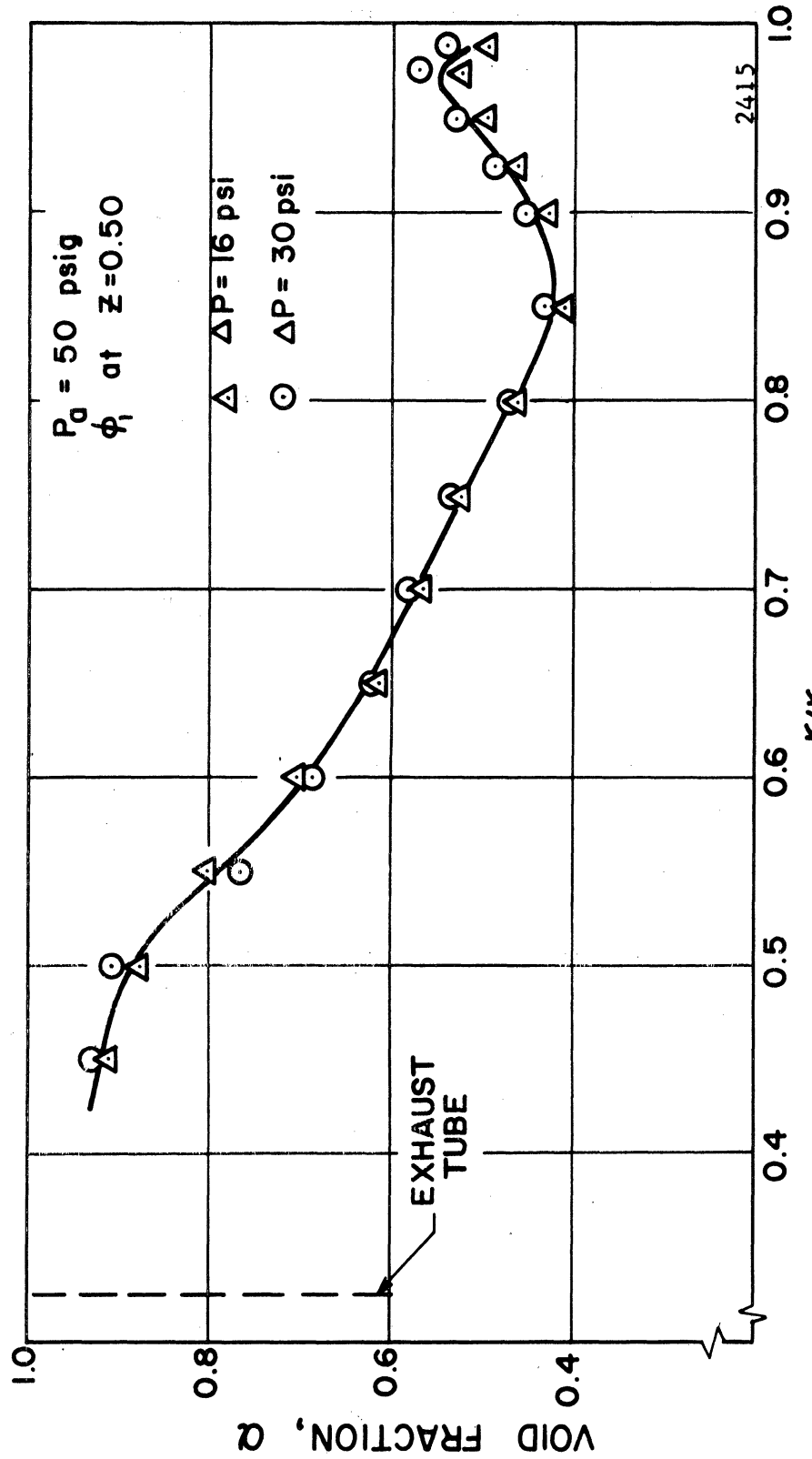

Fig. 5.32 - Radial Distribution of Void Fraction.
Test Series No. 2.

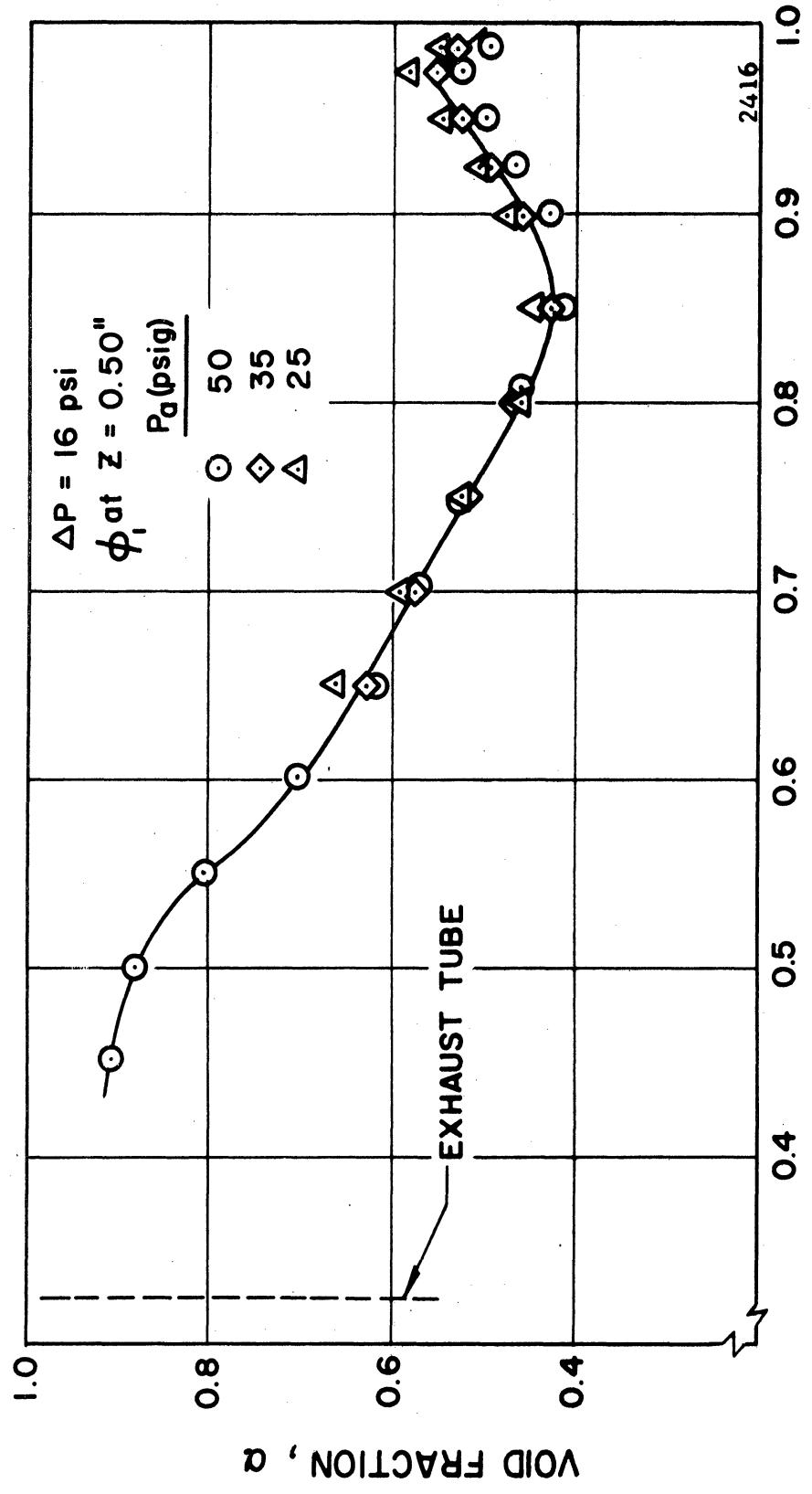

Fig. 5.33 - Radial Distribution of Void Fraction as a Function of P_a at ΔP = 16 psi. Test Series No. 2.

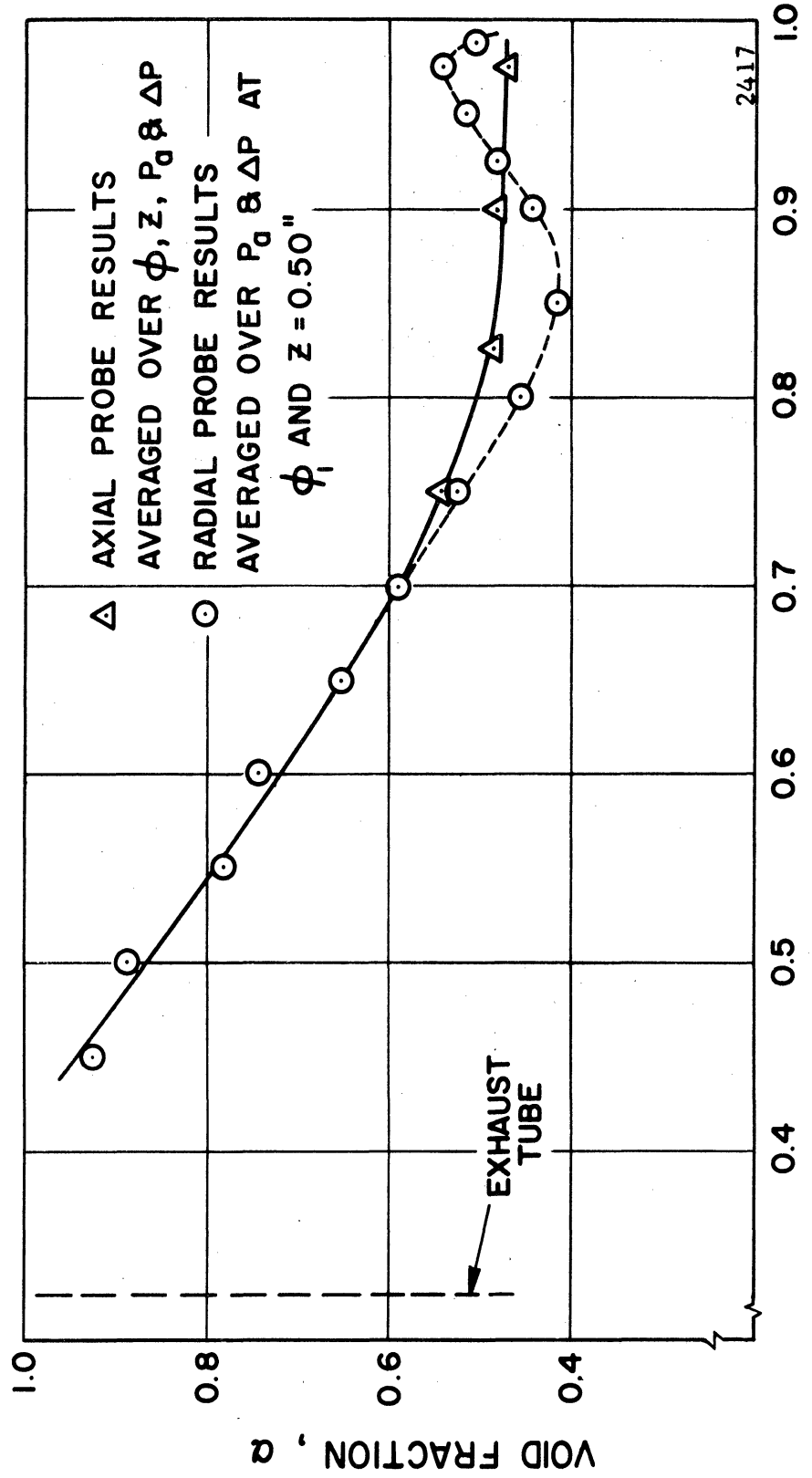

Fig. 5.34 - Radial Distribution of Average Void Fraction.

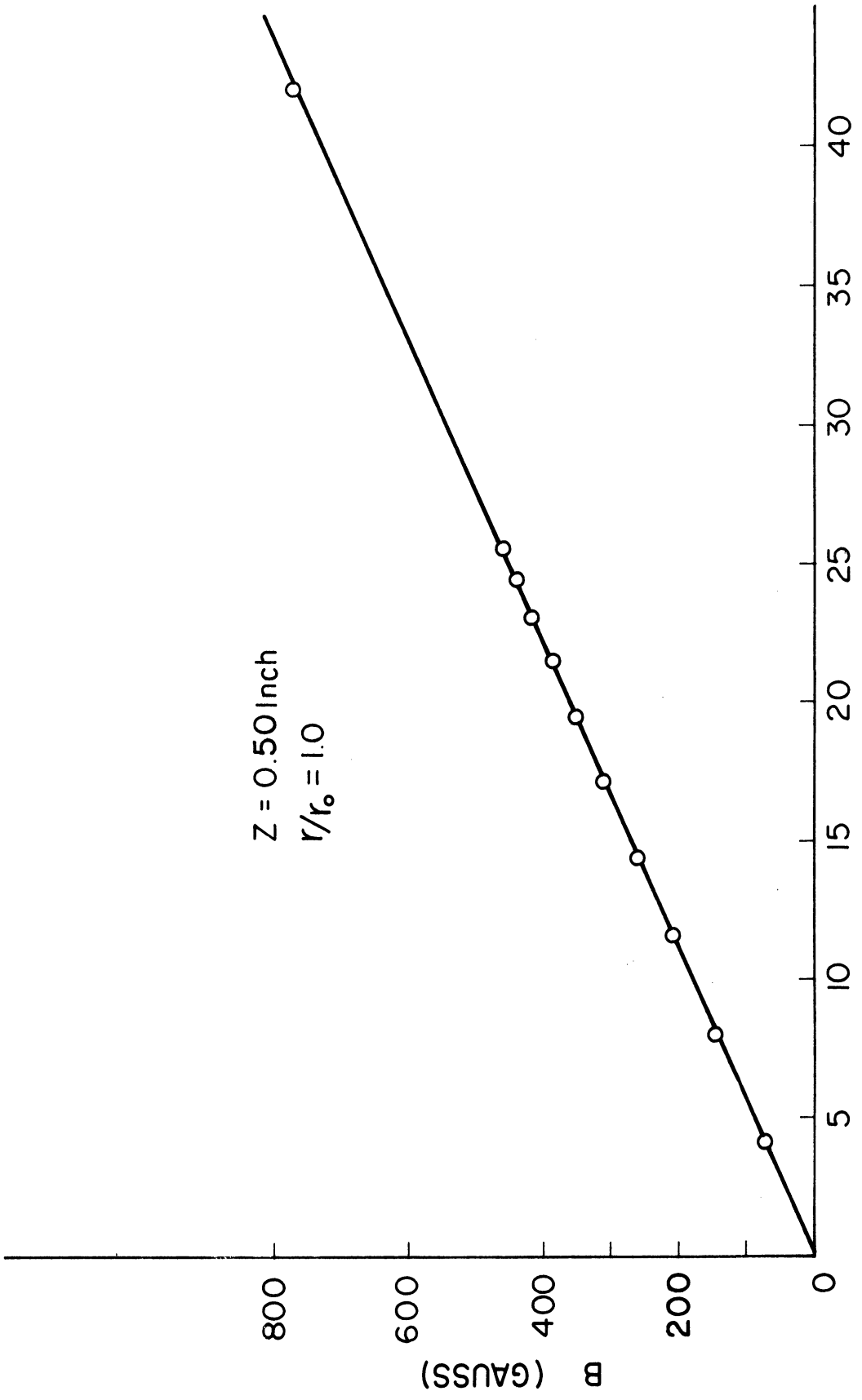

Fig. 5.35 - Variation of Magnetic Flux Density with Coil Current.

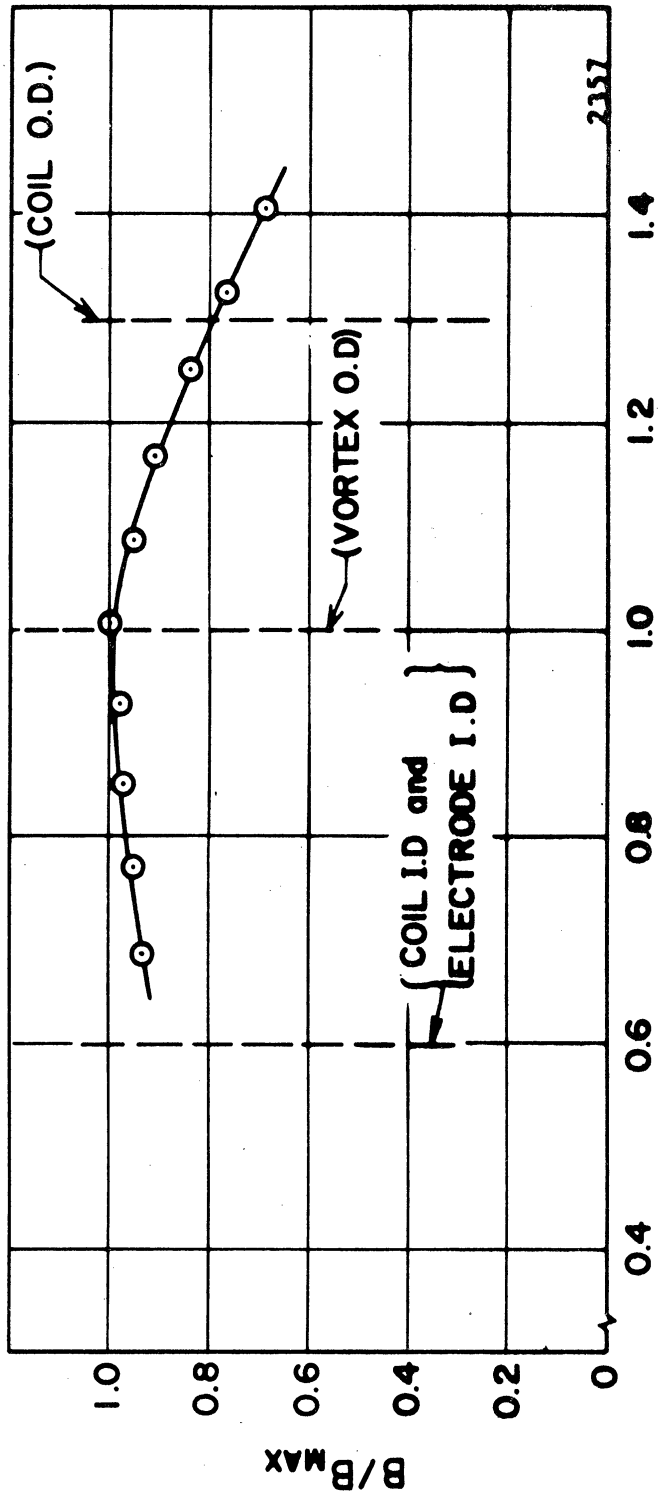

Fig. 5.36 - Radial Distribution of Magnetic Flux Density.

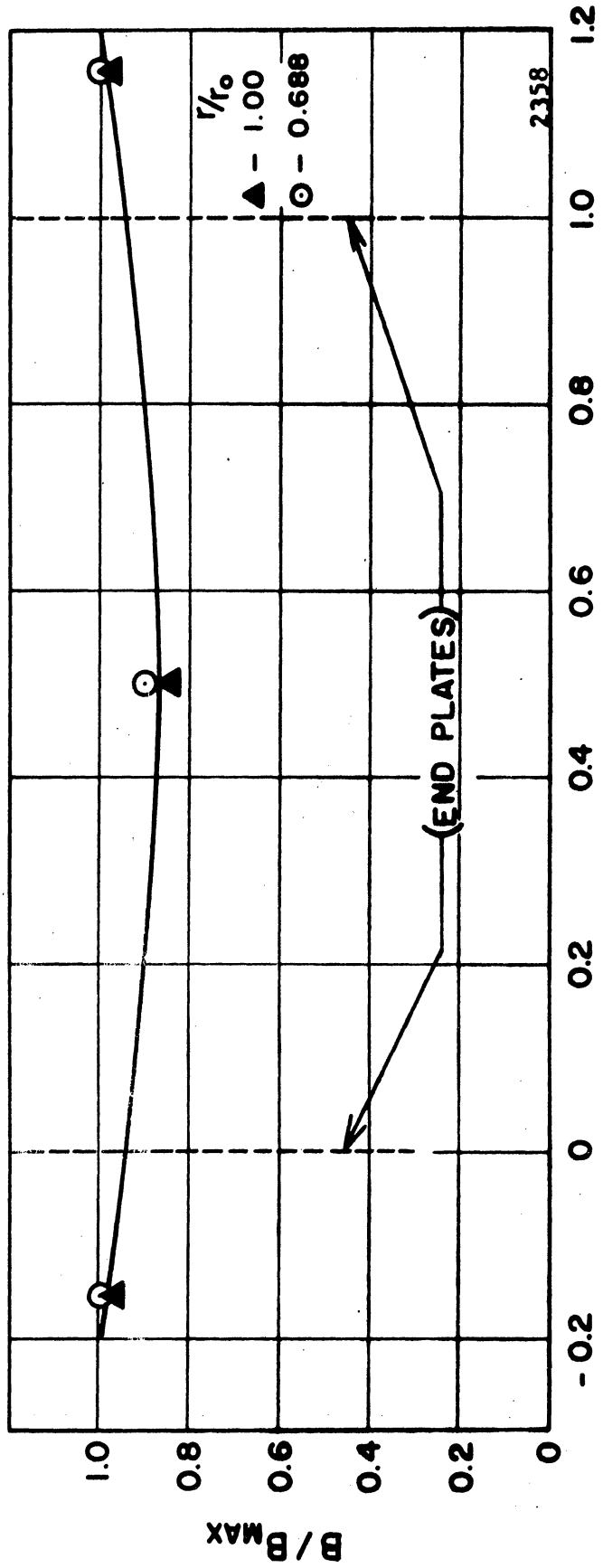

Fig. 5.37 - Axial Distribution of Magnetic Flux Density.

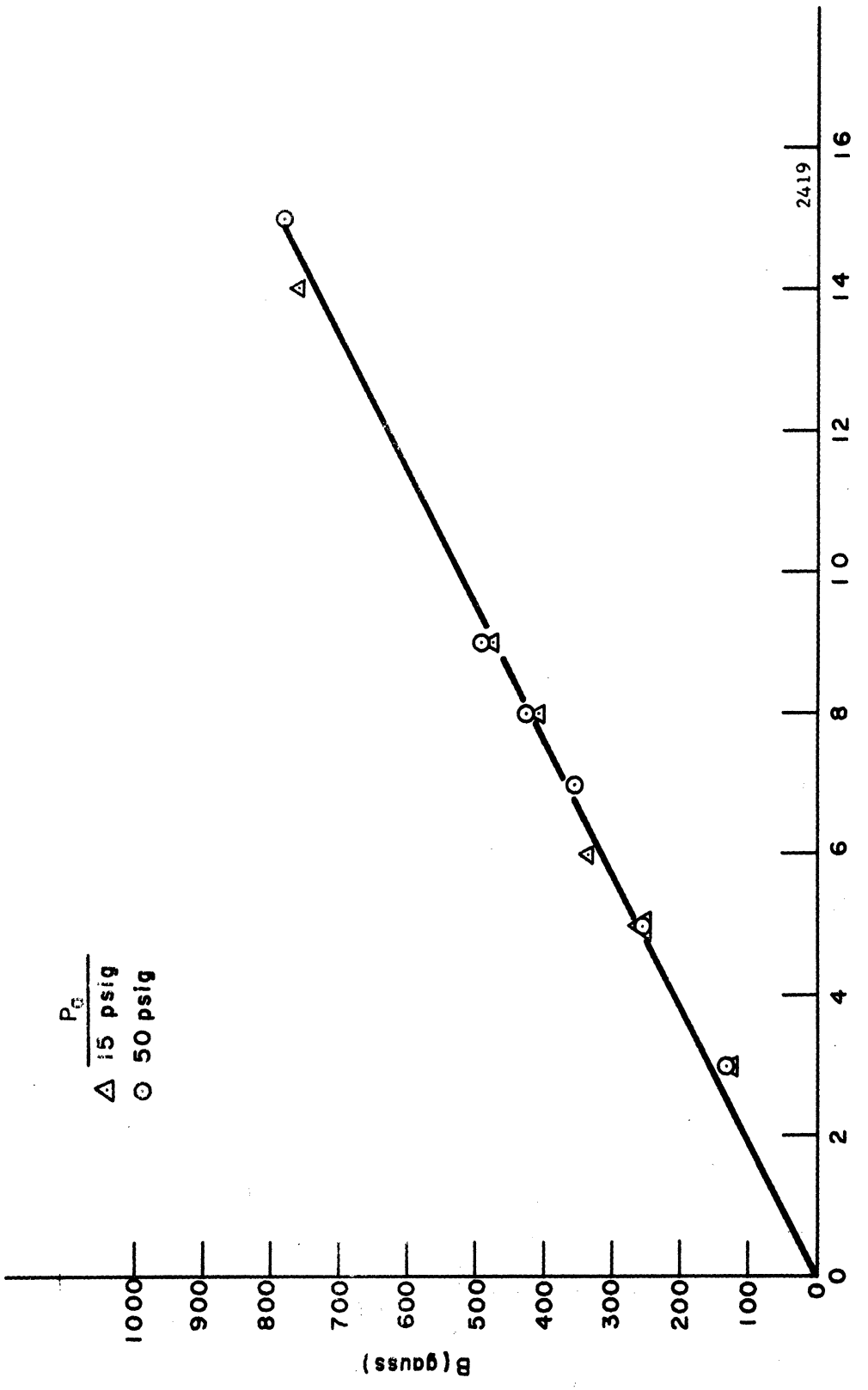

Fig. 5.38 - Open Circuit Voltage as a Function of Magnetic Flux Density and P_a at ΔP = 10 psi.

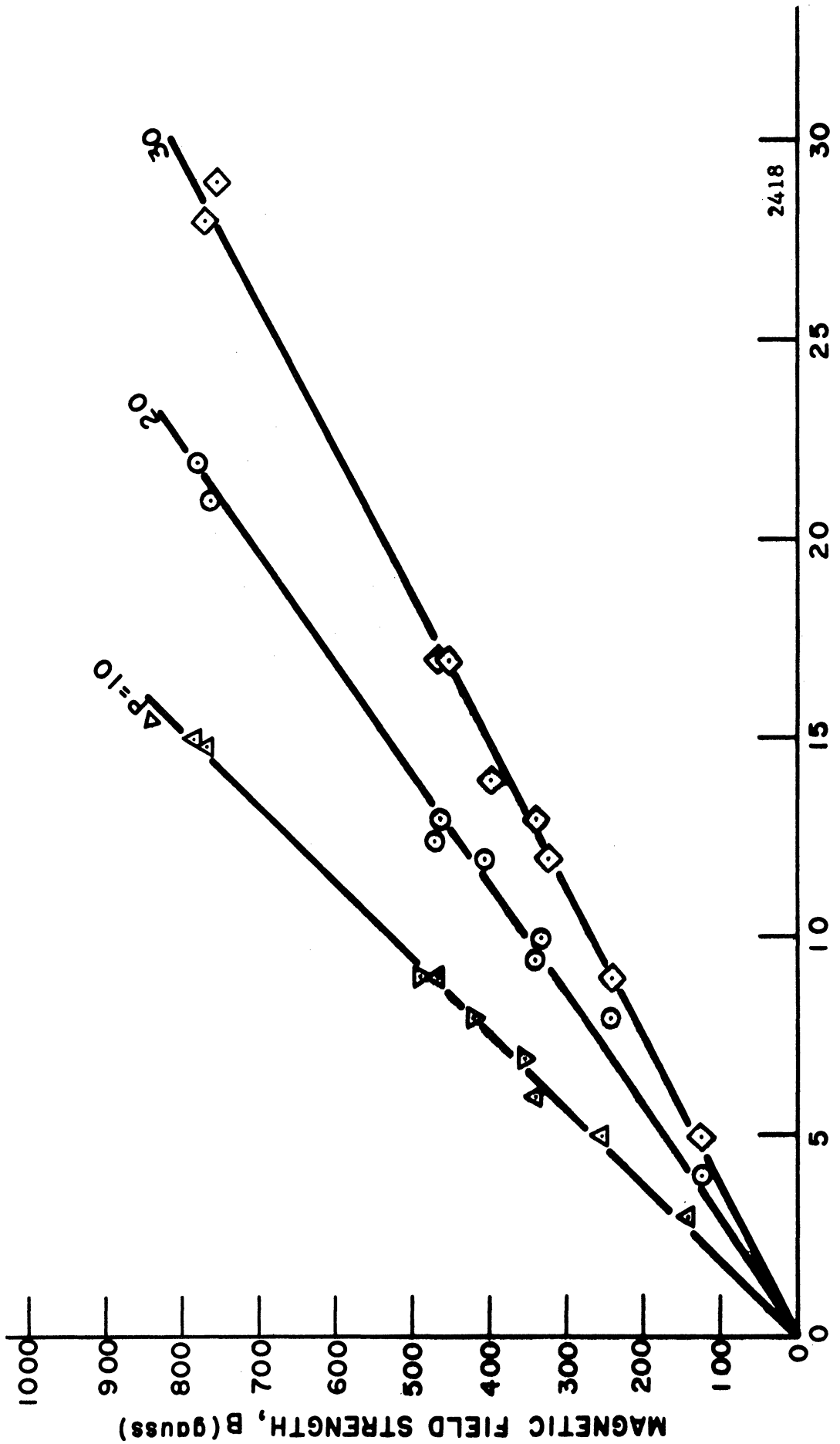

Fig. 5.39 - Open Circuit Voltage as a Function of Magnetic Flux Density and ΔP at P_a = 50 psig.

CHAPTER VI

THEORY

A. Analysis of the Two-Phase Vortex

1. Model and assumptions: In the two-phase vortex flow considered in this investigation, visual observation (of an air-driven water vortex) indicated that a stable flow condition exists in which the net radial flow of the liquid phase is zero except for a small radial inflow through the end wall boundary layers. If the region near the axis of rotation is excluded from the analysis, then it is also reasonable to consider the net axial velocity components to be zero. Under these considerations a relatively simple physical model of the flow can be formulated. The analysis considers a geometry as shown in Fig. 6.1 where the radial and tangential velocity components of the vapor (or gas)* phase are designated by the lower case symbols u and v respectively, and the corresponding liquid velocity components are represented by U and V. The analysis is based on the following assumptions:

a. $v \gg u$ at $r = r_o$

b. $U = 0$

c. $d/d\emptyset = d/dz = 0$ everywhere

*In this discussion "vapor" is used to designate all gaseous components.

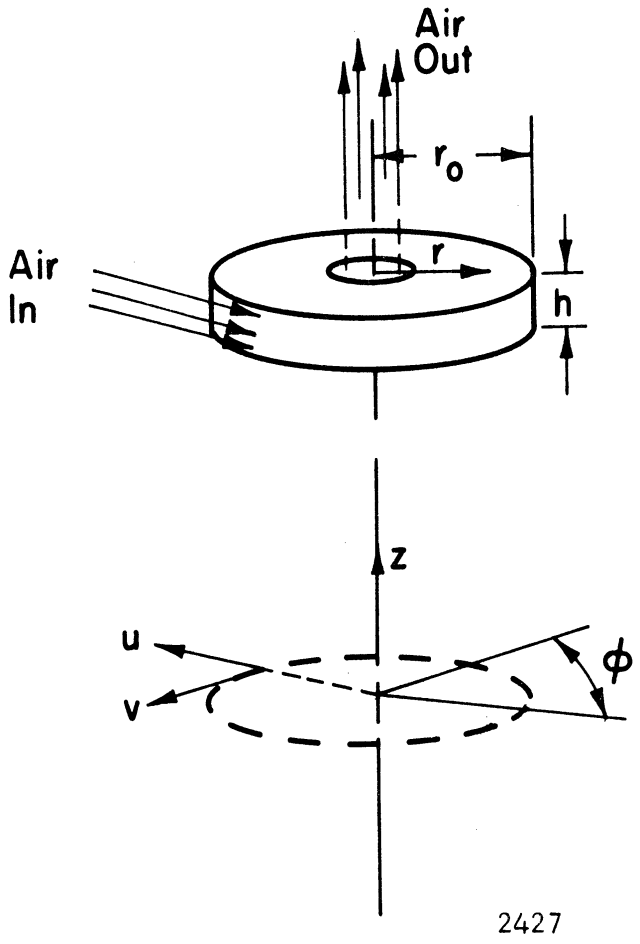

Fig. 6.1 - Schematic Representation of the Vortex.

d. The axial components of velocity are everywhere zero

e. The temperature is everywhere constant within the vortex

f. Condensation and evaporation are negligible

g. Gravity effects are negligible

h. The viscous shear forces within the mixture are negligible compared to the drag forces on the end plates for any annular element taken as a free body

i. The flow is in the "mist" flow regime.

The model based on these assumptions contains the five dependent variables v, V, α, u, and p (see definition of symbols on page x). If the radial pressure distribution p(r) and the void fraction distribution $\alpha(r)$ are specified or measured experimentally for a given value of the air mass flow rate $\mathring{m}$, three equations are necessary to determine the radial profiles of v, u and V. Three independent equations can be formulated within the restrictions of the listed assumptions of the model by considering the balance of the radial and angular momentum fluxes and the conservation of mass.

2. Angular momentum flux balance: Considering an annular element of the two-phase mixture of thickness dr and height h, the change in the angular momentum flux is, according to assumption b, due to the vapor only and can be expressed as

$$d\mathring{M}_{\emptyset} = \mathring{m} \frac{d}{dr}(rv)\, dr \,. \qquad (6.1)$$

This change in the momentum flux is balanced by the torque exerted on the element by the drag forces. If the net viscous shear forces due to the adjacent elements of the mixture are ignored, as indicated by assumption h, the retarding force on the element is due only to the tangential component of the drag of the element on the end plates. In order to express the two-phase drag force it is necessary to resort to empirical results.

In the investigation of two-phase drag coefficients and friction factors, it has become customary in the literature[35,46,48] to express the phase velocities in terms of "superficial" velocities defined as

$$\text{Superficial liquid velocity} = V_s = (1 - \alpha)V \qquad (6.2)$$

$$\text{Superficial gas velocity} = v_s = \alpha v \qquad (6.3)$$

In two-phase pipe flow a superficial friction factor f_s is defined in terms of the two-phase pressure drop and the superficial gas velocity by

$$\frac{\Delta P}{\Delta L} = -\frac{f_s}{2}\frac{\rho_g v_s^2}{D} \qquad (6.4)$$

where D is the pipe diameter and ΔP is the pressure drop in the distance ΔL.

In order to express Equation (6.4) in terms of a drag force and a corresponding drag area, both sides are multiplied by A ΔL, the total flow area of the pipe times the length of the flow element. The left hand side of the

equation is then seen to be the pressure force on the flow element, and, in terms of the pipe cross sectional area $\pi D^2/4$,

$$F = - \frac{f_s}{2} \frac{\rho_g v_s^2}{D} \frac{\pi D^2 \Delta L}{4} = - \frac{f_s}{8} \rho_g (\alpha v)^2 A_D \qquad (6.5)$$

where A_D is the wall drag area.

Chien and Ibele[48] have found, for the mist flow regime in pipes, that the relationship

$$f_s = 0.272 \frac{(Re_L)_s^{0.517}}{(Re_g)_s^{0.468}} \qquad (6.6)$$

provides a very good correlation of f_s with an extensive amount of experimental data over the range of superficial liquid Reynolds numbers

$$10^3 < (Re_L)_s < 3 \times 10^4$$

and gas Reynolds numbers between $1.199 \times 10^6 (Re_L)_s^{-0.301}$, the experimentally determined point of transition from annular to annular mist flow, and 4×10^5.

Assuming that f_s for two-phase flow between flat plates has the same parametric dependence as that expressed by Equation (6.6), the friction factor associated with the drag on the end plates of the two-phase vortex is approximated by

$$f_s = k \frac{(2hV_s/\nu_L)^{0.517}}{(2hv_s/\nu_g)^{0.468}} \qquad (6.7)$$

where k is a constant corresponding to the factor 0.272 in

Eq. (6.6) and the hydraulic diameter for the vortex chamber with small L/D is approximated by 2h. Replacing the superficial velocities by the actual phase velocities by use of Eq. (6.2) and (6.3), the superficial friction factor becomes

$$f_s = k \frac{(RT\mu_g/2h)^{0.468}}{(\nu_L/2h)^{0.517}} \frac{(1-\alpha)V^{0.517}}{(\alpha v)^{0.468}} P^{-0.468} \qquad (6.8)$$

where the density term in the gas Reynolds number has been replaced by P/RT.

Applying equation (6.5) to the annular element of the two-phase vortex, $A_D = 2(2\pi r\, dr)$, and the tangential drag force on the element is

$$dF_\phi = -\frac{f_s}{2} \pi \rho_g (\alpha v)^2 r\, dr \qquad (6.9)$$

and using f_s for the vortex from Equation (6.8),

$$dF_\phi = -K P^{0.532} (\alpha v)^{1.532} [(1-\alpha)V]^{0.517} r\, dr \qquad (6.10)$$

where

$$K = \frac{k}{2} \frac{(RT\mu_g/2h)^{0.468}}{(\nu_L/2h)^{0.517}} \frac{\pi}{RT} \qquad (6.11)$$

and the vapor density term has been replaced by p/RT from the ideal gas law.

Then, equating the change in the momentum flux $d\dot{M}_\phi$ (Equation 6.1) to the torque $F_\phi r$, expressed by the use of Equation (6.10), there results

$$\frac{d}{dr}(rv) = -\frac{K\, r^2\, P^{0.532}}{\dot{m}} (\alpha v)^{1.532} [(1-\alpha)V]^{0.517} \quad (6.12)$$

It is emphasized that the validity of this result is restricted to the mist flow regime which excludes very low values of the void fraction. Examination of Equation (6.10) shows that the use of the empirical friction factor correlation does not result in the correct asymptotic behavior as the void fraction approaches unity since the drag force approaches zero rather than the single phase gas drag force. Hence, Equation (6.12) is not valid for either extreme of void fraction values.

3. Radial Momentum Flux Balance: The change in the radial momentum flux across the annular element is given by

$$d\dot{M}_r = \dot{m}\,(du/dr)\,dr \quad (6.13)$$

and, neglecting the radial drag force of the radial vapor flow on the end plates, this is balanced by the centrifugal force F_c and the net radial pressure force F_p. The centrifugal force on the element is given by the sum of the centrifugal forces on the two phases as

$$F_c = \left[\frac{m_g v^2}{r} + \frac{m_L V^2}{r}\right]$$

$$= 2\pi h \left[\alpha \rho_g v^2 + (1-\alpha)\ \rho_L V^2\right] dr \quad (6.14)$$

and the pressure force is

$$F_p = -2\pi h\, r(dp/dr)\, dr\ . \tag{6.15}$$

Then equating the summation of F_c and F_p from Equations (6.14) and (6.15) to Equation (6.13) gives

$$\frac{\dot{m}}{2\pi h}\frac{du}{dr} = -r\frac{dp}{dr} + \left[\alpha\rho_g v^2 + (1-\alpha)\rho_L V^2\right] \tag{6.16}$$

4. Conservation of Mass: Using the basic mass conservation equation for the radial air flow, the mass flow rate is expressed in terms of the velocity by

$$\dot{m} = \rho_g A\, u \tag{6.17}$$

and noting that the area available for radial air flow at r is $2\pi rh\alpha$, the radial air velocity is seen to be

$$u = \frac{\dot{m}}{2\pi h\alpha\rho_g r} = \frac{\dot{m}RT}{2\pi h\alpha p\, r} \tag{6.18}$$

where the ideal gas law has again been employed to express the vapor density in terms of the pressure and temperature.

With a reasonable estimate of K and the measurement of $\alpha(r)$, P(r) and $\dot{m}$, the radial distributions of v(r), u(r) and V(r) are defined by Equations (6.12), (6.16) and (6.18).

B. Velocity Estimates by Impact Pressure

If a pitot tube is inserted into a fluid stream with the opening facing into the flow, the impact pressure (total

pressure - static pressure) for a single phase, incompressible, flow is given by Bernoulli's equation as

$$(P_t - P) = \frac{1}{2} \rho V^2 \qquad (6.19)$$

This assumes, in addition to incompressible flow, that the viscous losses from free stream to stagnation at the probe are negligible, and that the flow is steady and sub-sonic. For air at STP it has been shown[49] that if compressibility is neglected and the remaining assumptions are valid, the correction factor for the velocity determined by Equation (6.19) is on the order of 1.05 for V = 500 ft/sec. For an air velocity of 1000 ft/sec the correction factor has increased to about 1.21.

For the case of two-phase flow, assuming a homogeneous mixture of the two phases, the impact pressure sensed by the pitot tube would be expressed as the sum of the impact pressures of the two phases as

$$(P_t - P) = \frac{1}{2} \alpha \rho_g v^2 + \frac{1}{2} (1 - \alpha) \rho_L V^2 \qquad (6.20)$$

which is subject to the same restrictions as Equation (6.19). In terms of the slip ratio S = v/V, the two phase impact pressure is

$$(P_t - P) = \frac{1}{2} (1 - \alpha) \rho_L V^2 \left[1 + \frac{\alpha}{(1 - \alpha)} \frac{\rho_g}{\rho_L} S^2 \right]. \qquad (6.21)$$

For a pressure of 1 atmosphere, a void fraction of 0.90 and S = 2, the second term in the brackets of Equation (6.21) is

about 0.044. The liquid velocity can then be predicted under these conditions with an error of 2.2% by neglecting the entire term in the brackets provided the basic assumptions are valid. With a void fraction of 0.50 and a pressure of 4 atmospheres, V can be determined with the same degree of accuracy with slip ratios as high as 3. It would then appear that use of the relationship

$$V = \left[\frac{2(P_t - P)}{(1 - \alpha)\ \rho_L}\right]^{1/2} \qquad (6.22)$$

should give reasonable estimates of the liquid velocities in two-phase flow. Shires and Riley,[36] however, performed an extensive series of tests, using air and water, in which impact pressures were measured in conjunction with an independent determination of the phase velocities by isokinetic sampling techniques. Although they did not investigate the validity of Equation (6.22) insofar as the prediction of liquid velocities is concerned, their data, limited to liquid velocities below 9 ft/sec with slip ratios as high as 3 and void fractions ranging from 0.1 to 0.73, show that the liquid velocities predicted by Equation (6.22) were uniformly low by about 30%. It is then evident that with the use of impact pressure measurements, the Bernoulli equation will give only a rough estimate of the free stream liquid velocities at low values of V. In considering the validity of Equation (6.22), it should be noted that the sonic velocity in a two-phase mixture can be an order of

magnitude less than that for either phase considered separately,[50] and hence on the order of the velocities considered here. It is thus possible for Mach number effects to be appreciable, and in fact, "condensation shocks" have been observed in similar cases.[51]

C. Electromagnetic Effects

When a conducting fluid is flowing with a uniform velocity V in the presence of a magnetic field of flus density B normal to V, there results án electric field intensity, normal to V and B, of magnitude

$$|\bar{E}| = |\bar{V} \times \bar{B}| = B\,V \tag{6.23}$$

for open circuit operation. Kolin[52] has shown that, for a channel of circular cross section and diameter D, the potential E_o produced across the channel is

$$E_o = D\,B\,V_{av} \tag{6.24}$$

provided B is constant across the channel and the velocity distribution is axisymmetric. Arnold[53] analyzed the case of a channel of rectangular cross section and was able to show that

$$E_o = b\,B\,V_{av} \tag{6.25}$$

where b is the width of the channel in the direction of E. This result is valid for the case in which the electrodes span the breadth of the channel and for an arbitrary velocity distribution.

Unfortunately, the difference in geometry between the straight channel flow and vortex flow prohibits a simple result analogous to Eq. (6.25) in the vortex case except in special cases. For the vortex flow of an annulus of conducting fluid, as shown in Fig. 6.2, a radial magnetic field B which is constant with r and Ø will result in an induced electric field intensity E(r) which is equal to BV(r) for open circuit operation if V is a function of r only.

If annular electrodes are installed at Z = 0 and Z = h such that they bound fluid annulus, the net potential E_o between the plates will be independent of r (assuming the electrodes to be perfect conductors). For a small annular element of the flow of thickness dr and height h, the current through the element in the Z-direction is

$$dI = \sigma(E - E_o/h)\, dA \tag{6.26}$$

where

σ = conductivity of the fluid at r

$dA = 2\pi r\, dr$

Since the net current flow through the region bounded by the electrodes must be zero for open circuit conditions for the unit as a whole,

$$\int_A dI = 0 = 2\pi \int_{R_1}^{R_2} \sigma(E - E_o/h)\, r\, dr\ . \tag{6.27}$$

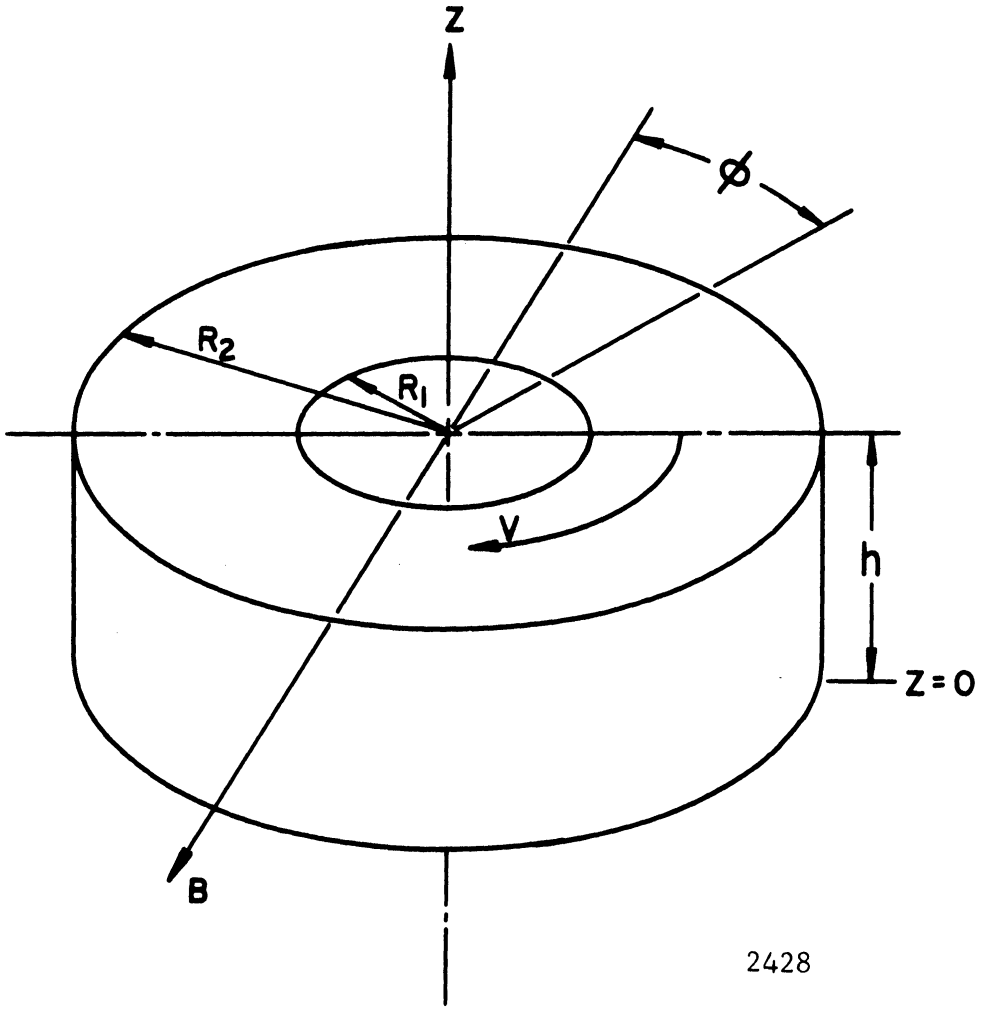

Fig. 6.2 - Schematic Representation of the Vortex in the Presence of a Magnetic Field.

It was shown in Chapter III that the local conductivity of a two-phase air-water flow can be approximated by

$$\frac{\sigma}{\sigma_o} = 1 - \alpha . \tag{6.28}$$

Using this result and replacing E by BV, Equation (6.27) becomes

$$\int_{R_1}^{R_2} (1 - \alpha)(BhV - E_o)\, r\, dr = 0 \tag{6.29}$$

and solving for E_o

$$E_o = Bh \frac{\int_{R_1}^{R_2} (1 - \alpha) V\, r\, dr}{\int_{R_1}^{R_2} (1 - \alpha) r\, dr} \tag{6.30}$$

In this result it is seen that the variable void fraction and the r-term resulting from the geometry prevent the integral in the numerator from being interpreted as simply the average fluid velocity. The simple (but not necessarily practical) case, in which $\alpha(r)$ is constant and the liquid velocity is a linear function of radius, can be solved analytically, i.e., taking $V = a\, r$ (wheel flow),

$$E_o = (2/3)Bha \left[\frac{R_2^3 - R_1^3}{R_2^2 - R_2^2} \right] \tag{6.31}$$

and introducing the average fluid velocity V_{av} as

$$V_{av} = \frac{\int_{R_1}^{R_2} a\, r\, dr}{R_2 - R_1} = a\,\frac{R_2^2 - R_1^2}{2(R_2 - R_1)} \tag{6.32}$$

E_o can be expressed as

$$E_o = (4/3)Bh\left[\frac{R_2^4 - R_2R_1^3 - R_1R_2^3 + R_1^4}{R_2^4 - 2R_1^2R_2^2 + R_1^4}\right] V_{av} \tag{6.33}$$

and if R_2/R_1 is less than about 2,

$$E_o \approx (4/3)BhV_{av} \tag{6.34}$$

from which a rough estimate of the fluid velocity can be obtained from measurements of the open circuit voltage with a known magnetic field. Since the variation of void fraction with radius is known from experimental measurements, a realistic solution of Eq. (6.30) will be possible when V(r) is determined. The values of E_o thus obtained can then be compared to those values obtained from direct measurements of the open circuit voltage, providing an independent verification of V(r).

CHAPTER VII

APPLICATION OF THE THEORY AND COMPARISON OF RESULTS

A. The Analytical Model

In the investigation of single-phase forced vortices it has generally been found that the term in the radial momentum flux balance (Eq. 6.18) involving du/dr is negligible compared to r(dP/dr).[25,54] In the case of the two-phase vortex, neglect of the du/dr term should be even more justifiable since the void fraction has been found to increase with decreasing radius. This variation of α tends to off-set the geometric effect of decreasing flow area with decreasing r which would otherwise tend to increase the radial air velocity as r decreases. Using the measured values of P, α, and $\dot{m}$ it is found that the du/dr term is indeed three to four orders of magnitude less than r(dP/dr). Then neglecting the du/dr term in Eq. (6.18), the tangential water velocity is

$$V = \left[\frac{1}{\rho_L(1-\alpha)}\left(r\frac{dP}{dr} - \frac{\alpha P}{RT}v^2\right)\right]^{\frac{1}{2}} \qquad (7.1)$$

Using this result to replace V in the tangential momentum equation (Eq. 6.14), an equation involving only v, r and measured parameters is obtained as

$$\frac{d}{dr}(rv) = -\frac{K}{\dot{m}}r^2 P^{0.532}(\alpha v)^{1.532}\left[\frac{(1-\alpha)}{\rho_L}\left(r\frac{dP}{dr} - \frac{\alpha P}{RT}v^2\right)\right]^{0.2585} \qquad (7.2)$$

Equation (7.2) can be evaluated, using the measured radial distributions of α and P, by the Runge-Kutta integration procedure when a suitable boundary value of $v = v_o$ at r_o is introduced. The initial value of the tangential air velocity to be used in Eq. (7.2) is $(v_n - \Delta v)$ where v_n is the nozzle exit air velocity and Δv is the decrease in the tangential air velocity incurred due to the drag on the outer cylindrical wall plus the drag of that annular flow element on the end plates. Equation (7.2) cannot account for the nozzle ring drag since it was formulated in terms of the momentum flux balance across annular elements which were assumed to experience a drag force due only to the end plates.

Taking an angular momentum flux balance across the peripheral annular element of thickness $r_o - (r_o - \Delta r)$,

$$-\dot{m}\,\Delta(rv) = \dot{m}[r_o v_n - (r_o - \Delta r)v_o] = F_{\phi_o} r_o \qquad (7.3)$$

The drag force F_{ϕ_o} is evaluated from Eq. (6.8) using the drag area

$$A_D = 2\pi r_o h + 4\pi\left[r_o^2 - (r_o - \Delta r)^2\right] \qquad (7.4)$$

which approaches the value of $2\pi r_o h$ as Δr becomes very small. Then the torque $F_{\phi_o} r_o$ due to the drag on the nozzle ring is obtained simply by evaluating Eq. (6.10) at $r = r_o$ and multiplying by the ratio of drag areas

$$\frac{2\pi r_o h}{4\pi r_o \, dr} = \frac{h}{2\,dr}$$

Then for Δr very small, Eq. (7.3) becomes

$$v_o - v_n = \left(\frac{-K\ h\ r_o}{2\dot{m}}\ P_o^{0.532}(\alpha_o v_o)^{1.532}\right) \left\{\frac{(1-\alpha_o)}{\rho_L}\left[r_o\left(\frac{dP}{dr}\right)_o - \frac{\alpha_o P_o}{RT}\ v_o^2\right]\right\}^{0.2585} \tag{7.5}$$

From this result an effective value of v_o can be obtained by successive approximations for each set of conditions. The v_o thus determined is then used as the initial value of v in the solutions of Eq. (7.2).

Since both P and dP/dr appear in the equations for v and V, it is convenient for computer programming to express P as an analytical function of the radius. Using the pressure difference ratio $(P - P_E)/(P_o - P_E)$, which was found to be a unique function of r as was shown in Fig. 5.12, it was found that the empirical relationship

$$\frac{P - P_E}{P_o - P_E} = 0.00345 \exp\left(5.76\ \frac{r}{r_o}\right) \tag{7.6}$$

provides a good correlation between P and r (Fig. 7.1).

The set of equations (6.18), (7.1), (7.2), (7.5) and (7.6) were programed on a digital computer and solutions obtained for u, v and V using the measured values of $\dot{m}$, v_n, P_o, P_E, α, T and a suitable value of K. The input

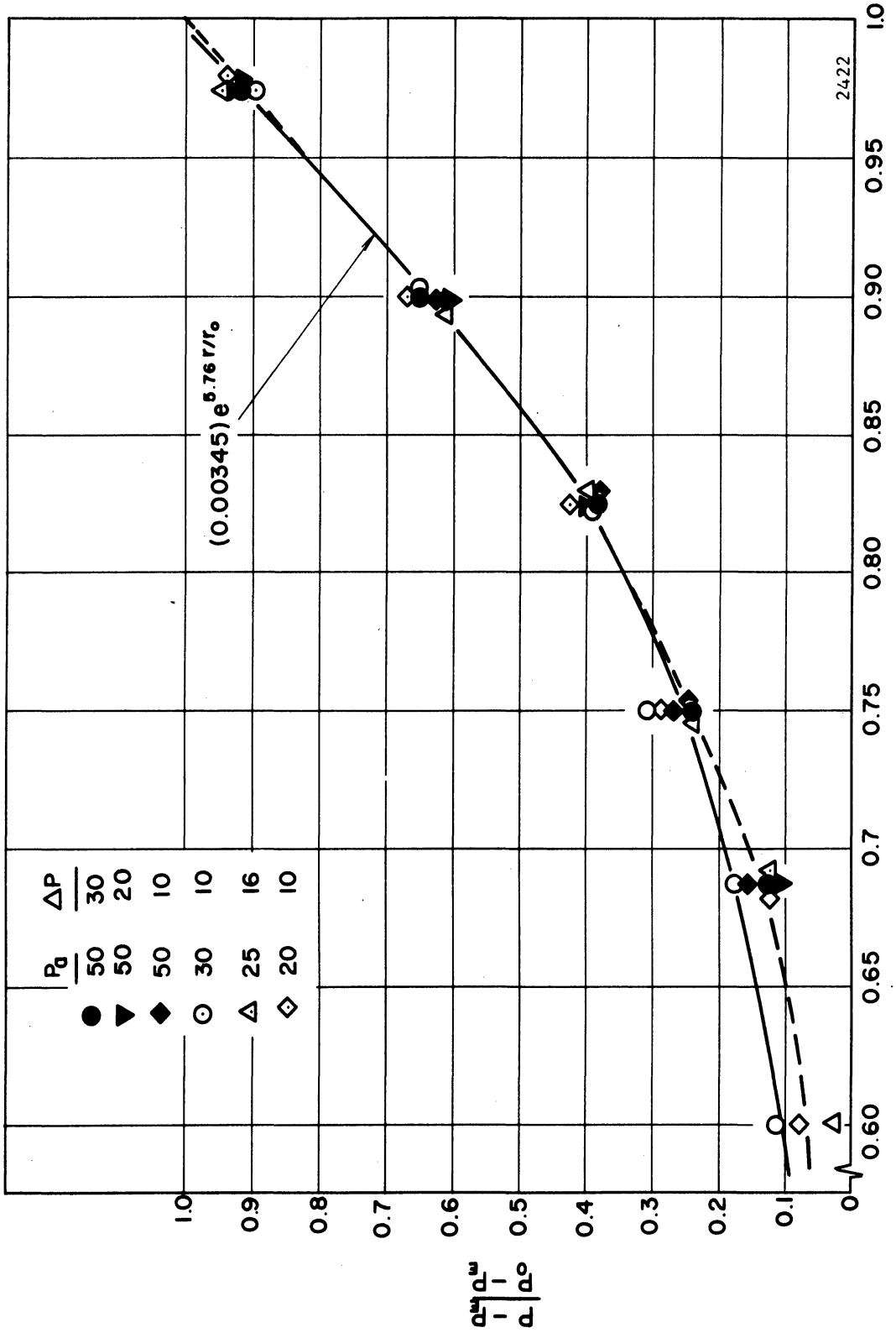

Fig. 7.1 - Comparison of the Measured Pressure Difference Ratio to the Empirical Approximation.

data used in the solutions of these equations are listed in the Appendix.

B. Radial Air Velocity

The radial air velocity is calculated by Eq. (6.18) and (7.6) in a straight-forward manner using the experimentally determined values of α and $\dot{m}$. The resulting distributions are presented in Fig. 7.2 for representative values of P_a and $\triangle P$. These radial distributions show very little variation with r as was predicted in the discussion of the magnitude of the du/dr term in the radial momentum equation.

C. Tangential Air Velocity

An initial estimate of the constant K for calculation of the tangential air velocities was obtained by evaluating Eq. (6.11) for air and water at room temperature, using $k = 0.272$ as found by Chien and Ibele[48] for two-phase pipe flow. These conditions give a value of K of approximately 10^{-4}. Starting with this value, the applicable value for the vortex flow equations was determined by varying K until the exit angle of the air leaving the two-phase region agreed with that observed, i.e., an angle of 20° to 24° with the tangent at $r/r_o = 0.55$ for $P_a = 50$ psig and $P = 16$ and 20 psi. The radial air velocity u (which is independent of K) was

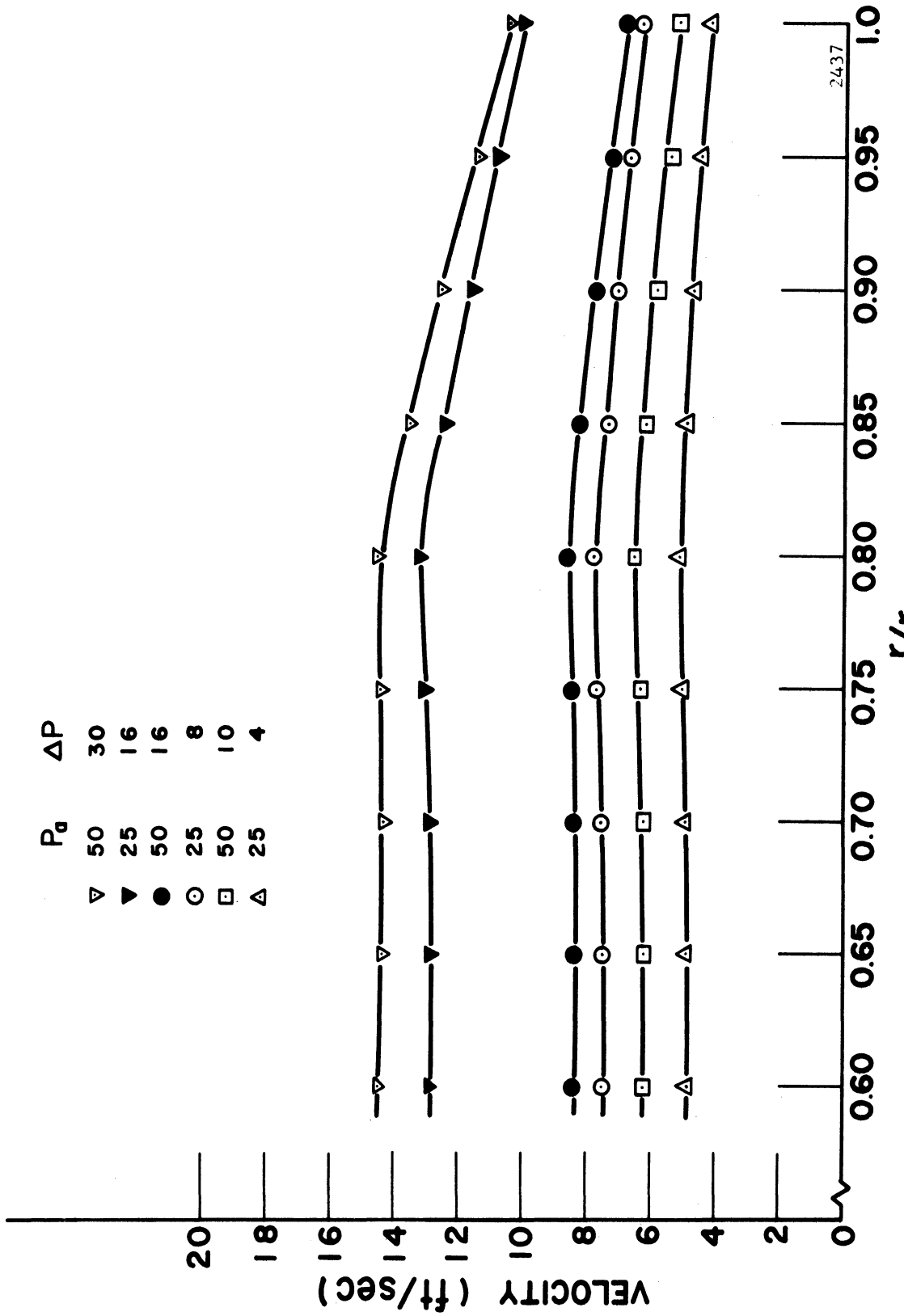

Fig. 7.2 - Radial Distribution of the Radial Air Velocity.

used to determine the value of v necessary at $r/r_o = 0.55$ to provide agreement with the observed exit angle. With u calculated to be from 8.2 to 9.5 ft/sec at these conditions, a tangential air velocity of about 20 ft/sec at the specified conditions is required.

Representative results of the solutions for v, as a function of K and r, obtained for $P_a = 50$ psig and $\Delta P = 16$ psi are shown in Fig. 7.3. Here it is seen that $K = 4 \times 10^{-4}$ gives the desired value of v of approximately 20 ft/sec at $r/r_o = 0.55$. The fact that this value of K differs from that estimated from the pipe flow correlations by only a factor of 4 is considered to be very good agreement since the flow geometry is radically different and the velocity values determined by these calculations result in superficial Reynolds numbers an order of magnitude higher than those for which Chien and Ibele made their pipe flow correlations. In obtaining solutions for the tangential air velocities, it was assumed that K remained constant over the range of air velocities investigated.

The radial variations of the tangential air velocity calculated using $K = 4 \times 10^{-4}$ are shown in Fig. 7.4, 7.5 and 7.6 for $P_a = 25$, 35 and 50 psig, respectively, for several values of ΔP. These results show that the air velocity decreases rapidly with decreasing r near the outer radius, and approaches a relatively constant value near the

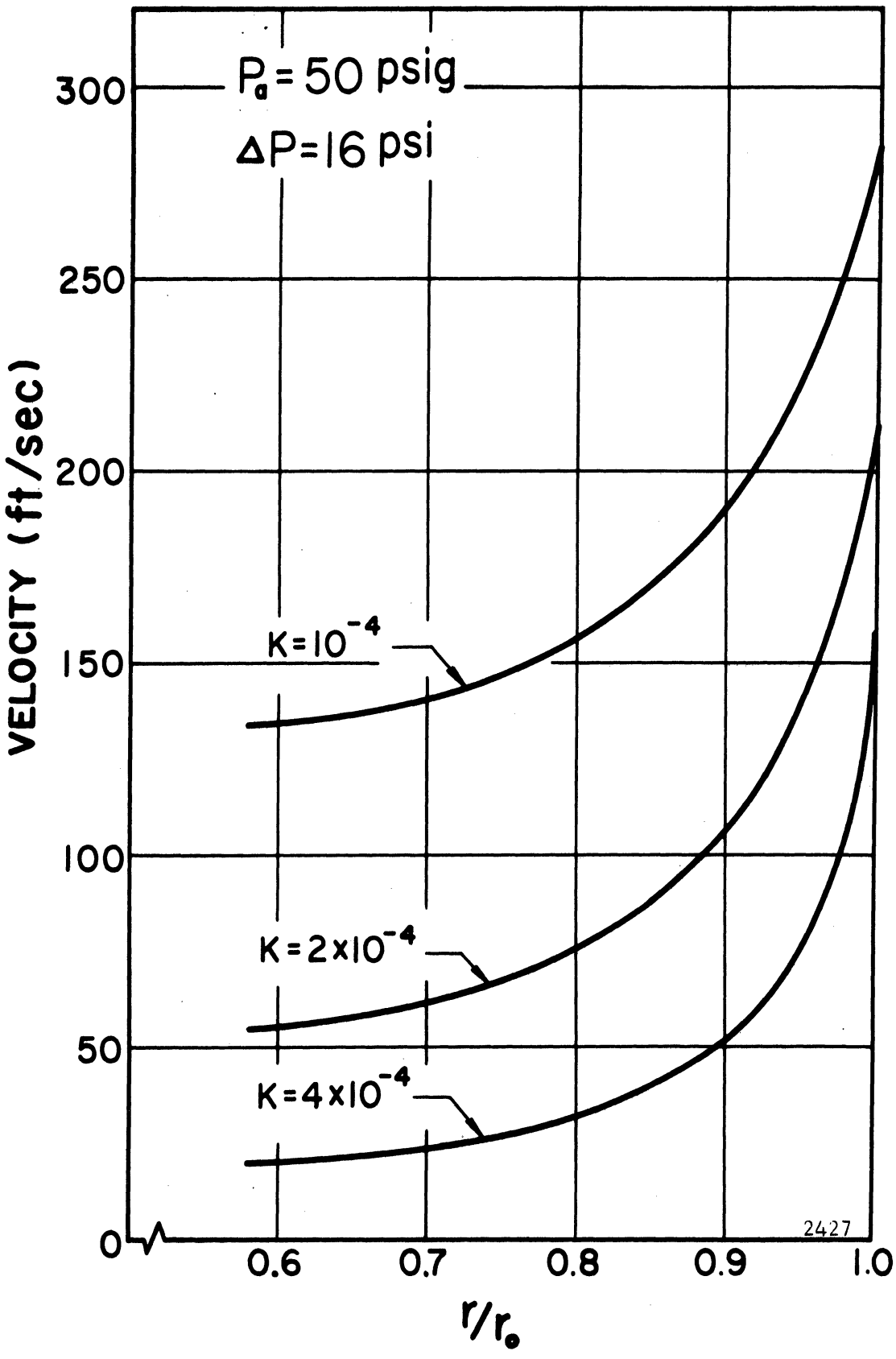

Fig. 7.3 - Radial Distribution of the Tangential Air Velocity as a Function of K.

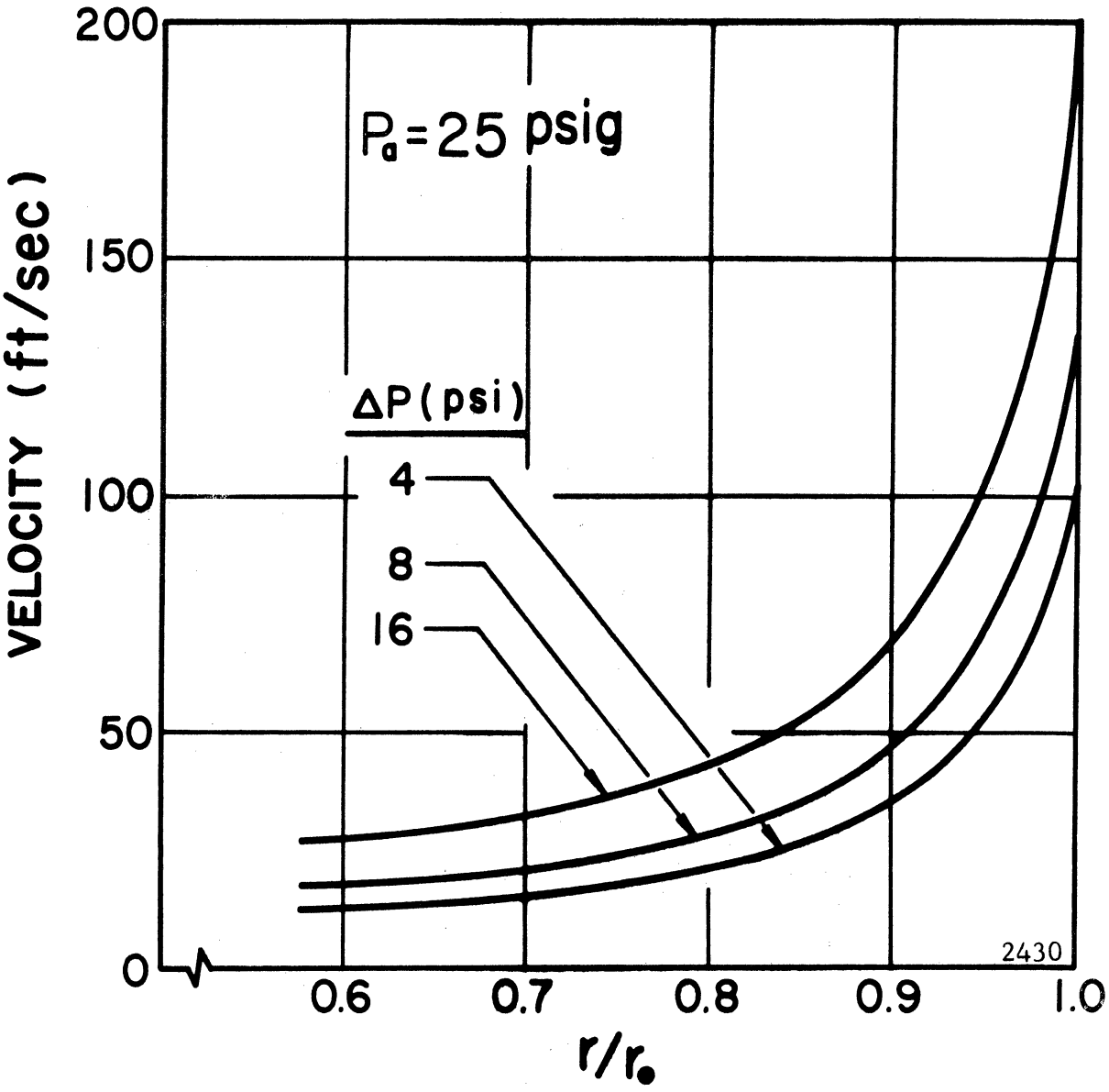

Fig. 7.4 - Radial Distribution of the Tangential Air Velocity as a Function of ΔP. P_a = 25 psig.

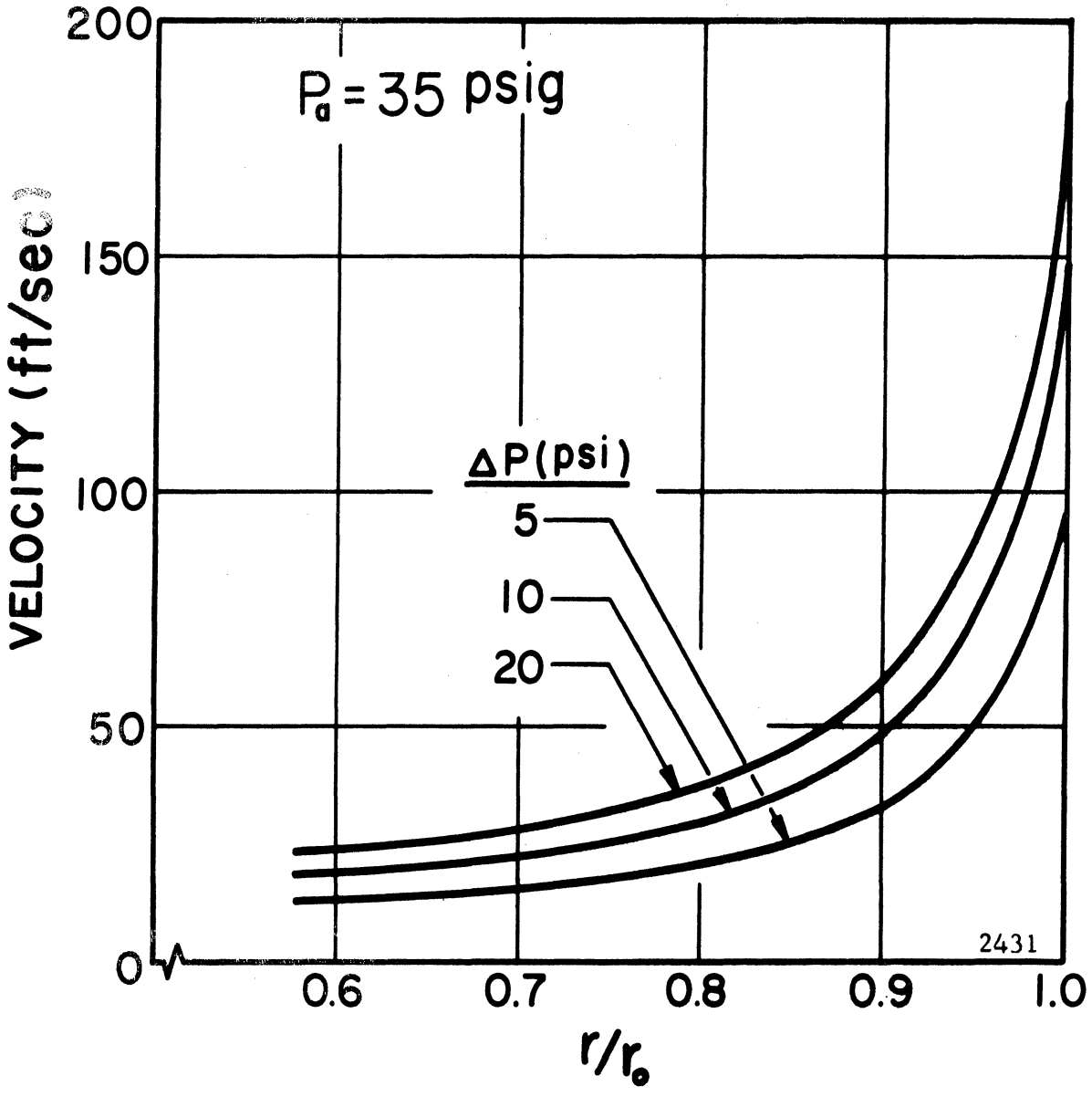

Fig. 7.5 - Radial Distribution of the Tangential Air Velocity as a Function of ΔP. P_a = 35 psig.

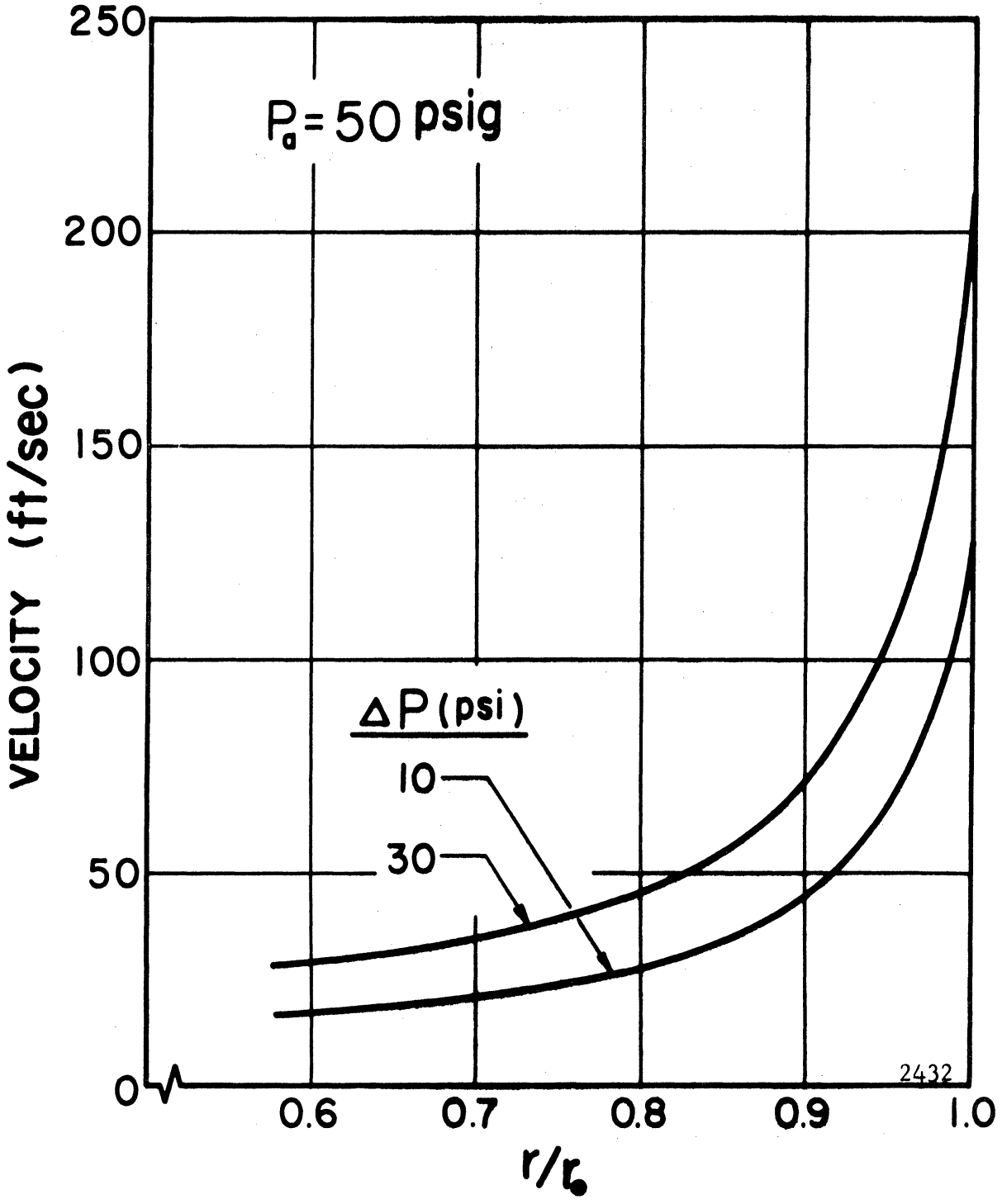

Fig. 7.6 - Radial Distribution of the Tangential Air Velocity as a Function of ΔP. P_a = 50 psig.

inner radius of the two-phase region. The radial average* of the tangential air velocity increases with ΔP for a given P_a but decreases with increasing P_a at constant ΔP due to the reduction in v_n as P_a/P_o decreases. This latter characteristic is illustrated in Fig. 7.7 where, for ΔP = 16 psi, v_n is seen to decrease with increasing P_a while the average water velocity,* shown by the broken curve, remains nearly constant. The tangential air velocity decreases by a factor of about 20 from the nozzle exits to the exit from the two-phase region. An out-standing characteristic demonstrated here is that most of this decrease, about 70% of $(v_n - v_E)$, occurs at the nozzle ring.

The variation of these quantities with P_a show that the greatest decrease in air velocity within the vortex occurs at the lower values of P_a; however, the decrease in angular momentum flux across the vortex is very nearly constant with P_a and ΔP at 10 lbm - ft^2/sec^2. Although v_n decreases with increasing P_a (at constant ΔP) by 30% from P_a = 20 to 50 psig, the air mass flow rate increases, due to increased density, by 50% (Fig. 7.8) resulting in a nearly constant momentum input at all P_a for a given ΔP. The slight rise in the mean water velocity at higher P_a indicates a more efficient momentum exchange at high P_a.

Considering the decrease in the tangential air velocity due to the drag on the nozzle ring, it was found that the

---

*Average velocity = $\int_{r_1}^{r_2} V(r)dr/(r_2 - r_1)$

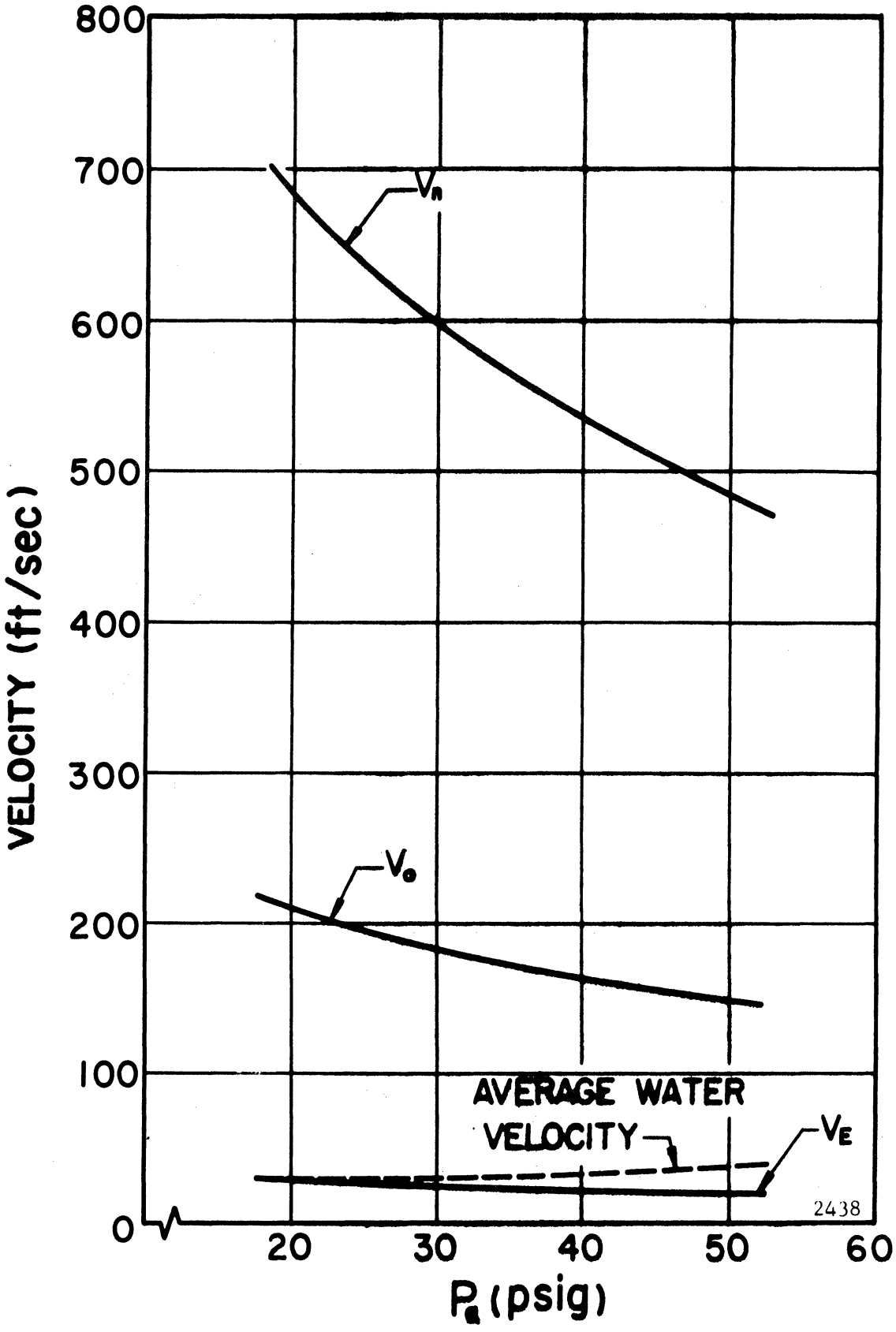

Fig. 7.7 - Variation of Air and Water Tangential Velocity with P_a at ΔP = 16 psi.

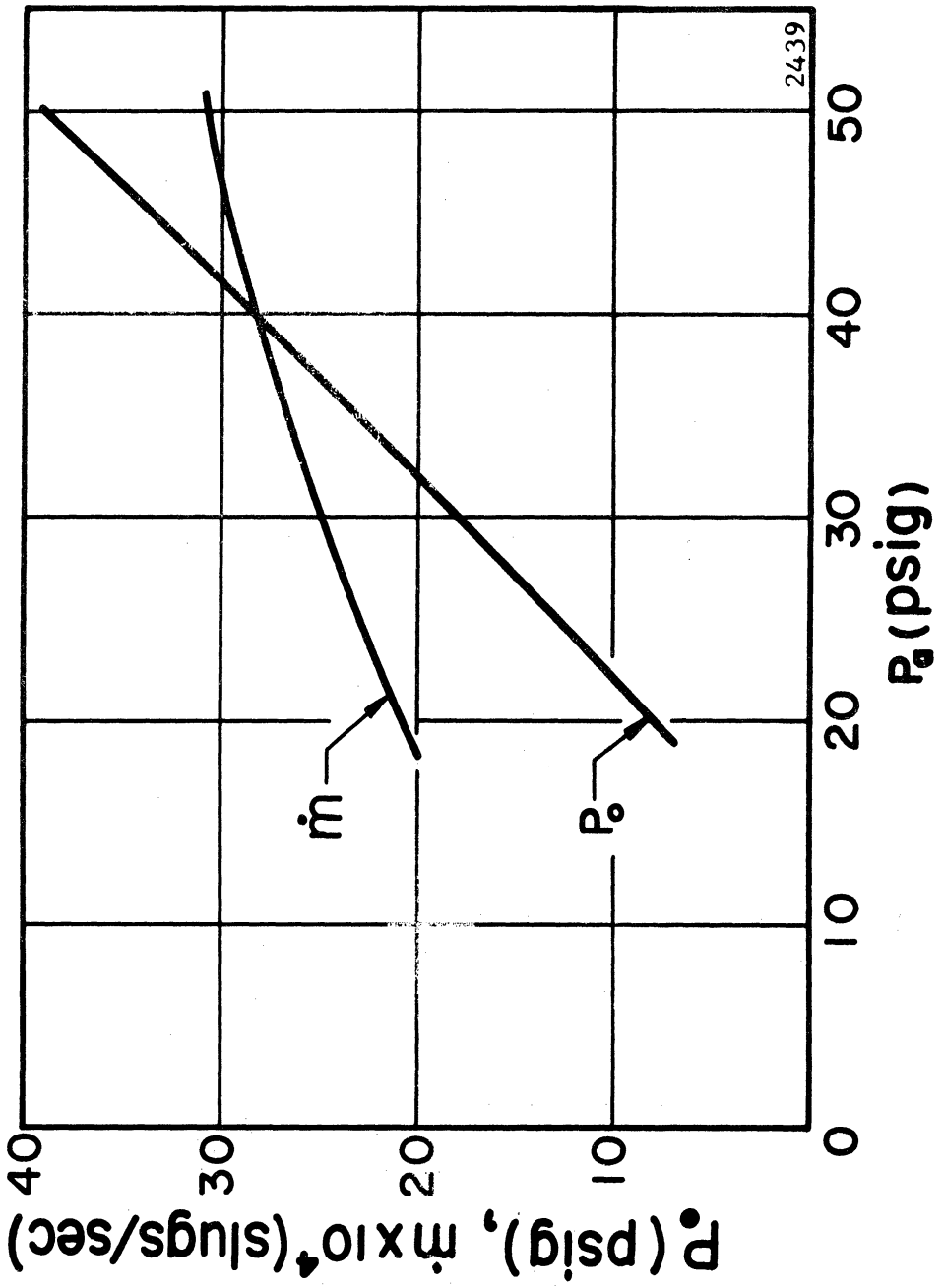

Fig. 7.8 - Air Mass Flow Rate and P_o as a Function of Pa.

jet recovery factor v_o/v_n in these calculations is about 0.31 for all cases, as compared to average values ranging from 0.4 to 0.7 reported for jet-driven single-phase vorticies.[28,31] Since the air velocities calculated from the analytical model are dependent on the value of K (which was determined by an estimate of the exit angle of the air from the two-phase region), the extent to which the calculated values of the jet recovery factor agree with the measurements from single-phase vortices provides some confidence as to the validity of the simple analytical model developed in this investigation. It should be emphasized that comparisons such as the one above are the only means available by which the validity of the calculated air velocities can be evaluated, since there is no feasible means by which the local air velocities can be measured. It was shown, for example, in Chapter VI, that in the equations relating phase velocities and impact pressures (Eq. 6.21 and 6.22), the air velocity term is negligible compared to the term involving the water velocity.

D. Tangential Water Velocity

With the values of v determined from Eq. (7.2), V was calculated from the radial momentum equation (Eq. 7.1). It was found that, due to the strong radial pressure gradient, V is very insensitive to v, e.g., for a given pressure gradient, a 100% increase in v corresponds to a

decrease in V of less than 3%. This implies that the normalized water velocity V/V_o is essentially a unique function of radius. The V_o used here is the effective value of the water velocity at $r = r_o$ obtained by extrapolating the radial distribution of V to the nozzle ring wall. If the term in v^2 is neglected in Eq. (7.1), it is seen that with the use of the pressure correlation (Eq. 7.6),

$$V/V_o = \left[0.00345 \frac{r}{r_o} \exp(5.76 \frac{r}{r_o})\right]^{\frac{1}{2}} \qquad (7.7)$$

which expresses the velocity ratio as a function of r only, as it should.

The distribution of V/V_o is shown in Fig. 7.9 where it is compared to the normalized water velocities obtained from the impact pressure measurements and Eq. (6.22). The velocity distributions obtained by the measured impact pressures $(P_t - P)$ are flatter than those calculated from the pressure gradient using Equation (7.1) or (7.7). This result is reasonable in view of the probe effects on the static pressure, i.e., according to Roschke[31] and Pivirotto,[33] the presence of the probe increases the static pressure near the center and decreases P near the periphery. Hence, since the static pressures were measured without the probe inserted into the vortex, the measured impact pressures are too high at the smaller values of r and too low near the periphery, resulting in the deviations apparent

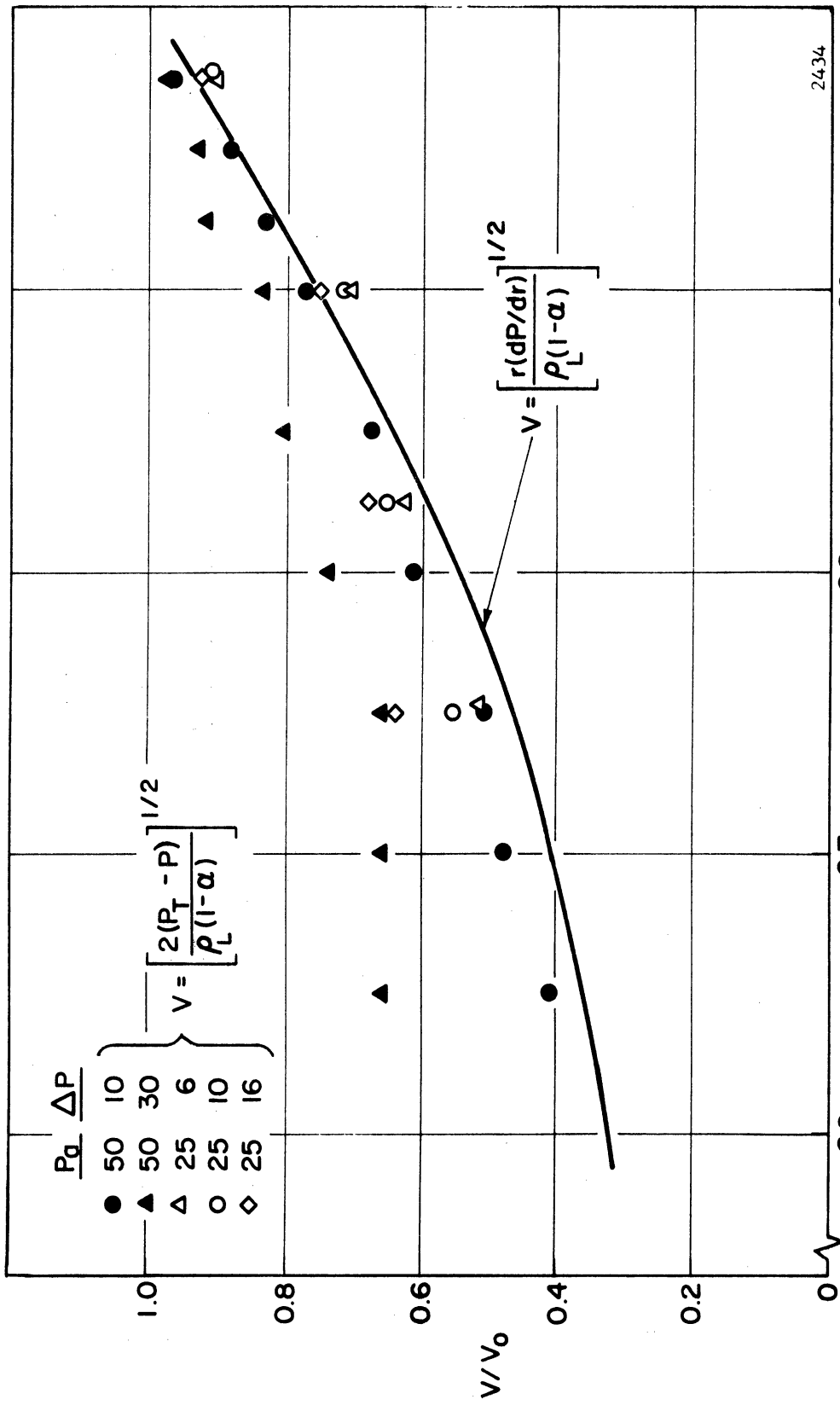

Fig. 7.9 - Radial Distribution of Tangential Water Velocity.

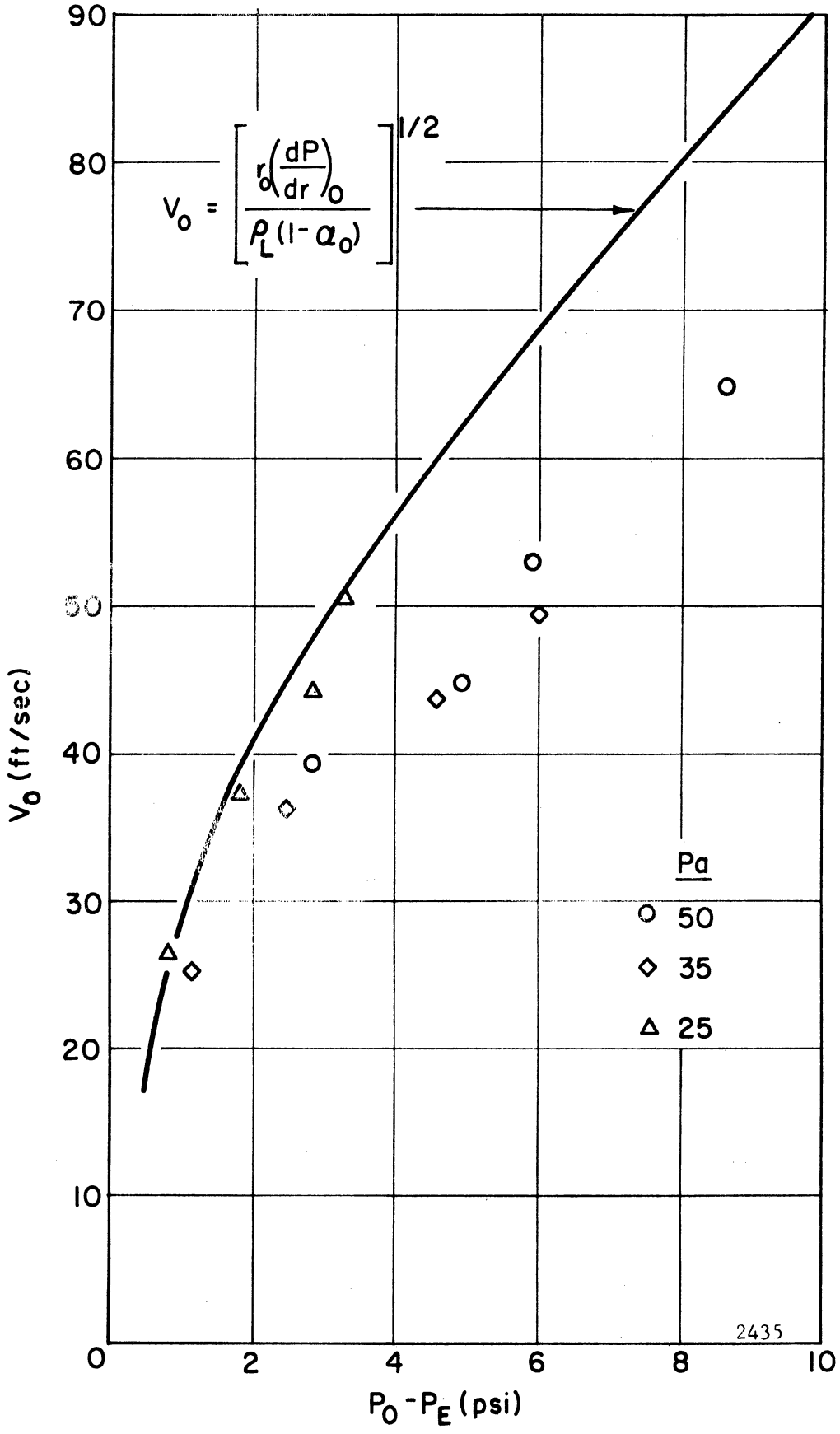

Fig. 7.10 - Variation of V_o with Pressure Drop Across the Vortex.

in Fig. 7.9. The lower values of the effective wall velocity V_o obtained from the impact pressure measurements are shown in Fig. 7.10 where they are compared to those obtained from Eq. (7.1).

Although close agreement between the two calculations of the water velocity is not expected due to the above considerations as well as the inaccuracy of pitot tube measurements in two-phase flow,[36] the general agreement in magnitude and radial distribution of V exhibited between the two sets of calculations is encouraging insofar as the applicability of the analytical model is concerned.

E. Open Circuit Voltage from Electromagnetic Effects

With the radial distributions of the water velocity obtained from the pressure gradient and void fraction measurements, the integrals in the equation relating the open circuit voltage E_o to the water velocity (Eq. 6.30) can be evaluated numerically. The expression thus obtained for E_o is

$$E_o = 0.635\ B\ h\ V_o = 1.084\ BhV_{av} \tag{7.8}$$

This result is compared to the measured values of E_o in Fig. 7.11 where E_o/V_o is plotted against B. The relationship

$$E_o = BhV_{av} \tag{7.9}$$

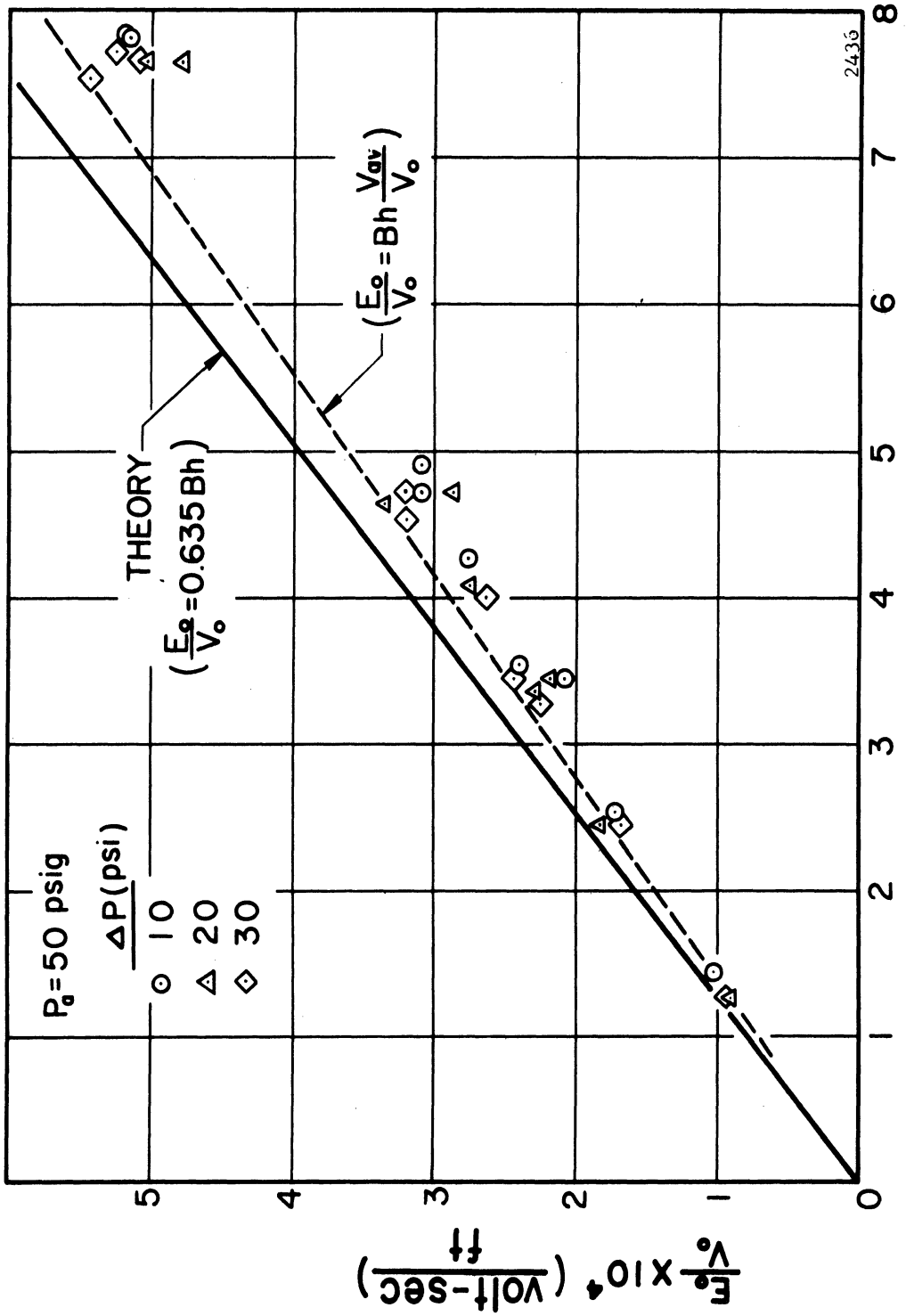

Fig. 7.11 - Comparison of Open Circuit Voltage Measurements.

is also presented for comparison. The measured values of E_o fall slightly below those obtained from both Eq. (7.8) and (7.9), probably because of the electrical losses within the vortex. It must also be considered that the velocity distribution used, as well as the void fractions, are based on average values. In the actual vortex investigated there are extreme variation in α and P which are not considered in the simple analytical model from which V was obtained. Under these considerations, the extent of the agreement between the predicted and measured values of E_o gives strong evidence of the validity of the analytical model for the vortex used in this investigation.

CHAPTER VIII

SUMMARY AND CONCLUSIONS

A. Analytical Model

An analytical model has been developed to describe the jet-driven two-phase vortex and to aid in the understanding of such flows. Utilizing experimental data and adapting a two-phase friction factor obtained from correlations for pipe flow, this model is used to calculate the velocity distributions of the two phases within the air-water vortex. These calculations utilized the measured values of driving-jet velocity, mass flow rate, void fraction and static pressure.

The computed velocities are in very good agreement with independent measurements and with trends predicted from other investigations of single-phase vortex flow.

B. Pressure Measurements

The air-balance system developed to measure the pressures in the two-phase flow was found to give consistent and repeatable results. From the static pressure measurements, it was found that the ratio $(P - P_E)/(P_o - P_E)$ provided a correlation of P as a unique function of radius. The radial dependence of the pressure difference ratio was approximated quite well by the empirical relationship

$$\frac{P - P_E}{P_o - P_E} = (0.00345)\ \exp\left(5.76\ \frac{r}{r_o}\right) .$$

The variations in total pressure measured within the vortex showed trends which were consistent with the local perturbations of the flow caused by the nozzles and with the magnitude of the pressure drop across the vortex. However, due to the disturbance of the flow by the pressure probe and the inherent inaccuracies associated with pitot tube measurements in two-phase flow, the exact degree to which the measured total pressures represent the free stream conditions is not known.

C. Void Fraction Measurements

The void fraction probe (conductivity probe) developed in this investigation provided a simple and reliable means for measuring local void fractions in two-phase flow. A complete theoretical analysis to explain the response of the probe, as a function of both velocity and void fraction, over the entire range of void fraction is not yet available.

Over the range of pressures investigated, the void fraction distribution within the two-phase vortex was found to be relatively insensitive to pressure level and pressure drop across the vortex. The average void fraction (average of axial and azimuthal variations) was found to be essentially constant at about 0.5 for $0.825 < r/r_o < 1.0$, and increased with decreasing radius to a value of approximately 0.725 at $r/r_o = 0.60$.

D. Radial Air Velocities

The radial component of the air velocity (calculated from the conservation of mass relationship) showed very little variation with radius. This result was expected since it is typical of jet-driven vortices with high ratios of tangential jet-velocities to radial jet-velocities and since the nature of the variation of void fraction in this case very nearly cancelled the geometric effect of decreasing radial flow area with decreasing radius.

E. Tangential Air Velocity

By establishing a boundary condition at the inner radius of the two-phase region, i.e., the exit angle of the air from the two-phase region, the radial distribution of the tangential air velocity was calculated from the analytical model. These calculations were based on measured values of pressure, void fraction, mass flow rate and air-jet velocity. The detailed agreement between these results and the actual air velocities could not be assessed due to the lack of a method for measuring the local air velocity in two-phase flow. An indication of the validity of the calculated air velocities was obtained by computing the jet-recovery factor v_o/v_n. This parameter was found to be about 0.31 for all cases as compared to average values ranging from 0.4 to 0.7 reported for jet-driven single-phase vortices.[38,31] Since the ratio of the jet air density to the

vortex density is very large for a two-phase vortex as compared to the single phase case, a relatively low jet-recovery factor would be expected.

A further indication of the validity of the calculated air velocities was the value of the constant K, associated with the two-phase drag force, which was necessary to satisfy the boundary condition at the inner radius of the two-phase annulus. This value of K was found to be within a factor of four of the value determined from the empirical correlations for two-phase pipe flow.[48] Considering the difference in the flow geometry between pipe flow and confined vortex flow, this degree of agreement in the value of K is encouraging.

For a constant pressure drop across the vortex, it was found that the angular momentum input of the air and the loss of angular momentum across the two-phase region were essentially constant for all plenum pressures. Since the average water velocity increased slightly at the higher values of plenum pressure at constant momentum input, it is concluded that the effective momentum exchange between the air and water is greater at the higher pressures. This might be expected since the density ratio of driving to driven fluid increases somewhat and the air velocity decreases.

F. Tangential Water Velocity

For corresponding values of void fraction and radial pressure gradient, the tangential water velocity was found to be quite insensitive to the magnitude and variations of the air velocity. Thus, as predicted by the analytical model, the water velocity was, as a very good approximation, expressed as

$$V = \left[\frac{r}{\rho_L (1 - \alpha)} \frac{dP}{dr} \right]^{\frac{1}{2}}$$

The magnitude of the water velocities calculated from this relationship agreed well with estimates obtained from the open circuit voltages produced when the vortex operated in the presence of a magnetic field. The radial variation of V obtained from the analytical model deviated from that estimated from the pitot tube (impact pressure) measurements in a predictable manner. The pitot tube estimates were low near r_o and high at small r/r_o compared to those calculated from the analytical model, as expected, since probe disturbance in vortex flow has been found to decrease the static pressure near the periphery and increase P at the inner radii relative to free stream conditions.[31,33]

G. Applications

1. Vortex MHD Power Generator: The results of this investigation show that a vortex MHD generator is a feasible

concept. It has been demonstrated that a stable two-phase flow of annular configuration can be maintained with a void fraction which results in a reasonable electrical conductivity. Because of the low conductivity of water, only open-circuit tests were meaningful in the present work with an air-water vortex. Hence, the MHD aspects of the unit could not be evaluated. The practicality of the MHD application depends upon the characteristics of a jet-driven vortex utilizing a liquid with a much higher conductivity, such as a liquid metal. The velocities required to maintain an annulus of fluid in the vortex in the presence of gravity forces are independent of density, i.e., it is only necessary that $(V^2/r)/g >> 1.0$. Hence, the difference in flow characteristics between a vortex using water and one using liquid metal (without MHD effects) will result from differences in viscosity and perhaps a different void fraction distribution resulting from the difference in the centrifugal force term ($\rho V^2/r$).

The operation of the vortex as a MHD power generator would be enhanced by an increased momentum transfer per unit volume of liquid. This could be accomplished by increased momentum input by the gas jets (by increased gas velocity and/or mass), reduction in the liquid mass within the vortex, and an increase in the jet-recovery factor which might conceivable be accomplished by suitable changes in flow geometry.

Research on these aspects, in addition to investigation of the MHD characteristics of the flow, would be an obvious and important extension of this investigation.

2. Liquid Core Nuclear Rocket: In the application of the two-phase vortex to the liquid core nuclear rocket concept, two major problems are a) the carry-over of the fuel into the rocket exhaust and b) the necessity to isolate the liquid mass from the walls of the containment vessel in order to permit maximum temperature operation.

Although the volume rate of carry-over of liquid in the exhaust of the air-water vortex was small, the mass of liquid lost per minute was of the order of the total liquid mass in the vortex. However, the retention time of the liquid ($m_L/\dot{m}_L$) varied between 0.5 and 2.0 minutes as compared to 1 to 4 seconds retention time for a heavy gas (freon or argon) in a mixture with a lighter gas (hydrogen or nitrogen) in a jet-driven gaseous vortex.[34]

Isolation of the liquid from the container walls, as well as an increase in the jet-recovery factor, might be accomplished by providing a boundary layer of gas at the walls by the use of porous material for the containment vessel. The effect of this modification on liquid carry-over would also have to be considered. The increased total mass flow of gas, if unaccompanied by an increase in its driving angular momentum input, might result in increased carry-over, while a reduction in liquid carry-over would be expected to result from a substantial gain in the jet-recovery factor.

It will be necessary to examine these problems and the possible solutions in detail before the practicality of the liquid core nuclear rocket (utilizing jet-driven vortex flow) can be established.

APPENDIX

OPERATING CONDITIONS AND CORRESPONDING EXPERIMENTAL DATA SELECTED FOR CALCULATION OF THE VELOCITY DISTRIBUTIONS FROM THE ANALYTICAL MODEL

P_a (psig)	ΔP (psi)	$\dot{m}$ (slug/sec)	$P_o - P_E$ (lb/ft^2)	P_E (lb/ft^2)	v_n (ft/sec)
20	16	-0.00208	469.4	2664	682
25	4	-0.00129	115.2	5112	320
25	8	-0.00177	273.6	4536	456
25	12	-0.00208	417.6	3960	565
25	16	-0.00230	504.0	3384	652
30	16	-0.00249	535.7	4104	595
35	5	-0.00158	168.5	6408	310
35	10	-0.00222	354.0	5688	455
35	16	-0.00265	569.0	4824	557
35	20	-0.00283	858.0	4248	613
40	16	-0.00282	602.0	5544	537
45	16	-0.00296	633.6	6264	510
50	10	-0.00256	374.4	7848	389
50	16	-0.00306	668.0	6984	483
50	20	-0.00336	835.2	6408	543
50	30	-0.00382	1238.4	4968	660

REFERENCES

1. Eskinazi, S., Principles of Fluid Mechanics, Allyn and Bacon, Inc., Boston, 1962, p. 414.

2. Kelsall, D. F., "Study of Motion of Solid State Particles in a Hydraulic Cyclone," Transactions of the Institute of Chemical Engineers, Vol. 30, No. 3, 1952, pp. 87-104.

3. Lawler, M. T. and Ostrach, S., "A Study of Cyclonic Two-Fluid Separation," Report No. AFOSR 65-1523, Engineering Division, Case Institute of Technology, Cleveland, Ohio, 1965.

4. Kerrebrock, J. L. and Meghreblian, R. V., "An Analysis of Vortex Tubes for Combined Gas-Phase Fission Heating and Separation of the Fissionable Material," ORNL-CF-47-11-3, 1957.

5. Kerrebrock, J. L., and Meghreblian, R. V., "Vortex Containment for the Gaseous-Fission Rocket," Journal of Aerospace Science, Vol. 28, No. 9, September 1961, pp. 710-724.

6. Donaldson, C. duP., Hamel, B. B., McCune, J. E., and Snedeker, R. S., "Theory of the Magnetohydrodynamic Homopolar Generator, Part I: Liquid Mediums," Aeronautical Research Associates of Princiton, Rept. No. 20, September, 1959.

7. McCune, J. E., "Theory of the Magnetohydrodynamic Homopolar Generator, Part II: Gaseous Mediums," Aeronautical Research Associates of Princeton, Rept. No. 25, June, 1960.

8. Donaldson, C. duP., "The Magnetohydrodynamic Vortex Power Generator: Basic Principles and Practical Problems," Engineering Aspects of Magnetohydrodynamics, Edited by C. Mannal and N. W. Mather, Columbia University Press, New York, 1962, pp. 228-254.

9. Holt, W. D. and Rivard, J. G. "Research Study of the Vortex Valve for Medium-Temperature Solid Propellants," NASA CR-424, The Bendix Corp., Southfield, Michigan, April, 1966.

10. Tempelmeyer, K. E. and Rittenhouse, L. E., "Vortex Flow in Arc Heaters," AIAA Journal, Vol. 2, No. 4, April 1964, pp. 766, 767.

11. Palanek, E. J., "Experimental Study of Vortex Flow in a Cylinder," M.S. Thesis, School of Engineering, Air Force Institute of Technology, Wright-Patterson Air Force Base, Ohio, March, 1966.

12. Sellers, A. J., et. al, "Recent Developments in Heat Transfer and Development of the Mercury Boiler for the SNAP-8 System," Proceedings of the Conference on Application of High Temperature Instrumentation to Liquid-Metal Experiments (ANL-7100), 1965, pp. 573-632.

13. Turner, J. S. and Lilly, D. K., "The Carbonated-Water Tornado Vortex," Journal of Atmospheric Sciences, Vol. 20, No. 5, 1963, pp. 468-471.

14. Lanzo, C., Personal Cummunication, May, 1966.

15. McLafferty, G. H., Personal Communication, May, 1966.

16. Bussard, R. W. and DeLauer, R. D., Fundamentals of Nuclear Flight, McGraw-Hill Book Co., New York, 1965, p. 12.

17. Weber, N. E. and Marston, C. H., "Liquid Metal Vortex Generator," ASME Paper No.63-WA-209.

18. Weber, H. E., and Marston, D. H., "MHD With Liquid Metal," Mech. Eng., Vol. 86, No. 8, 1964, p. 34.

19. Nelson, S. T., "Conceptual Design Study of a Liquid-Core Nuclear Rocket," Report No. 665, Guggenheim Laboratories for the Aerospace Propulsion Sciences, Princeton University, September 1963.

20. Pedersen, E. S., Nuclear Energy in Space, Prentice-Hall, Inc., Englewood Cliffs, N. J., 1964, pp. 257-265.

21. Anderson, O. L., "Theoretical Solutions for the Secondary Flow on the End Wall of a Vortex Tube," Report R-2494-1, United Aircraft Corporation Research Laboratories, East Hartford, Conn., Nov. 1961.

22. Anderson, O. L., "Theoretical Effect of Mach Number and Temperature Gradient on Primary and Secondary Flows in a Jet-Driven Vortex," Report RTD-TDR-63-1098, United Aircraft Corporation Research Laboratories, East Hartford, Conn., November 1963.

23. Savino, J. M. and Keshock, E. G., "Experimental Profiles of Velocity Components and Radial Pressure Distributions in a Vortex Contained in a Short Cylindrical Chamber," NASA TN D-3072, NASA Lewis Research Center, Cleveland, Ohio, October 1965.

24. Loper, D. E., "An Analysis of Confined Vortex Flows," Report No. A-31, Plasama Research, Case Institute of Technology, Cleveland, Ohio, June 1964.

25. Ginsberg, T., "Flow Distributions in a Confined Viscous Vortex," Technical Memorandum TM 605.2621-04, Ordnance Research Laboratory, Pennsylvania State University, April 1966.

26. Roschke, E. J., "Flow Visualization Studies of a Confined, Jet-Driven Water Vortex," Technical Report 32-1004, Jet Propulsion Laboratory, Pasadena, Calif., Sept. 1966.

27. Travers, A., "Experimental Investigation of Peripheral-Wall Injection Techniques in a Water Vortex Tube," Report D-910091-7, United Aircraft Corporation Research Laboratories, East Hartford, Connecticut, Sept. 1965.

28. McFarlin, D. J., "Experimental Investigation of the Effect of Peripheral-Wall Injection Techniques on Turbulence in an Air Vortex Tube," Report D-910091-5, United Aircraft Corporation Research Laboratories, East Hartford, Connecticut, Sept. 1965.

29. Ragsdale, R. G., "A Mixing Length Correlation of Turbulent Vortex Data," ASME Papaer No. 61-WA-244, Dec. 1961.

30. Keys, J. J., Jr., "An Experimental Study of Flow and Separation in Vortex Tubes with Application to Gaseous Fission Heating," ARS Journal, Vol. 31, Sept. 1961, pp. 1240-1210.

31. Roschke, E. J., "Experimental Investigation of a Confined, Jet-Driven Water Vortex," Technical Report No. 32-982, Jet Propulsion Laboratory, Pasadena, Calif., Oct. 1966.

32. Reshotko, E. and Monnin, C. F., "Stability of Two-Fluid Wheel Flows," NASA TN D-2696, NASA Lewis Research Center, Cleveland, Ohio, August 1965.

33. Pivirotto, T. J., "An Experimental and Analytical Investigation of Concentration Ratio Distributions in a Binary Compressible Vortex Flow," Technical Report No. 32-808, Jet Propulsion Laboratory, Pasadena, Calif., March 1966.

34. Pivirotto, T. J., "Mass-Retention Measurements in a Binary Compressible Vortex Flow," Technical Report No. 32-864, Jet Propulsion Laboratory, Pasadena, Calif. June 1966.

35. Lockhard, R. W. and Martinelli, R. C., "Proposed Correlation of Data for Isothermal Two-Phase, Two-Component Flow in Pipes", Chem. Eng. Prog., 45, 39-48, (1949).

36. Shires, G. L. and Riley, P. J., "The Measurement of Radial Vodiage Distribution in Two-Phase Flow by Isokinetic Sampling," Report AEEW-M650, Reactor Development Division, Atomic Energy Establishment, Winfrith, Dorset, England, 1966.

37. Petrick, M. P., "Two Phase Air-Water Flow Phenomena", ANL-5758, Argonne National Laboratory, (1958).

38. Smith, W., Atkinson, G. L., and Hammitt, F. G., "Void Fraction Measurements in a Cavitating Venturi", Trans. ASME, J. of Basic Eng., June 1964.

39. Petrick, M. P. and Lee, K., "Liquid MHD Power Cycle Studies", ANL-6954, Argonne National Laboratory, (1965).

40. Maxwell, J. C., A Treatise on Electricity and Magnetism, Oxford University Press, Vol. 1, p. 365, (1873).

41. Nassos, G. P., "Development of an Electrical Resistivity Probe for Void Fraction Measurements in Air-Water Flow", ANL-6738, Argonne National Laboratory, (1963).

42. Bencze, I., and Ørbeck, I., "Development of an Instrument for Digital Measurement and Analysis of Voids Using an A. C. Impedance Probe", KR-73, Institutt for Atomenergi, Kjeller Research Establishment (1964).

43. Richardson, B. L., "Some Problems in Horizontal Two-Phase Two-Component Flow", ANL-5949, Argonne National Laboratory (1958).

44. Fohrman, M. J., "The Effect of the Liquid Viscosity in Two-Phase Two-Component Flow", ANL-6256, Argonne National Laboratory (1960).

45. Vogrin, J. A., Jr., "An Experimental Investigation of Two-Phase Two-Component Flow in a Horizontal Converging-Diverging Nozzle," ANL-6755, Argonne National Laboratory, July 1963.

46. Smissaert, G. E., "Two-Component Two-Phase Flow Parameters for Low Circulation Rates," ANL-6755, Argonne National Laboratory, July 1963.

47. Baker, J. L. L., "Flow-Regime Transitions at Elevated Pressures in Vertical Two-Phase Flow," ANL-7093, Argonne National Laboratory, Sept. 1965.

48. Chien, Sze-Foo, and Ibele, W., "Pressure Drop and Liquid film thickness of Two-Phase Annular and Annular-Mist Flows," J. Heat Transfer, Trans. ASME, Vol. 86, 1964, pp. 89-96.

49. Shapiro, A. H., The Dynamics and Thermodynamics of Compressible Fluid Flow, Vol. 1, The Ronald Press Company, New York, 1953, p. 94.

50. Hammitt, F. G., Robinson, M. J. and Lafferty, J. F., "Choked Flow Analogy for Very Low Quality Two-Phase Flow," Nucl. Sci. Eng., To be published.

51. Hammitt F. G., et. al, "Fluid-Dynamic Performance of a Cavitating Venturi--Part I," Report 03424-2-T, Dept. of Nuclear Engineering, The University of Michigan, October, 1960.

52. Kolin, A., "Improved Apparatus and Technique for Electromagnetic Determination of Blood Flow," Rev. Sci. Instr., Vol. 23, 1952, p. 235.

53. Arnold, J. S., "An Electromagnetic Flowmeter for Transient Flow Studies," Rev. Sci. Instr., Vol. 22, 1951, p. 43.

54. Roschke, E. J. and Pivirotto, T. J., "Similarity in Confined Vortex Flows," Technical Report No. 32-789, Jet Propulsion Laboratory, Pasadena, Calif., Aug. 1965.